

PE&RS

December 2021

Volume 87, Number 12

PHOTOGRAMMETRIC ENGINEERING & REMOTE SENSING · The official journal for imaging and geospatial information science and technology





ASPRS 2022 Annual Conference

At Geo Week
February 6-8, 2022
Denver, CO, USA

Virtual
March 21-25, 2022

ASPRS 2022 Annual Conference at Geo Week in Denver, CO, February 6 - 8, 2022

In 2022, ASPRS will transition back to a traditional face-to-face conference format as part of Geo Week 2022. However, we realized that our virtual ASPRS conference in 2021 reached many attendees and presenters who, regardless of COVID, would not be able to take part in Geo Week due to travel or cost constraints. Therefore, we are holding our 2022 ASPRS Annual Conference in two parts.

The February 6-8, 2022, conference in Denver, Colorado will be a live, in-person event. It will not be broadcast or recorded. Attendees can participate in:

- ASPRS technical sessions consisting of individual presentations, panel discussions, and a poster gallery
- ASPRS 2-hour and 4-hour workshops
- Shared Geo Week exhibit hall and social networking functions
- ASPRS Board of Directors, Council, Division, and Committee meetings
- ASPRS Annual Business Meeting, including
 - o Presentation of ASPRS Awards and Scholarships
 - o Installation of Officers
- Past Presidents and ASPRS Foundation Board of Trustees meetings (by invitation)
- Student and Early Career Professional Mentoring and Networking

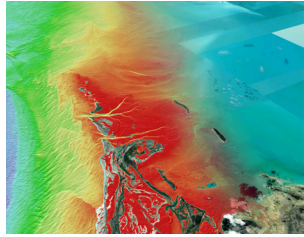
ASPRS 2022 Virtual Technical Program online, March 21 - 25, 2022

A live webinar event consisting of oral presentations, panel discussions, and an online poster gallery. This event will be recorded and made available on-demand.

For information on registering and presenting visit <https://my.asprs.org/2022conference>

For additional information or questions, contact programs@asprs.org.

ANNOUNCEMENT



As the effort in pursuit of the complete map of the ocean floor accelerates, The Nippon Foundation-GEBCO Seabed 2030 Project signs a new Memorandum of Understanding (MOU) with TCarta Marine, LLC (TCarta) – a US-based company dedicated

to marine remote sensing and hydrospatial data services.

Seabed 2030 is a collaborative project between The Nippon Foundation and GEBCO to inspire the complete mapping of the world's ocean by 2030, and to compile all bathymetric data into the freely available GEBCO Ocean Map. GEBCO is a joint project of the International Hydrographic Organization (IHO) and the Intergovernmental Oceanographic Commission (IOC) and is the only organisation with a mandate to map the entire ocean floor. Seabed 2030 is formally endorsed as a Decade Action of the UN Decade of Ocean Science for Sustainable Development.

TCarta has been a global innovator in Satellite Derived Bathymetry (SDB), marine remote sensing and space-based hydrospatial technologies since its founding in 2014. The company has extensive experience producing custom, project-specific SDB, as well as en masse through automation and cloud computation.

TCarta is currently underway in grant research, funded by the National Oceanic and Atmospheric Administration (NOAA) to pursue advancements in on-platform parameterization of satellite imagery collection for improved SDB data, as well as to develop standards of SDB, next-generation assessments of data accuracy, and definitions of zones of confidence.

“With just over 20 per cent of the seafloor mapped, we are aware of the significant task ahead of us – mapping the remaining 80 percent of the seafloor in under ten years,” commented Jamie McMichael-Phillips, Project Director of Seabed 2030. “However, at Seabed 2030 we subscribe to the view that with global cooperation, producing a complete map of the entire seafloor within our timeframe is achievable. We are therefore delighted to welcome the support of TCarta in helping us realise our goal.”

Commenting on the partnership, President of TCarta Kyle Goodrich said, “At TCarta, we recognize the need for a complete map of the seafloor and especially in vulnerable and dynamic coastal areas.

“We are very excited to bring TCarta’s vision for scalable, global satellite-based surveying technology, developed under our National Science Foundation Small Business Innovation Research grant, to participate in this important global initiative.

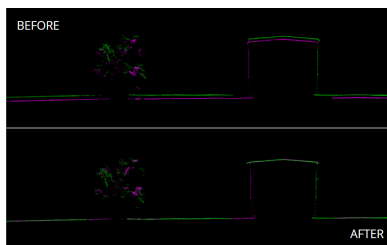
“TCarta looks forward to this partnership in striving for Seabed 2030 goals by contributing bathymetric data to in-fill the data gaps in existing hydrographic survey coverage.”

All data collected and shared with the Seabed 2030 Project is included in the GEBCO global grid, which is free and publicly available.

For more detailed information on The Nippon Foundation-GEBCO Seabed 2030 Project, please visit our website, seabed2030.org, like our Facebook page, follow us on Twitter @Seabed2030, or contact enquiries@seabed2030.org.



TECHNOLOGY



GeoCue Group Inc. and BayesMap Solutions LLC are pleased to announce the release of our new geometric correction software for the True View series of small Unmanned Aerial Systems

(sUAS) 3D Imaging Systems (3DIS®). Historically, geometric correction of lidar data has been an arduous process requiring Byzantine parameter adjustments and numerous trial runs. GeoCue has been working with BayesMap for the past several years to develop an add-on to our True View EVO software that allows “one button click” geometric correction of sUAS lidar data with no need to adjust algorithm parameters. This effort has culminated in the creation, by BayesMap, of StripAlign for EVO (SAfE).

Geometric errors are introduced into lidar data sets by two general mechanisms (assuming one has a good sensor to start with!); poor system calibration and/or GNSS/IMU estimation errors during flight. Calibration can be addressed by being very particular with system rigidity during design and developing exacting calibration procedures. GNSS and IMU estimation errors cannot be corrected via sensor design since these errors are inherent in the position and attitude sensors during flight. We do mitigate this in the True View sensors by using very high-quality Trimble/Applanix APX series Position and Orientation Systems (POS) but data can exhibit small geometric inconsistency, especially when combining data from multiple flights. BayesMap StripAlign for EVO detects and corrects these errors via an application of sensor-specific mathematical modeling.

SAfE is an optional extension to True View EVO, GeoCue’s post-processing and exploitation software bundled with True

View sensors, that integrates directly into the workflow using EVO's new Job Manager subsystem. The Job Manager allows users to work on other projects within EVO while SAfE is processing. SAfE is a fully automated process with no need for users to set project-specific "tuning" parameters or to move in and out of the EVO processing environment – press a button and it just works!

SAfE is available now. It was bundled with all True View 515, 635 and 640 3D Imaging Systems shipped after September 1st, 2021. It is available as an optional purchase for all other EVO-supported lidar sensors.



UP42 is pleased to announce the immediate availability of very high-resolution optical imagery from the Airbus Pléiades Neo constellation on the UP42 geospatial marketplace and developer platform. Pléiades Neo's unique combination of 30cm native spatial resolution, daily revisit, and faster tasking/data

delivery will benefit end users in all sectors, most notably Urban Mapping, Infrastructure Monitoring, Disaster Response, Insurance, and Agriculture.

The flexible UP42 platform provides the building blocks for geospatial companies to scale their products and businesses faster, further and cost effectively. UP42 customers may now plan, place, and track orders for Pléiades Neo acquisitions. For the many UP42 customers who access data and algorithms through the platform API, Pléiades Neo tasking will be available immediately.

The Pléiades Neo constellation represents a breakthrough in Earth observation technology from the acquisition capabilities in orbit to the production workflow on the ground. Developed by Airbus, the constellation currently includes two imaging satellites launched earlier this year with another two set for launch in 2022.

For more information, visit www.up42.com.

CALENDAR

- 14-18 December, **30th International Cartographic Conference & International Cartographic Exhibition**, Florence, Italy. For more information, visit <https://icaci.org/icc2021>.
- 1-3 February, 2022, **URIS LEAP Conference**. For more information, visit www.urisa.org/leap.
- 6-8 February 2022, **Geo Week 2022**, Denver, Colorado. For more information, visit www.geo-week.com/.

HTTP://DPAC.ASPRS.ORG

asprs
THE IMAGING & GEOSPATIAL INFORMATION SOCIETY

"The ASPRS Aerial Data Catalog is a tool allowing owners of aerial photography to list details and contact information about individual collections. By providing this free and open metadata catalog with no commercial interests, the Data Preservation and Archiving Committee (DPAC) aims to provide a definitive metadata resource for all users in the geospatial community to locate previously unknown imagery."

ASPRS AERIAL DATA CATALOG

"THE SOURCE FOR FINDING AERIAL COLLECTIONS"

- 1 USE** Use the catalog to browse over 5,000 entries from all 50 states and many countries. Millions of frames from as early as 1924!
- 2 SUPPLY** Caretakers of collections with, or without metadata, should contact DPAC to add their datasets to the catalog for free!
- 3 TELL** Spread the word about the catalog! New users and data collections are key to making this a useful tool for the community!

For More Details Contact:

David Ruiz druiz@quantumspatial.com 510-834-2001	David Day dday@kasurveys.com 215-677-3119
--	---



869 Giving Credit where it is Due

By Al Karlin, Ph.D., CMS-L, GISP

879 Semi-Automated Roller Parameters Extraction from Terrestrial Lidar

Sagar S. Deshpande, Mike Falk, and Nathan Plooster

Rollers are an integral part of a hot-rolling steel mill. They transport hot metal from one end of the mill to another. The quality of the steel highly depends on the surface quality of the rollers. This article presents semi-automated methodologies to extract roller parameters from terrestrial lidar points.

891 UAV Remote Sensing Assessment of Crop Growth

Freda Elikem Dorbu, Leila Hashemi-Beni, Ali Karimoddini, and Abolghasem Shahbazi

The introduction of unmanned-aerial-vehicle remote sensing for collecting high-spatial- and temporal-resolution imagery to derive crop-growth indicators and analyze and present timely results could potentially improve the management of agricultural businesses and enable farmers to apply appropriate solutions, leading to a better food-security framework. This article aims to analyze crop-growth indicators such as the normalized difference vegetation index (NDVI), crop height, and vegetated surface roughness to determine the growth of corn crops from planting to harvest.

901 MSegnet, a Practical Network for Building Detection from High Spatial Resolution Images

Bo Yu, Fang Chen, Ying Dong, Lei Wang, Ning Wang, and Aqiang Yang

Building detection in big earth data by remote sensing is crucial for urban development. However, improving its accuracy remains challenging due to complicated background objects and different viewing angles from various remotely sensed images. The hereto proposed methods predominantly focus on multi-scale feature learning, which omits features in multiple aspect ratios. Moreover, postprocessing is required to refine the segmentation performance. We propose modified semantic segmentation (MSegnet), a single-shot semantic segmentation model based on a matrix of convolution layers to extract features in multiple scales and aspect ratios.

907 Estimation of Rock Characteristics Based on Polarization Spectra: Surface Roughness, Composition, and Density

Feizhou Zhang, Xufang Liu, Yun Xiang, Zihan Zhang, Siyuan Liu, and Lei Yan

Surface polarization characteristics provide crucial structural information of the Earth's surface. As two key elements of the natural geographical environment, rocks and soils play an important role in the study of surface processes. Inherent surface characteristics, such as surface roughness, composition, and density are critical parameters for the remote monitoring of land surfaces as they affect the polarization characteristics of scattered light waves. In this article, we investigated the relationship between surface roughness, composition, and density, and the polarization spectra of limestone-dolomite series rock.

913 Automatic Registration of Mobile Mapping System Lidar Points and Panoramic-Image Sequences by Relative Orientation Model

Ningning Zhu, Bisheng Yang, Zhen Dong, Chi Chen, Xia Huang, and Wen Xiao

To register mobile mapping system (MMS) lidar points and panoramic-image sequences, a relative orientation model of panoramic images (PROM) is proposed.

923 Dense Bathymetry in Turbid Coastal Zones Using Airborne Hyperspectral Images

Steven Martinez Vargas, Claudio Delrieux, Katy L. Blanco, and Alejandro Vitale

We used airborne hyperspectral images to generate a dense survey of bathymetric data in the Bahía Blanca estuary (Buenos Aires Province, Argentina).



874 In Memoriam — James Bryan Mercer

COLUMNS

869 GIS Tips & Tricks—Giving Credit where it is Due

871 Grids and Datums Update

This month we look at Saint Vincent and the Grenadines

ANNOUNCEMENTS

870 New ASPRS Members

Join us in welcoming our newest members to ASPRS.

874 In Memoriam—James Bryan Mercer

875 Signatures

The Column of the Student Advisory Council

877 Headquarters News—2022 ASPRS Annual Election

878 Call for Submissions—AI-Based Environmental Monitoring with UAV Systems

DEPARTMENTS

865 Industry News

866 Calendar

900 In-Press *PE&RS* Articles

928 ASPRS Sustaining Members

See the Cover Description on Page 868

COVER DESCRIPTION

Landsat 9, a joint mission between NASA and the U.S. Geological Survey (USGS) that launched in September 2021, has collected its first images of Earth. Acquired on October 31, the “first-light” images provide a preview of how the mission will help people manage vital natural resources and understand the impacts of climate change. The new satellite extends an unparalleled data record that spans nearly 50 years of space-based observation of Earth.

“First light is a big milestone for Landsat users; it’s the first chance to really see the kind of quality that Landsat 9 provides,” said Jeff Masek, the mission’s project scientist at NASA. “When we have Landsat 9 operating in coordination with Landsat 8, it’s going to be this wealth of data, allowing us to monitor changes to our home planet every eight days.”

Landsat 9 carries two main instruments: the Operational Land Imager 2 (OLI-2), which detects visible, near-infrared, and shortwave-infrared light in nine wavelengths, and the Thermal Infrared Sensor 2 (TIRS-2), which detects thermal radiation in two wavelengths used to measure Earth’s surface temperatures. Together the instruments can provide users with essential information about crop health, irrigation use, water quality, wildfire severity, deforestation, glacial retreat, and urban expansion, especially when put in the context of the long Landsat data record.

The new satellite and instruments are quite similar in design to Landsat 8, which was launched in 2013 and remains in orbit. Together the two satellites will collect approximately 1,500 images of Earth’s surface every day, observing the entire planet every eight days.

Landsat 9 features several improvements, including higher radiometric resolution, allowing the sensors to detect more subtle differences in surface features, especially over darker areas like water or dense forests. With 14 -bit radiometric resolution, Landsat 9 can differentiate more than 16,000 shades of a given wavelength; Landsat 8 provides 12-bit data and 4,096 shades. Landsat 7, the satellite being replaced, detects only 256 shades with its 8-bit resolution.

“The data and images from Landsat 9 are expanding our capability to see how Earth has changed over decades,” said Karen St. Germain, Earth Science Division director for NASA. “In a changing climate, continuous and free access to Landsat data and to other data from NASA’s Earth observing fleet helps data users—including city planners, farmers, and scientists—plan for the future.”

The Landsat 9 team at NASA is now conducting a 100-day check-out—known as satellite commissioning—that involves testing the satellite’s systems and subsystems and calibrating its instruments in preparation for handing the mission over to USGS in January 2022. USGS will operate Landsat 9 along with Landsat 8. The new data will be available to the public for free from the USGS website once Landsat 9 begins normal operations.

“The incredible first pictures from the Landsat 9 satellite are a glimpse into the data that will help us make science-based decisions on key issues including water use, wildfire impacts, coral reef degradation, glacier and ice-shelf retreat, and tropical deforestation,” said USGS Acting Director David Applegate. “This historic moment is the culmination of our long partnership with NASA on Landsat 9’s development, launch, and initial operations, which will better support environmental sustainability, climate change resiliency, and economic growth.”

To see the additional first pictures and for more information, visit <https://landsat.visibleearth.nasa.gov/view.php?id=149058>.

NASA images by Matt Radcliff, using Landsat data from the U.S. Geological Survey. Story by Kate Ramsayer, with Mike Carlowicz.



PHOTOGRAMMETRIC ENGINEERING & REMOTE SENSING

JOURNAL STAFF

Publisher ASPRS

Editor-In-Chief Alper Yilmaz

Assistant Director — Publications Rae Kelley

Electronic Publications Manager/Graphic

Artist Matthew Austin

Photogrammetric Engineering & Remote Sensing is the official journal of the American Society for Photogrammetry and Remote Sensing. It is devoted to the exchange of ideas and information about the applications of photogrammetry, remote sensing, and geographic information systems. The technical activities of the Society are conducted through the following Technical Divisions: Geographic Information Systems, Photogrammetric Applications, Lidar, Primary Data Acquisition, Professional Practice, and Remote Sensing Applications. Additional information on the functioning of the Technical Divisions and the Society can be found in the Yearbook issue of *PE&RS*.

Correspondence relating to all business and editorial matters pertaining to this and other Society publications should be directed to the American Society for Photogrammetry and Remote Sensing, 425 Barlow Place, Suite 210, Bethesda, Maryland 20814-2144, including inquiries, memberships, subscriptions, changes in address, manuscripts for publication, advertising, back issues, and publications. The telephone number of the Society Headquarters is 301-493-0290; the fax number is 225-408-4422; web address is www.asprs.org.

PE&RS. *PE&RS* (ISSN0099-1112) is published monthly by the American Society for Photogrammetry and Remote Sensing, 425 Barlow Place, Suite 210, Bethesda, Maryland 20814-2144. Periodicals postage paid at Bethesda, Maryland and at additional mailing offices.

SUBSCRIPTION. For the 2021 subscription year, ASPRS is offering two options to our *PE&RS* subscribers — an e-Subscription and the print edition. E-subscribers can plus-up their subscriptions with printed copies for a small additional charge. Print and Electronic subscriptions are on a calendar-year basis that runs from January through December. We recommend that customers who choose both e-Subscription and print (e-Subscription + Print) renew on a calendar-year basis.

The rate of the e-Subscription (digital) Site License Only for USA and Non-USA is \$1000.00 USD. e-Subscription (digital) Site License Only for Canada* is \$1049.00 USD. e-Subscription (digital) Plus Print for USA is \$1365.00 USD. e-Subscription (digital) Plus Print for Canada* is \$1424.00 USD. e-Subscription (digital) Plus Print for Non-USA is \$1395.00 USD. Printed-Subscription Only for USA is \$1065.00 USD. Printed-Subscription Only for Canada* is \$1124.00 USD. Printed-Subscription Only for Non-USA is \$1195.00 USD. *Note: e-Subscription/Printed-Subscription Only/e-Subscription Plus Print for Canada include 5% of the total amount for Canada’s Goods and Services Tax (GST #135123065). **PLEASE NOTE: All Subscription Agencies receive a 20.00 USD discount.**

POSTMASTER. Send address changes to *PE&RS*, ASPRS Headquarters, 425 Barlow Place, Suite 210, Bethesda, Maryland 20814-2144. CDN CPM # (40020812)

MEMBERSHIP. Membership is open to any person actively engaged in the practice of photogrammetry, photointerpretation, remote sensing and geographic information systems; or who by means of education or profession is interested in the application or development of these arts and sciences. Membership is for one year, with renewal based on the anniversary date of the month joined. Membership Dues include a 12-month electronic subscription to *PE&RS*. Or you can receive the print copy of *PE&RS* Journal which is available to all member types for an additional fee of \$60.00 USD for shipping USA, \$65.00 USD for Canada, or \$75.00 USD for international shipping. Dues for ASPRS Members outside of the U.S. will now be the same as for members residing in the U.S. Annual dues for Regular members (Active Member) is \$150.00 USD; for Student members \$50.00 USD for USA and Canada \$53.00 USD; \$60.00 USD for Other Foreign members. A tax of 5% for Canada’s Goods and Service Tax (GST #135123065) is applied to all members residing in Canada.

COPYRIGHT 2021. Copyright by the American Society for Photogrammetry and Remote Sensing. Reproduction of this issue or any part thereof (except short quotations for use in preparing technical and scientific papers) may be made only after obtaining the specific approval of the Managing Editor. The Society is not responsible for any statements made or opinions expressed in technical papers, advertisements, or other portions of this publication. Printed in the United States of America.

Giving Credit where it is Due

For those who have been following this column, you know that one of my mantras regarding GIS-based cartography is “never accept the defaults.” This mantra extends to the use of pre-constructed basemaps. While I encourage my students to construct their basemaps from scratch, that is, publicly available GIS data, sometimes it is just too convenient to use a pre-constructed basemap and then add your relevant data directly to it. While that basemap may be cartographically pleasing and exactly what you need for your map product, it will generally come with the source and credits imbedded into the graphic. Remember that although it is absolutely necessary to retain that information on the map, the font, text size, color, placement, etc. may be inharmonious with your map. So...here is a tip on how to adjust the credits.

IN ARCGIS DESKTOP

Typically, when you use an Esri pre-constructed basemap, the credits will appear in the lower right-hand portion of your map (Figure 1), as:

Esri, HERE, Garmin, (c) OpenStreetMap contributors, and the GIS user community

Figure 1. Typical Esri Basemap Credit Display.

To convert the credit text into editable text that you can adjust, from the Main Toolbar, choose:

Insert | Dynamic Text and choose the “Service Layer Credits” option (Figure 2).

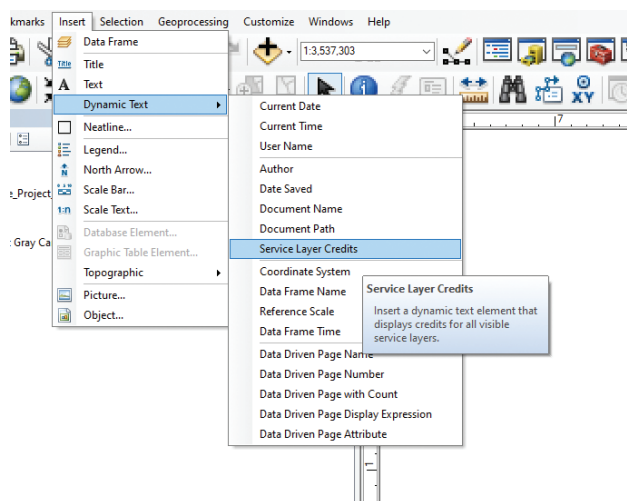


Figure 2. Path from the ArcGIS Desktop Main Menu Bar to alter the Basemap Credit Text.

ArcGIS will select the Service Credits, reformat the text, and convert them into text. You will see the handles (Figure 3) around the text which you can now modify as you need for your map product. Of course, when you can update the text, it is a good idea not to alter the words or remove them completely from the map.

Service Layer Credits: Esri, HERE, Garmin, (c) OpenStreetMap contributors, and the GIS user community

Figure 3. Service Credits converted to Editable Text in ArcGIS Desktop.

IN ARCGIS PRO

The process is much the same in ArcGIS Pro. In a Layout Window (Figure 4) containing the Esri basemap,

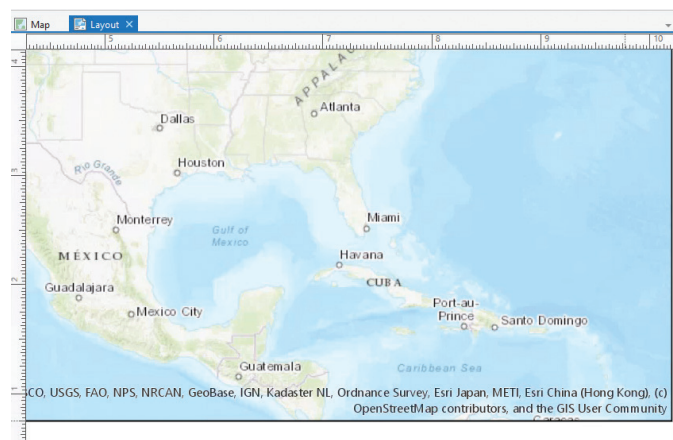


Figure 4. ArcGIS Pro Layout Window with Esri Basemap showing Service Credits.

Select the “Dynamic Text” dropdown (Figure 5) and scroll down to choose “Service Layer Credits”.

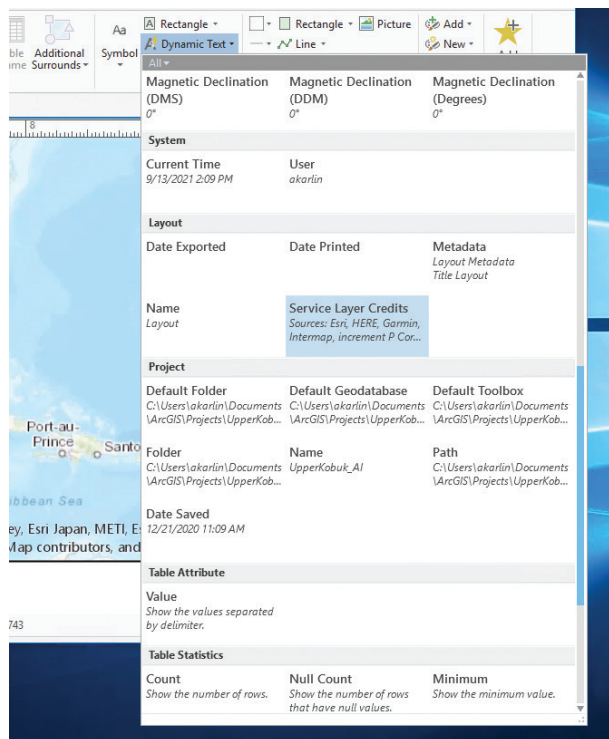


Figure 5. Dynamic Text Dropdown Menu in ArcGIS Pro.

Clicking on the credits on the map will select the text (Figure 6), which you can now adjust for your map.

And it is that easy to update the service credits for your basemap.



Figure 6. Dynamic Text shown as an Editable Feature in ArcGIS Pro Layout Window.

Just a quick note, Esri has moved many of the basemaps to Mature Support (<https://www.esri.com/arcgis-blog/products/arcgis-online/announcements/reminder-raster-basemaps-moved-to-mature-support/>), including the World Dark Gray and the World Street Maps. That means that these maps will no longer be updated or revised. These maps are being replaced with vector versions to provide for faster rendering. If you have these basemaps in your map documents, you might want to check to make sure that you are using the most up-to-date versions.

Send your questions, comments, and tips to GISTT@ASPRS.org.

Al Karlin, Ph.D., CMS-L, GISP is with Dewberry's Geospatial and Technology Services group in Tampa, FL. As a senior geospatial scientist, Al works with all aspects of Lidar, remote sensing, photogrammetry, and GIS-related projects.

NEW ASPRS MEMBERS

ASPRS would like to welcome the following new members!

Mahnaz Dil Afroz

Zia Ahmed

Elliot Anderson

Curtis Beloy

Kalynn Bronson

Janet Bull

Brian Fitzpatrick

Dale Fried

Russell Stuart Godkin

Jamie Goosney

Michelle Helms

James Edward Jones, III

Daniel Koklauner

Wenliang Li

Yuchi Ma

Brooke Obrey

Seyi Ogundeji

Kyle James Paulekas

Indu Miriam Philip

Hope Piper

Shaifali Prajapati

Maxwell Angus Pratt

Brooke Radding

Karl Schwab

Fitsum Tilahun Teshome

Alejandro Torres

Victor Toth

Gene Trantham

Stephanie Willsey

Zachary Winters

FOR MORE INFORMATION ON ASPRS MEMBERSHIP, VISIT
[HTTP://WWW.ASPRS.ORG/JOIN-NOW](http://www.asprs.org/join-now)

ASPRS WORKSHOP SERIES



It's not too late to earn Professional Development Hours

Miss an ASPRS Workshop or GeoByte? Don't worry! Many ASPRS events are available through our online learning catalog.

<https://asprs.prolearn.io/catalog>

Image Priscilla Du Preez on Unsplash.



GRIDS & DATUMS

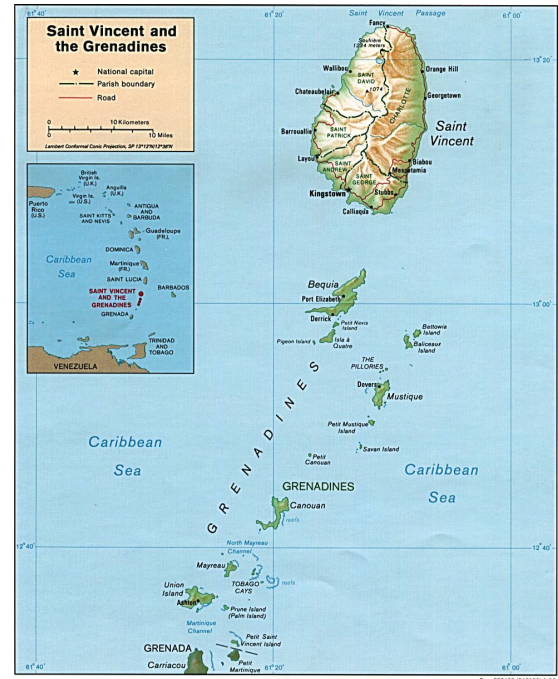
BY Clifford J. Mugnier, CP, CMS, FASPRS

SAINT VINCENT AND THE GRENADINES

The Grids & Datums column has completed an exploration of every country on the Earth. For those who did not get to enjoy this world tour the first time, *PE&RS* is reprinting prior articles from the column. This month's article on Saint Vincent and the Grenadines was originally printed in 2004 but contains updates to their coordinate system since then.

The cannibal warrior Caribs arrived in Saint Vincent around the 14th century, and they strongly resisted colonial settlers until the 18th century. Christopher Columbus probably sighted the island on 22 January 1498 (St. Vincent's Day). In 1673 the first African slaves were shipwrecked in the Grenadines, but they managed to get to St. Vincent, intermarry with the Caribs, and became known as the "Black Caribs." In 1795 the Caribs un-successfully rose in revolt against the British, and 5,000 or more of them were deported to Roatan Island off the coast of Honduras. The hurricane of 1898 and the volcanic eruption of 1902 were disastrous to the economy. In 1958 Saint Vincent joined the West Indies Federation, it received a new constitution in 1960, and it became a state in association with the United Kingdom (*PE&RS, October 2003*) in 1969. Independence for Saint Vincent and the Grenadines was achieved on 27 October 1979. *Encyclopedia Britannica* says, "In 1979 the Soufrière volcano (1,234 m) erupted once again, damaging agriculture and the tourist trade. Hurricane Allen virtually wiped out the all-important banana crop in 1980."

Slightly less than twice the size of Washington, D.C., there are 32 Grenadine islands and cays, of which the largest are Bequia, Mustique, Canouan, and Union. Of a total 389 km², the area of Saint Vincent is 344 km². Some of the smaller islands are privately owned-probably not by retired cartographers. Part of the Windward Islands, the name dates back to the 18th century when English ships bound for Jamaica followed the trade-wind passage, and stopped at islands along the way. The islands constitute a north-south chain in the southern section of the Lesser Antilles and share a volcanic rock formation.



The earliest geodetic survey of Saint Vincent was of Fort Charlotte (lighthouse) in 1946 by the Hydrographic Service of the British Admiralty on 04 December. The coordinates of Fort Charlotte (V.1) are $\Phi_0 = 13^\circ 09' 24'' N$ and $\Lambda_0 = 61^\circ 14' 43''$ West of Greenwich, the reference azimuth from "V. 1" to "V. 3" is $\alpha_0 = 107^\circ 30' 13.42''$, the elevation of "V.2" is: $H_0 = 370.36$ feet, and the baseline length (measured in 1945 by the Royal Engineers [R.E.] by catenary) from "V.30" to "V.32" is 2,347.504 m. (Invar tapes or wires were commonly calibrated for a standard length by being supported only at the ends of the tape or wire with a specific tension, thus the sag formed a catenary curve). The reference ellipsoid is the Clarke 1880 where: $a = 6,378,249.136$ m, and $1/f = 293.46631$, the same parameters as for Jamaica (*PE&RS, May 2003*). Courtesy of the U.K. Military Survey, "The height of V.2 was established by the R.E. party by leveling from a Bench Mark on a step of the Aquatic Club, Kingstown; the height of the Bench Mark

Photogrammetric Engineering & Remote Sensing
Vol. 87, No. 12, December 2021, pp. 871-881.
0099-1112/21/871-881

© 2021 American Society for Photogrammetry and Remote Sensing
doi: 10.14358/PERS.87.12.871

was established by the R.E. party from mean tide gauge reading taken over a period of four months.” (*Note that a Metonic cycle is 18.67 years!* – Ed.)

The coordinate system used by the Lands and Surveys Department of Saint Vincent and the Grenadines is the British West Indies (BWI) Grid which is based on the Transverse Mercator projection where the Central Meridian $\lambda_0 = 62^\circ$ W, the Scale Factor at Origin $m_0 = 1999/2000 = 0.9995$, and the False Easting is 400 km. Note that the unit of measurement for this BWI Grid is the meter where 1 meter = 3.2828456 feet. The strange conversion factor is likely due to an earlier colonial length standard that was used for property surveys; a common quirk of old British Colonies throughout the world.

In 1996, the United States National Geodetic Survey (NGS) performed a GPS survey of selected points on the island of Saint Vincent. The NGS occupied a number of existing survey control marks previously set by the Lands and Surveys Department (L&SD), and I was successful in obtaining the classical St. Vincent Datum of 1946 coordinates of four of the six points collocated with GPS observations. Unfortunately, I do not have a record of who it was that sent the information to me on official L&SD stationery. I ran a solution for the three parameters of geocentric translation for those four points; two were listed as First Order and two were listed as Second Order. The resultant relation I derived from the St. Vincent Datum of 1946 to WGS 84 is $\Delta X = +196$ m, $\Delta Y = +332$ m, and $\Delta Z = +275$ m. I estimate the horizontal accuracy to be good to about 1 meter for the island of Saint Vincent. Because I had zero data on collocated points on any of the other islands, my guess is that the three-parameter shift values listed above are likely good to no more than a few meters for the remainder of the islands to the south because of the usually superb quality of work produced by the Royal Engineers. Thanks to Dave Doyle of NGS for the NAD83 coordinates of Saint Vincent.

St. Vincent and the Grenadines Update

New 2019 publication on Limits in the Seas from the U.S. Dept. of State: <https://www.state.gov/wp-content/uploads/2019/10/LIS-144.pdf>

2007 Update on history details from Mr. Russell Fox, Librarian for the Directorate of Overseas Surveys:

“DOS* work in St Vincent and the Grenadines

Summarised from DOS Annual Reports and notes held by Russell Fox (OS International Library Manager 1994-2004)

- DOS is used here as shorthand for the Directorate of Colonial Surveys (DCS, 1946-57), Directorate of Overseas Surveys (DOS, 1957-84), Overseas Surveys Directorate, Ordnance Survey (OSD, 1984-91) and Ordnance Survey International (1991-2004).

Other abbreviations: SVSD St Vincent Survey Department
SVG St Vincent Government
RE Royal Engineers
RN Royal Navy

Surveys and Computations

- 1947/48—RE 1945 primary trig of St V. computed by DCS; co-ords issued.
- 1951/52—DCS Senior Surveyor W H Young, and two surveyors recruited from Trinidad by the SVG, identified existing trigs on air photos and established 93 new trigs to provide extra control for 25K mapping, road traversing and cadastral surveys. Extra height control was fixed for 25K contouring.
- 1952/53—St Vincent. Control for 25K mapping completed. Closer control established for cadastral surveys. Many existing property beacons were tied in during this work. Subsequent investigation showed gross error in the existing property surveys. Brigadier Hotine, Director of Colonial Surveys, visited St V. in Dec 1952 and decided that a complete cadastral re-survey of the island was necessary. Mr Young was instructed to commence this work while a suitably qualified surveyor could be recruited to continue the work permanently.
- 1953/54—St Vincent. Cadastral surveys continued. Little cadastral re-survey work was possible owing to ad hoc surveys urgently required by SVG and carried out up to May 1954. The cadastral re-survey was postponed until trained staff were available. Five Vincentians were selected for the two-year survey training course in Trinidad. [Mr Young probably left St V. in mid-1954]. All trig computations were completed at DCS and lists prepared for issue.
- 1957—Mr Young visited St V. in May and Sep to advise on local surveys and do 25K field completion.
- 1962/63—The Grenadines. Tellurometer traversing & trig observed from St V. to Grenada by DOS/SVSD/RN. 115 stations built, 96 observed, 91 lines measured. Preliminary investigation of existing control in the Grenadines completed at DOS.
- 1964—The Grenadines computations were completed at DOS. Co-ords and heights computed for 121 stations. Two sets of co-ords were produced, one on St V. datum and the other on Grenada datum.
- 1965—A DOS surveyor spent one week in St V. assisting SVSD in premarking control for large scale mapping and measuring 11 Tellurometer lines to fix additional stations.
- 1971-73—St Vincent. A DOS field party of 4 surveyors established a dense network of fourth order traverse stations for cadastral purposes. A prime-

ter Tellurometer traverse, with a cross-island link, was observed to check the scale of the existing trig. Additional control was observed for the Kingstown 2.5K mapping. Photo control for 5K mapping of the west coast was observed. In all, some 700 new stations were established. Field revision was carried out for the 25K third edition mapping. During Nov 1971 the Soufriere volcano became active. DOS surveyors and geologists from Trinidad made periodic observations of the level of the crater lake and lava islands in it. Geodimeter observations were made between Chateaubelair and Soufriere to detect earth movements associated with recent eruptions. At DOS the perimeter Tellurometer traverse was computed, revealing inconsistencies in the scale of the existing network. DOS prepared to carry out a comprehensive re-adjustment of the main surveys observed since 1944/45 [but the re-adjustment was not done until the late 1970s].

- 1972-74—Grenadines. Extra control was established for 2.5K mapping in the islands. 65 new stations were fixed by EDM traverse and trig. On Mustique, existing Fairey Surveys control points were re-occupied by DOS; only one new station was required there. DOS computed final co-ords and provisional heights for Bequia, Mustique, Cannouan, Mayreau and Union islands.
- 1976/77—DOS computed provisional co-ords and heights for St V. from the 1972 fieldwork.
- 1978-80—St Vincent. Two DOS surveyors were detached from the St Lucia field party for a month to recce and photo-identify control for 2.5K mapping N of Kingstown and on the E coast.
- St Vincent and the Grenadines. DOS re-computed all surveys in one adjustment comprising 1528 observation equations in 416 unknowns. Final co-ords were produced for 209 points. Two further adjustments were carried out to incorporate the minor control and a final co-ordinate list of 1177 points was issued.
- 1980-82—The DOS Caribbean Map Revision/Field Completion team and an SVSD surveyor carried out field completion and 2.5K map revision in St Vincent and the Grenadines, plus 5K and 10K map revision on some islands of the Grenadines. Plan and height control for 2.5K mapping in the Grenadines was observed and then computed at DOS.
- 1982/83—2.5K field completion was completed on St Vincent and Union islands by two surveyors from DOS and SVSD. The DOS party closed down in 1983, SVSD continuing the field completion work.

Aerial Photography

DOS Contract no.	Year	Scale	Coverage
2	1950	18K	St Vincent
3	1951	14-18K	W & central St Vincent
RAF	1965	25K	The Grenadines
85	1966	6-12.5K	W & SE St V. and Mustique
RAF	1966	?	Partial coverage of the Grenadines
113	1970	12.5K	Central & E St Vincent
116	1971	20K	W St Vincent
116	1971	12.5K	The Grenadines
RAF	1972	20K	Partial coverage of St Vincent
RN	1972	?	Helicopter phy of Ronde and Bequia
163	1977	12.5K	W, S & E St Vincent
186	1981	25K	St Vincent
186	1981	12.5K	Bequia, Mustique and Union islands and parts of St Vincent

I believe that the RAF flew some photography in 1946 but I have no details.

DOS Mapping

Scale	Series	Year	Coverage
200K	?	?	St Vincent & the Grenadines
50K	DOS417	1961-91, 8 eds	St Vincent. Ed 8 has the St Vincent Grenadines on the reverse
50K	DOS417	1991	St V. Grenadines
25K	DOS317	1959-83, 5 eds	St Vincent in 2 sheets
25K	DOS344	1967-70	The Grenadines in 5(?) sheets; this was a dual scale series with DOS244
10K	DOS244	1967-70	The Grenadines in ? sheets; dual scale series with DOS344
10K	DOS217	1983-88	St V Grenadines in 5 sheets

I may have omitted some printed, large-scale editions from the 1970s. I have not attempted to summarise here any DOS geological and land use mapping of St Vincent and the Grenadines.

RDF, 15.7.07”

The contents of this column reflect the views of the author, who is responsible for the facts and accuracy of the data presented herein. The contents do not necessarily reflect the official views or policies of the American Society for Photogrammetry and Remote Sensing and/or the Louisiana State University Center for GeoInformatics (C⁴G).

This column was previously published in *PE&RS*.

James Bryan Mercer

1940-2021



Dr. Bryan Mercer passed away peacefully on September 30, 2021 in Calgary, Alberta. For more than 30 years, he was a strong supporter of ASPRS, never missing the Annual and the former Fall meetings. In addition, he was also represented the ASPRS community internationally at ISPRS.

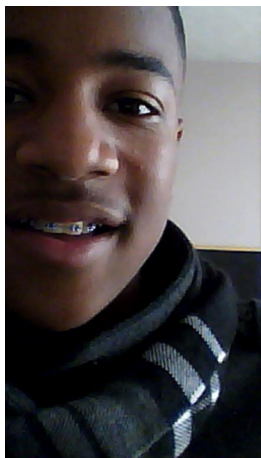
Bryan received his B.Sc. in Physics from the University of Alberta in 1962, and then a PhD in Astrophysics in 1967 at the University of Calgary. As a postdoc and young researcher, he travelled a lot and spent longer times in Italy and UK before settling back to Calgary, where he played a key role in initiating an arctic remote sensing program. In 1984, he became Chief Scientist at Intermap Technologies, a position he held until his retirement. He focused on radar technologies, in particular airborne SAR, and soon he turned out to be a world renowned expert in the commercial SAR practice, including data acquisition, processing and product development.

Notably, he had the classical geomatics trait, being extremely careful about using rigorous QA/QC processes. For 12 years, he jointly led ISPRS Working Groups on SAR and lidar technologies.

Bryan, a born optimist was not only a very bright scientist, but he was an exceptionally kind and supportive person. He had warm words for everyone around him and, being an excellent speaker, was always ready to share some nice stories. As a globetrotter scientist, he met many people all over the world and developed long-lasting friendships. Bryan was a well-rounded person, as besides being a devoted professional, he had a life outside of the office too. He loved nature, the mountains, especially the Canadian Rockies where he found lots of joy, including, camping, hiking, skiing and biking. He liked movies and books; a good book as well as a flask of Crown Royal had always accompanied him on his numerous trips all over the world. While he loved jazz in his entire life, it was fairly late when he started to play on the saxophone, something he could enjoy till the very end.

Bryan is survived by his wife Diane; his children Larissa and David and stepdaughter Robin; grandchildren Caelan, Athan, Noah, Maya and Fiona. He will be missed by his family, friends and colleagues.

~Charles Toth, Past President—ASPRS



Too young to drive the car? Perhaps!

But not too young to be curious about geospatial sciences.

The ASPRS Foundation was established to advance the understanding and use of spatial data for the betterment of humankind. The Foundation provides grants, scholarships, loans and other forms of aid to individuals or organizations pursuing knowledge of imaging and geospatial information science and technology, and their applications across the scientific, governmental, and commercial sectors.

Support the Foundation, because when he is ready so will we.

asprsfoundation.org/donate

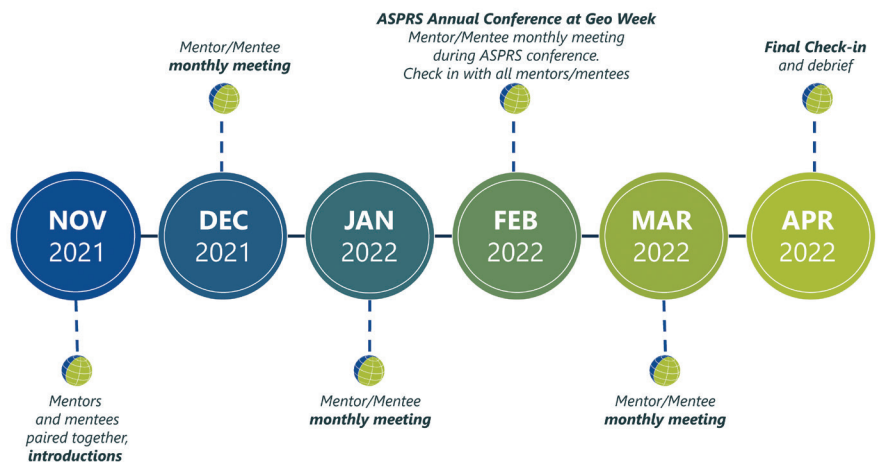


WHAT'S NEW WITH THE ASPRS STUDENT ADVISORY COUNCIL (SAC)!

After months of hard work, we are delighted to talk about the successful launch of the mentor/mentee program. This program aims to provide students with a platform to assist them in creating their own career paths in the field of remote sensing and geosciences while helping students build stronger connections in the industry and academia.

The details of the program are as follows:

- Mentor/Mentee pairs will meet in person or virtually once a month for at least one hour. Meetings should be flexible to accommodate the schedules of all participants. Mentor/Mentee pairs can be provided a zoom link if needed!
- This program is already in motion as mentor-mentee pairs were assigned in November.
- There will be a check-in with all mentors and mentees in February during Geo Week, and a final check-in and debrief in April 2022. An article on the program and the mentor/mentee pairs will be featured in the June 2022 issue of *PE&RS*!
- A total of five (5) pairs are chosen for this pilot program, and any mentors or mentees who did not get to participate will be given the chance the following year. If you are interested in becoming a mentor for the next year, please send us an email at sac@asprs.org.



Our sincere appreciation to all ASPRS professionals who are helping the next generation of GIS, photogrammetry and remote sensing specialists.

Join us in congratulating our new Chair, Lauren McKinney-Wise, who was previously serving as Deputy Chair.

If you are interested in SAC activities:

- Participate in our bi-monthly Zoom call scheduled for every other Thursday from 10:00-11:00 AM PST!
» Login with the QR code



ASPRS STUDENT ADVISORY COUNCIL

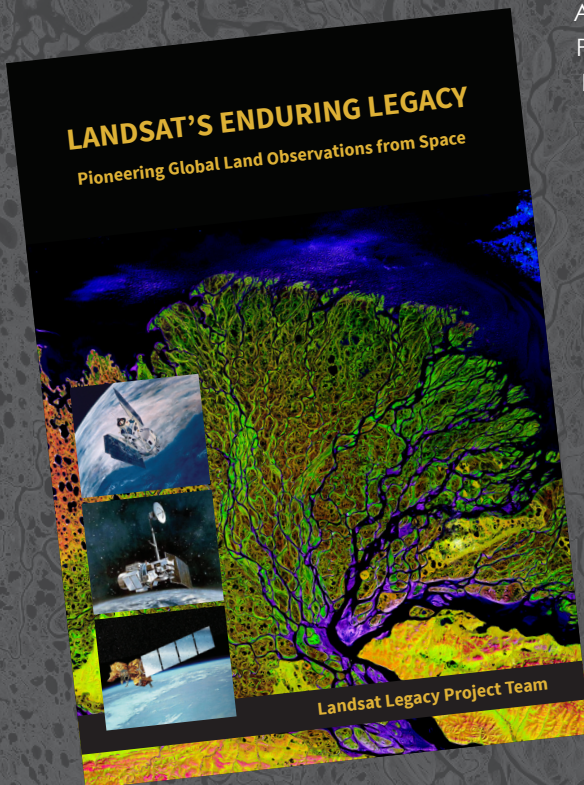
LAUREN MCKINNEY-WISE
COUNCIL CHAIR
OSCAR DURAN
DEPUTY COUNCIL CHAIR
CHUKWUMA JOHN OKOLIE
COMMUNICATIONS COUNCIL MEMBER

TBD
EDUCATION & PROFESSIONAL NETWORKING CHAIR
ALI ALRUZUQ
DEPUTY EDUCATION & PROFESSIONAL NETWORKING CHAIR
TESINI PRECIOSU DOMBO
COMMUNICATIONS COUNCIL MEMBER

RABIA MUNSAF KHAN
COMMUNICATIONS COUNCIL CHAIR
KENNETH EKPETERE
CHAPTERS COMMITTEE CHAIR
FREDA ELIKEM DORBU
COMMUNICATIONS COUNCIL MEMBER

LANDSAT'S ENDURING LEGACY

PIONEERING GLOBAL LAND OBSERVATIONS FROM SPACE



After more than 15 years of research and writing, the Landsat Legacy Project Team published, in collaboration with the American Society for Photogrammetry and Remote Sensing (ASPRS), a seminal work on the nearly half-century of monitoring the Earth's lands with Landsat. Born of technologies that evolved from the Second World War, Landsat not only pioneered global land monitoring but in the process drove innovation in digital imaging technologies and encouraged development of global imagery archives. Access to this imagery led to early breakthroughs in natural resources assessments, particularly for agriculture, forestry, and geology. The technical Landsat remote sensing revolution was not simple or straightforward. Early conflicts between civilian and defense satellite remote sensing users gave way to disagreements over whether the Landsat system should be a public service or a private enterprise. The failed attempts to privatize Landsat nearly led to its demise. Only the combined engagement of civilian and defense organizations ultimately saved this pioneer satellite land monitoring program. With the emergence of 21st century Earth system science research, the full value of the Landsat concept and its continuous 45-year global archive has been recognized and embraced. Discussion of Landsat's future continues but its heritage will not be forgotten.

The pioneering satellite system's vital history is captured in this notable volume on Landsat's Enduring Legacy.

Landsat Legacy Project Team

Samuel N. Goward
Darrel L. Williams
Terry Arvidson
Laura E. P. Rocchio
James R. Irons
Carol A. Russell
Shaida S. Johnston

Landsat's Enduring Legacy

Hardback, 2017, ISBN 1-57083-101-7

Student	\$36*
Member	\$48*
Non-member	\$60*

* Plus shipping

Order online at
www.asprs.org/landsat



asprs THE IMAGING & GEOSPATIAL
INFORMATION SOCIETY

JOURNAL STAFF

Editor-In-Chief

Alper Yilmaz, Ph.D., PERSeditor@asprs.org

Associate Editors

Rongjun Qin, Ph.D., qin.324@osu.edu

Michael Yang, Ph.D., michael.yang@utwente.nl

Petra Helmholz, Ph.D., Petra.Helmholz@curtin.edu.au

Bo Wu, Ph.D., bo.wu@polyu.edu.hk

Clement Mallet, Ph.D., clemallet@gmail.com

Prasad Thenkabail, Ph.D., pthenkabail@usgs.gov

Ruisheng Wang, Ph.D., ruiswang@ucalgary.ca

Desheng Liu, Ph.D., liu.738@osu.edu

Valérie Gouet-Brunet, Ph.D., valerie.gouet@ign.fr

Dorota Iwaszczuk, Ph.D., dorota.iwaszczuk@tum.de

Qunming Wang, Ph.D., wqm11111@126.com

Filiz Sunar, Ph.D., fsunar@itu.edu.tr

Norbert Pfeifer, np@ipf.tuwien.ac.at

Jan Dirk Wegner, jan.wegner@geod.baug.ethz.ch

Hongyan Zhang, zhanghongyan@whu.edu.cn

Dongdong Wang, Ph.D., ddwang@umd.edu

Zhenfeng Shao, Ph.D., shaozhenfeng@whu.edu.cn

Ribana Roscher, Ph.D., ribana.roscher@uni-bonn.de

Sidike Paheding, Ph.D., spahedin@mtu.edu

Contributing Editors

Highlight Editor

Jie Shan, Ph.D., jshan@ecn.purdue.edu

Feature Articles

Michael Joos, CP, GISP, featureeditor@asprs.org

Grids & Datums Column

Clifford J. Mugnier, C.P., C.M.S., cjmce@lsu.edu

Book Reviews

Sagar Deshpande, Ph.D., bookreview@asprs.org

Mapping Matters Column

Qassim Abdullah, Ph.D., Mapping_Matters@asprs.org

Sector Insight

Lucia Lovison-Golob, Ph.D., lucia.lovison@sat-drones.com

Bob Ryerson, Ph.D., FASPRS, bryerson@kimgeomatics.com

GIS Tips & Tricks

Alvan Karlin, Ph.D., CMS-L, GISP akarlin@Dewberry.com

ASPRS Staff

Assistant Director — Publications

Rae Kelley, rkelley@asprs.org

Electronic Publications Manager/Graphic Artist

Matthew Austin, maustin@asprs.org

Advertising Sales Representative

Bill Spilman, bill@innovativemediasolutions.com

2022 ASPRS ANNUAL ELECTION

The following candidates are running for office in the 2022 ASPRS Annual Election.

- Ballot was sent to all active members of ASPRS on November 30, 2021.
- Join or renew no later than January 15, 2022 to be eligible to vote!
- Final deadline for voting is January 18, 2022.
- Ballots will be counted on January 19, 2022.
- Winners will be notified on January 20, 2022.
- Installation of Officers will take place at the 2022 ASPRS Annual Business Meeting at Geo Week in Denver, Colorado on February 8, 2022

Candidates for Vice President from the Government Sector

- Bandana Kar, *Oak Ridge National Laboratory*
- John McCombs, *NOAA Coastal Services Center*

Candidates for Assistant Division Director

• GIS Division

- » Madison Fung, *University of Oregon*
- » Jin Lee, *George Mason University*

• Lidar

- » Matt Bethel, *Merrick & Company*
- » Paul Manley, *Missouri University of Science and Technology/Surdex*

• Photogrammetric Applications

- » Andrew Lassiter, *University of Florida*
- » Henry (Hank) Theiss, *University of Arkansas*

• Unmanned Autonomous Systems

- » Paul Crocker, *Ayres Associates*
- » Rusty Steel, *Half Associates, Inc.*
- » Bahram Salehi, *SUNY-ESF*

The 2022 ASPRS Annual Election will be conducted by electronic ballot using SurveyMonkey.

Call for Submissions

AI-Based Environmental Monitoring with UAV Systems

Photogrammetric Engineering and Remote Sensing (PE&RS) is seeking submissions for a special issue on AI-Based Environmental Monitoring with UAV Systems.

Global warming and climate change have become the most important factor threatening the world. Climate change results in dramatical environmental hazards and threatens the planet and human life. A wide variety of policies have been proposed to decrease the effects of global warming and climate change. The most important one is the Paris Agreement which aims to limit global warming to well below two degrees Celcius. Many countries have formulated long term low greenhouse gas emission development strategies related to the Paris Agreement which aimed to meet the essential strategies addressing issues with climate change, environmental protection and low carbon.

The astonishing developments on unmanned aerial vehicle (UAV) systems and artificial intelligence (AI) technologies enables a great opportunity to monitor the environment and propose reliable solutions to restore and preserve the planet and human health.

Data acquisition and processing paradigm has been changed as a result of technological developments. It is obvious that new solutions, innovative approaches will make significant contributions to solve the problems which our planet is facing. UAV data can be collected by various platforms (planes or helicopters, fixed wing systems, drones) and sensors for earth observation and sustainable environmental monitoring which are also utilized by the United Nations to support the delivery of its mandates, resolutions, and activities.

UAV based earth observation data and AI techniques have a wide range of applications such as risk management, disaster monitoring and assessment, environmental impact evaluation and restoration, monitoring agriculture and food cycles, urban analysis, digital twin and smart city applications and providing increased situation awareness. This growth of widely available UAV data associated with the exponential increase in digital computing power, machine learning and artificial intelligence plays a key role in the environmental monitoring and solution generation of geospatial information for the benefit of humans and the planet.

The proposed special issue aims to contributes ASPRS's key mission on 'Simplify and promote the use of image-based geospatial technologies for the end-user', 'Promote collaboration between end users and geospatial experts to match data and technology to applications and solutions' and 'promote the transfer of geospatial data and information technology to developing nations' by

serving as an innovative knowledge exchange platform for authors from the globe to deliberate on the latest advancements, state-of-the-art developments and solutions that can help the community to solve many real-world challenges on the topic of "AI-Based Environmental Monitoring with UAV Systems."

This special issue aims to bring researchers to share knowledge and their expertise about state-of-art developments and contribute to the goal of a livable world by integrating human creativity with UAV and AI technologies for environmental monitoring to combat global threats on ecosystems. We wish to discuss the latest developments, opportunities and challenges that can solve many real-world challenges in environmental monitoring including but not limited to:

- AI-Based UAV and GIS Applications
- AI-Based Object Detection and Recognition from UAV Imagery
- AI-Based Digital Twin Applications
- AI-Based Smart City Applications

Papers must be original contributions, not previously published or submitted to other journals. Submissions based on previous published or submitted conference papers may be considered provided they are considerably improved and extended. Papers must follow the instructions for authors at <http://asprs-pers.edmgr.com/>.

**Deadline for Manuscript Submission
May 1, 2022**

**Submit your Manuscript to
<http://asprs-pers.edmgr.com>**

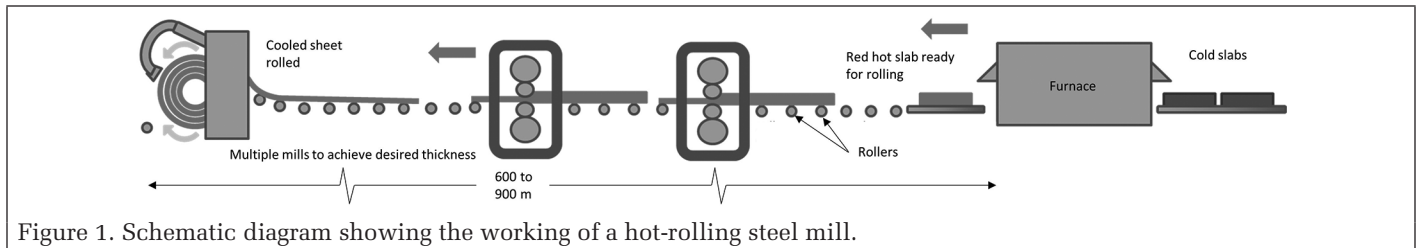
Guest Editor

Tolga Bakirman, PhD, Yildiz Technical University, Turkey

Dr. Tolga Bakirman. bakirman@yildiz.edu.tr is an assistant professor at Yildiz Technical University in the Department of Geomatic Engineering.

Semi-Automated Roller Parameters Extraction from Terrestrial Lidar

Sagar S. Deshpande, Mike Falk, and Nathan Plooster



Abstract

Rollers are an integral part of a hot-rolling steel mill. They transport hot metal from one end of the mill to another. The quality of the steel highly depends on the surface quality of the rollers. This paper presents semi-automated methodologies to extract roller parameters from terrestrial lidar points. The procedure was divided into two steps. First, the three-dimensional points were converted to a two-dimensional image to detect the extents of the rollers using fast Fourier transform image matching. Lidar points for every roller were iteratively fitted to a circle. The radius and center of the fitted circle were considered as the average radius and average rotation axis of the roller, respectively. These parameters were also extracted manually and were compared to the measured parameters for accuracy analysis. The proposed methodology was able to extract roller parameters at millimeter level. Erroneously identified rollers were identified by moving average filters. In the second step, roller parameters were determined using the filtered roller points. Two data sets were used to validate the proposed methodologies. In the first data set, 366 out of 372 rollers (97.3%) were identified and modeled. The second, smaller data set consisted of 18 rollers which were identified and modelled accurately.

Introduction

Hot-rolling steel mills are large steel processing facilities. Figure 1 shows a schematic diagram of a steel sheet manufacturing hot-rolling mill. The steel-manufacturing process starts with a cold slab at one end that is heated in a furnace. The hot slab is passed through multiple mills to achieve the desired cross-section. The length over which a slab is processed in a steel mill can extend from six to nine hundred meters. Rollers are placed at regular intervals to transport the slab. Finally, the processed steel sheet is rolled to form a coil.

Figure 2 shows rollers in a hot-rolling steel mill. The rollers are driven by drive motors which are attached to one end of the rollers. The drive motors spin the rollers at a constant rotational speed.

Sagar S. Deshpande is with Penn State University, Wilkes-Barre, PA 16801 (sagard79@gmail.com).

Mike Falk and Nathan Plooster are with Falk-PLI, Portage, IN 46383.

Contributed by Rongjun Qin, February 4, 2021 (sent for review March 18, 2021; reviewed by Chengyi Wang, Juntao Yang).

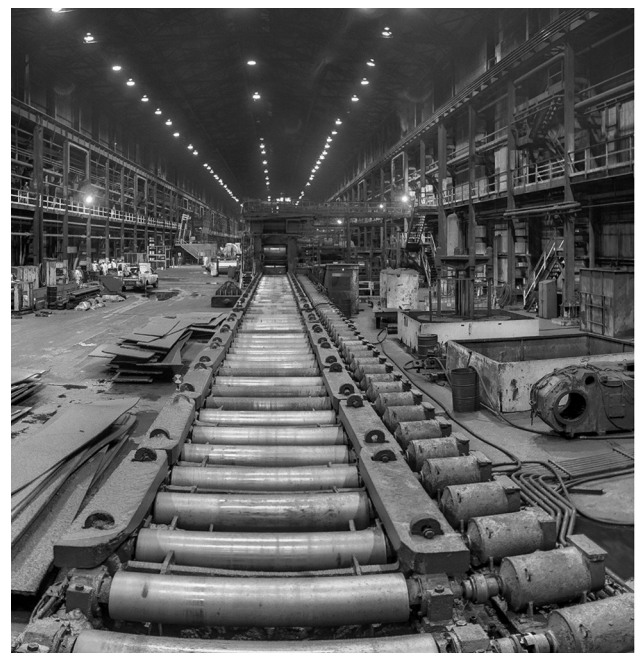


Figure 2. Rollers in a steel mill. Drive motors are on the right side of the rollers.

Over a period, the rollers undergo wear and tear because of friction with the steel. They could develop several issues such as uneven surface profile, tapering of surface, and/or tilt in the rotation axis. Figure 3 shows different defects that can develop. Figure 3a shows the tilt in a roller that may not be perfectly horizontal. Such a roller, due to varying friction over its length, could result in different roller radii. Figure 3b shows a roller with changing radii along its length. The unevenness or tilt in the roller's surface, although a few millimeters, can affect the quality of the steel. Different radii of rollers result in different surface velocities, which results in uneven steel surface.

Photogrammetric Engineering & Remote Sensing
Vol. 87, No. 12, December 2021, pp. 879–890.
0099-1112/21/879–890

© 2021 American Society for Photogrammetry
and Remote Sensing
doi: 10.14358/PERS.21-00005R2

Figure 4 shows changes in diameters from roller to roller. As stated earlier, the rollers are rotated at a constant rate. Uneven radii along the length of the rollers would result in uneven surface velocities causing friction and/or drag between the rollers and steel. Figure 4 also shows that the change in the radii of the rollers over their length could result in an uneven top surface. This situation is shown by the third roller, where a steel section could be supported by the second and fourth rollers. The third roller might just touch or scratch the steel over it.

Thus, it can be concluded that the quality of the steel produced directly depends on the surface quality of these rollers. Until now, the surface variations and alignments of the rollers have been measured manually using tactile direct measurement tools. Pi tapes are typically used to measure the radii of the rollers. The mill operations had to be stopped to make manual measurements, thereby causing loss of revenue for the steel factory. Moreover, such measurements can be made at limited locations. Hence, more time and effort would be required to manually measure the entire profile of the rollers.

Alternatively, a laser scanner can be used to scan the rollers. But manual extraction of the important roller parameters from the laser points would be highly time-consuming and would be influenced by individual operator judgment, which could lead to errors from misinterpretation. Hence, methods that can automatically extract the roller features and minimize manual interaction can greatly increase the effectiveness of roller mapping.

In this paper, methods are presented to extract the roller parameters from terrestrial laser points. The main objectives are to minimize human factor error, increase the measurement level of confidence, and to make the process computationally efficient.

This paper consists of six sections. The second section describes existing methodologies pertinent to the current study. The third section describes the data sets used to test the presented methodologies. The fourth section describes the methodology in detail. The fifth section provides the findings of the proposed methodologies and provides discussions. Finally, the sixth section summarizes the study and their shortcomings. This section also lists topics for future investigations.

Literature Review

Laser (light detection and ranging (lidar)) scanners are increasingly being used on aerial, terrestrial, and mobile platforms. The basic principle of a laser scanner is based on distance measurement using laser pulses sent by a sensor to the object (Liu *et al.* 2009). An onboard global positioning system (GPS)/inertial measurement unit (IMU) system coupled with the range distance can determine the position of the ground point. Due to its direct ranging capabilities and few limitations, lidar is increasingly being used in numerous industries with applications such as structural shape modeling (Puente *et al.* 2016; Yi *et al.* 2019), geometric deformation modeling (Cabaleiro *et al.* 2015; Selvaraj and Madhavan 2018), deformation determination in structural members

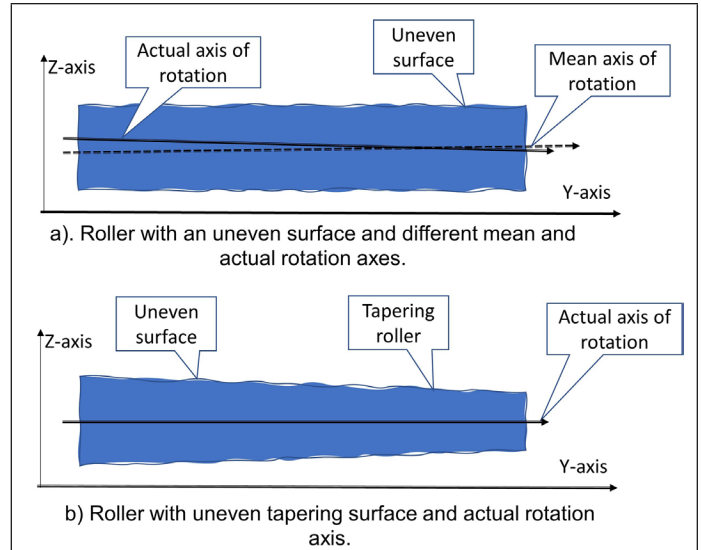


Figure 3. Cross-sectional view of rollers showing surface erosion, mean, and tilted rotational axes.

(Cabaleiro *et al.* 2014), transportation engineering (Gézero and Antunes 2019), and water resources engineering (Deshpande 2013; Deshpande and Yilmaz 2017). Taheri Andani *et al.* (2018) showed the reliability of lidar sensors for the assessment of the top of rail lubricity in a laboratory environment. Stein *et al.* (2016) presented methods to determine infrastructure elements like rails and turnout from mobile lidar data of a railroad. Cabaleiro *et al.* (2016) presented an application of lidar technology in structural health monitoring, especially in the study of deformations and stresses in beams. Gézero and Antunes (2019) extracted three-dimensional (3D) linear elements from a mobile lidar point cloud of a railroad. Deshpande (2021), Sánchez-Rodríguez *et al.* (2019), Yi *et al.* (2019), and Puente *et al.* (2016) presented methodologies addressing different issues in automatic tunnel modeling. Based on the literature review, it can be concluded that several researchers have presented method to model standard steel sections or prismatic sections of tunnels and bridge cross-sections. It could be reliably stated based on the literature review that lidar is progressively used for modeling and mapping various construction elements. Bridges, rails, and girders are currently being modeled using laser scanners. However, the use of laser scanners in steel industries is relatively new. Steel mills have numerous structural elements that need periodic monitoring for the smooth functioning of their facilities and the safety of their employees. Falk *et al.* (2021) has presented methodology to model rails and gantry crane girders by modeling a laser point cloud.

Rollers, one of the important elements in the steel-mill industry, are cylindrical in shape. Commercially available software and existing methodologies cannot address the issues to

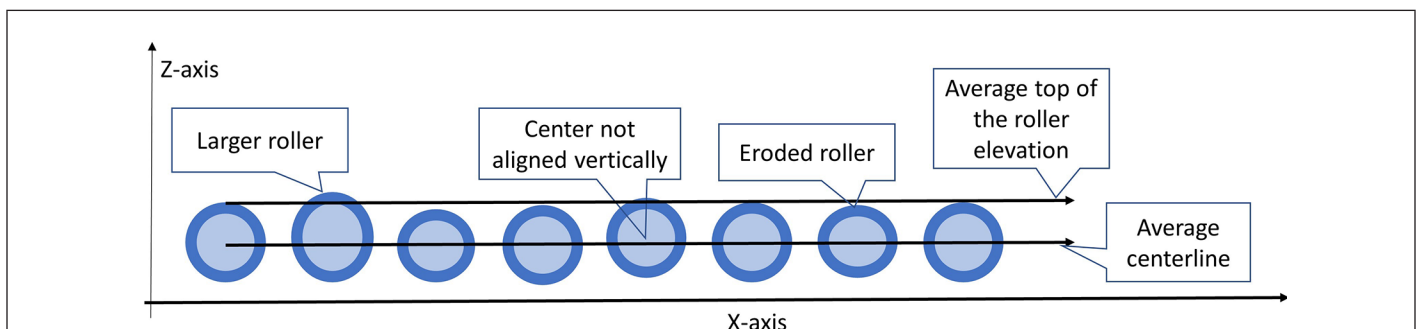


Figure 4. Issues in multiple rollers due to uneven erosion.

the extent necessary in steel mills. Thus, this paper presents roller modeling approaches using a terrestrial laser scanner in steel mills. The methodologies are developed to measure the following roller properties.

2. The actual (tilted) rotation axis variation compared to the mean rotation axis.
3. Surface variations considering the roller's actual (tilted) rotation axis.

Salient Metric Properties of a Roller in a Steel Mill

As stated earlier, the rollers are an essential component in steel mills. In this section, different issues that are addressed by this paper are described in detail. Considering all rollers together (Figure 4) the following pertinent parameters were determined:

1. Centerline variations of rollers (axial 3D alignment).
2. Radius variations of the rollers (roller profile/wear).
3. High point elevations of rollers.

Pertinent parameters considering an individual roller (Figure 3) include:

1. Surface variations of a roller with reference to the mean rotation axis.

Data Description

Two data sets were used to validate the methodologies presented in this paper. These data sets were acquired in a steel mill located in the U.S. using a Z+F IMAGER® 5010C, 3D laser scanner. The rollers were scanned by stationing the instrument on bridges as shown in Figure 2. The first data set consists of lidar points on 372 rollers and the second data set consisted of 15 rollers. The second data set was smaller in extent due to data availability. The nominal roller diameters in the first and second data sets were 0.2 and 0.15 m, respectively. The points were clipped by defining a bounding box. It can be noted from Figure 5 that several outliers existed in the clipped data set. A right-handed local coordinate system was used to orient the data in which the X-axis was along the centerline of the rollers and the Z-axis was in the plumb direction.

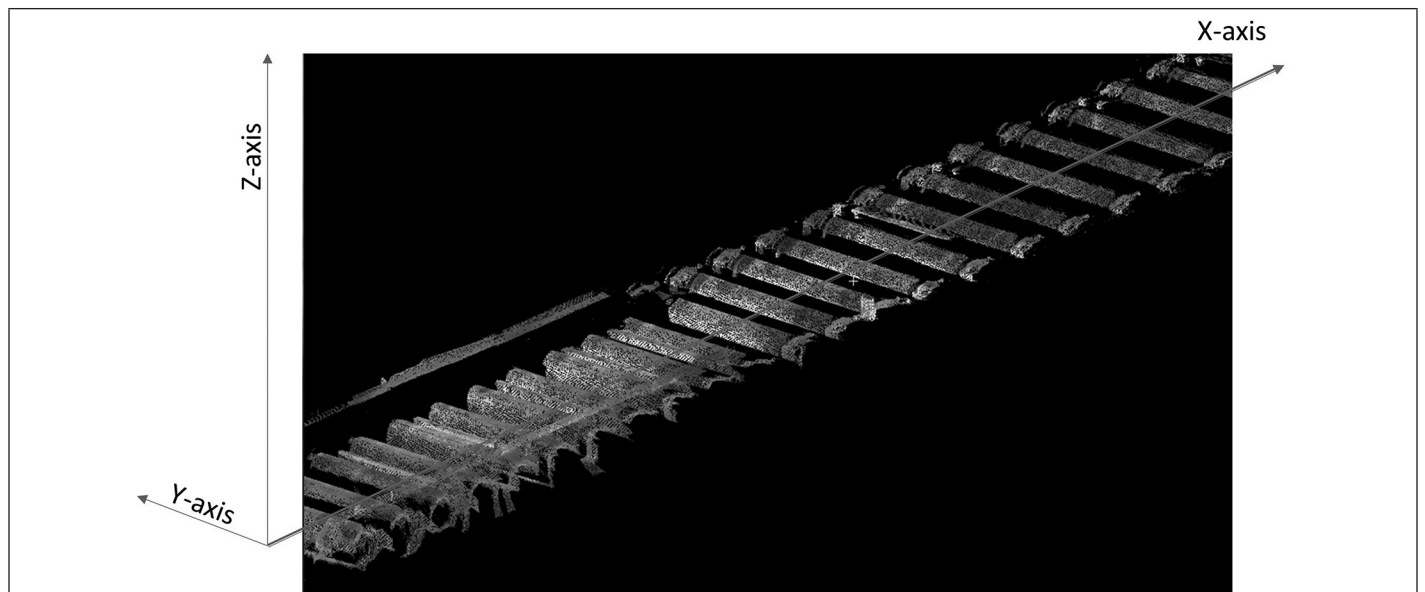


Figure 5. Point cloud of the rollers in a steel mill and the coordinate reference frame.

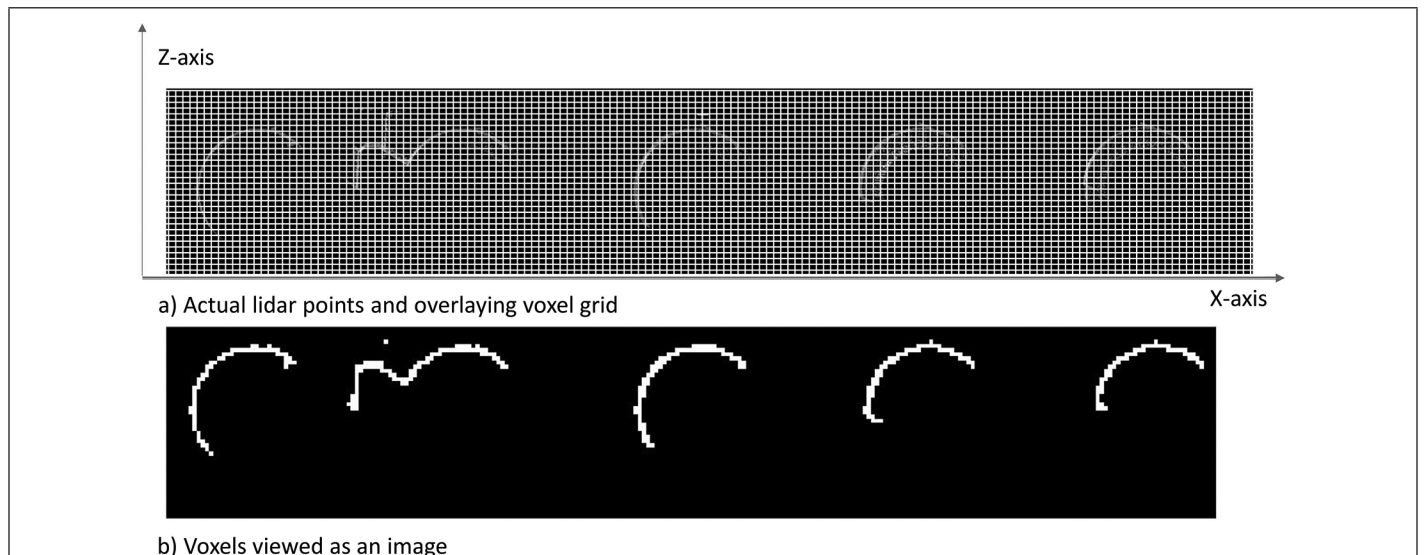


Figure 6. Laser points in the X-Z plane. (a) Voxel overlaid on the point cloud (grid not to scale) and (b) voxels viewed as an image. The image is created by thresholding the number of laser points within each voxel.

Figure 6a shows the roller points and the outlier points on a subset of five rollers. It can be noted that depending on the locations of the scanners and their scan angles, laser points were collected on limited surfaces of rollers.

Methodology

The overview of the entire process is shown in Figure 7. The entire methodology can be broadly grouped as locating the rollers using two-dimensional (2D) fast Fourier transform (FFT) and extracting the rollers' metric parameters.

Two-Dimensional Fast Fourier

Transform (2D FFT) Image Matching

In this section, 2D FFT image matching is explained. The function of 2D discrete Fourier transform (DFT) is shown in Equation 1. The general idea of 2D DFT is that an image in the spatial domain $f(x,y)$ of size $(M \times N)$ pixels will be represented in the frequency domain $F(u,v)$ (Smith 1997; Gonzalez *et al.* 2004) using Equation 1.

$$F(u,v) = \frac{1}{MN} \sum_{x=0}^{M-1} \sum_{y=0}^{N-1} f(x,y) e^{-j2\pi \left(\frac{ux}{M} + \frac{vy}{N} \right)} \quad (1)$$

Figure 8 shows a digital image in the spatial and the frequency domains, respectively. The concept behind the Fourier transform is that any waveform can be constructed using a sum of sine and cosine waves of different frequencies.

$$f(x,y) = \frac{1}{MN} \sum_{u=0}^{M-1} \sum_{v=0}^{N-1} F(u,v) e^{j2\pi \left(\frac{ux}{M} + \frac{vy}{N} \right)} \quad (2)$$

Thus, $F(u,v)$ can be converted to the corresponding image ($f(x,y)$) using the inverse Fourier transform (IFT). FFT is a smart algorithm for rapidly calculating the DFT. FFT can perform convolution by multiplication in the frequency domain hundreds of times faster than convolution in a spatial domain. Using this concept, two images can be convolved in the frequency domain for image matching (Smith 1997). This method was adopted because it is faster than the correlation in the spatial domain.

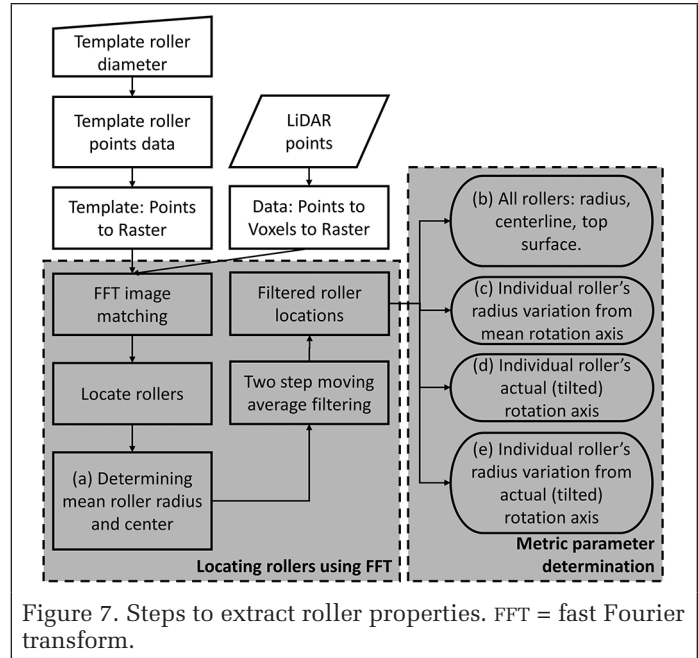


Figure 7. Steps to extract roller properties. FFT = fast Fourier transform.

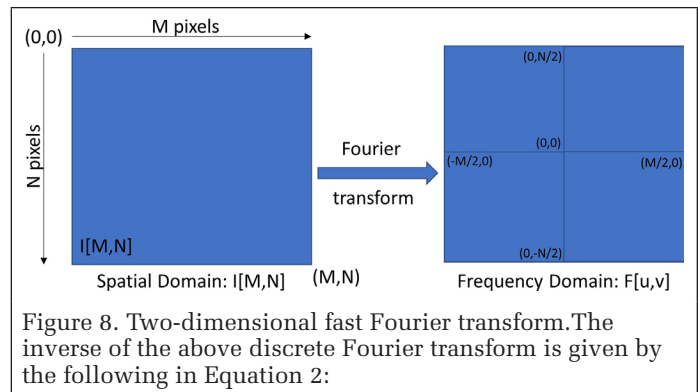
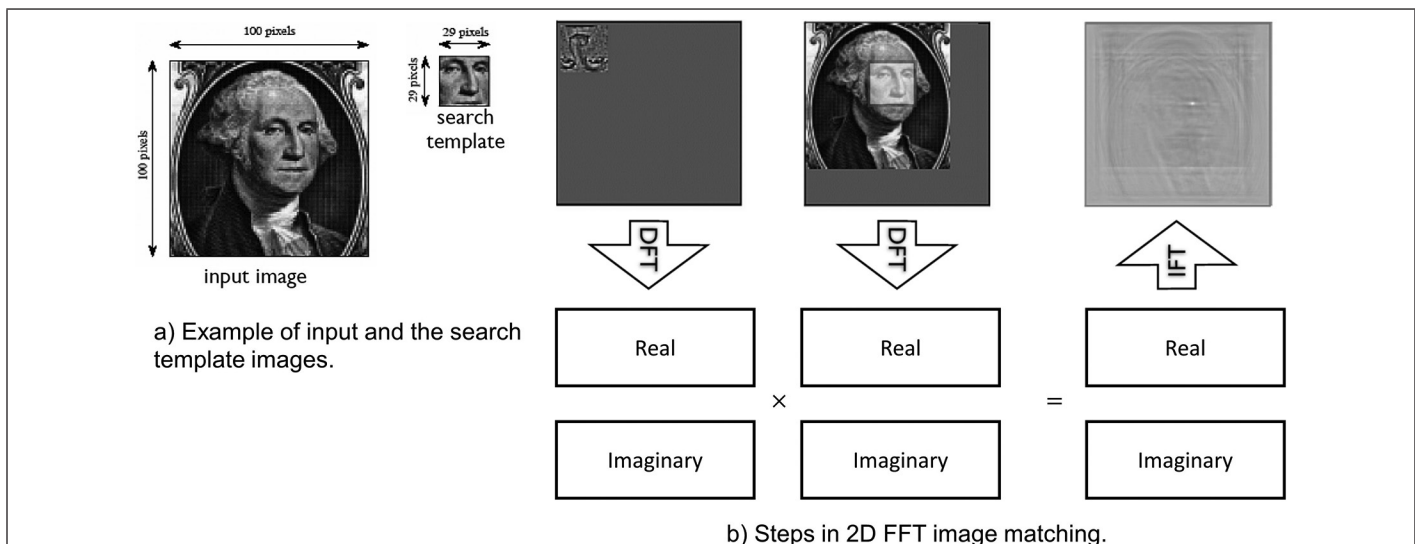


Figure 8. Two-dimensional fast Fourier transform. The inverse of the above discrete Fourier transform is given by the following in Equation 2:

Figure 9a shows a search template that is to be located on the input image. According to the FFT matching, the template image is flipped from left to right and then from top to bottom. A DFT is applied to both the images to obtain the real and imaginary output. These two sets are multiplied to obtain a



b) Steps in 2D FFT image matching.

Figure 9. Fast Fourier transform image matching (Smith 1997). 2D FFT = two-dimensional fast Fourier transform; DFT = discrete Fourier transform; IFT = inverse Fourier transform.

real and imaginary output. An IFT transform is implemented to obtain the correlation. The rightmost image in Figure 9b shows the results, where the brighter pixels represent the locations of higher correlation. This technique is used to locate the rollers to expedite the matching process.

Locating the Rollers Using FFT Matching

Figure 5 shows the point cloud and the coordinate reference frame. To locate the rollers, the entire laser point cloud was converted to voxels. Voxels are 3D cubes represented by width, depth, and height in X, Y, and Z directions, respectively. Several researchers have used voxels in various lidar-based applications (Popescu *et al.* 2008; Chasmer *et al.* 2004).

In this study, rectangular prism-shaped voxels of dimensions 15.24 mm (0.05 ft) × 15.24 mm in the X and Z directions and extending over the entire width in the Y-direction were created. It can be noted from Figure 6a that the voxels would represent a 2D image in which the column and row directions were aligned to the X and Z axes of the data, respectively. The first column of the raster image was placed on the point with the smallest X-value and the first row was placed on the point with the highest Z value. Voxels containing at least forty points were considered valid. This threshold was based on experimental testing which showed a reduction in outlier cells in the raster image. A binary image was created along the X and Z axis containing 1 for a valid voxel and 0 for a nonvalid voxel. Figure 6b shows the resulting image where white shows the valid pixel containing at least forty points. The shape of the roller and several outlier pixels can be seen in this figure. In the next step, individual rollers were located using the FFT image matching technique where Figure 6b was used as the input image.

In a steel mill, a standard roller size is used. Therefore, depending on the data set, a template roller was created by specifying the nominal roller radius. Virtual points were placed at the specified radius (Figure 10a) and were grouped in voxels of size 15.24 mm (0.05 ft) × 15.24 mm in the X and Z directions. The voxels were converted to create a template search image as shown in Figure 10b.

This template image was used for FFT image matching to locate the rollers in the input image. The resulting correlation image is shown in Figure 11a. It should be noted that the template was a complete circle whereas the rollers were partial circles with varying surface point coverage. Depending on the extent of roller surface points, the correlation value ranged significantly over the entire length. However, as seen in Figure 6a, the extents of the rollers' surface scan changed gradually in a smaller region. Hence, to obtain a uniform correlation, the entire length was divided into smaller sections along the X-direction so that a local threshold could be determined. Approximately five rollers were processed at one time, thereby generating a uniform correlation value for every section. Sufficient overlap was maintained between these sections to avoid missing any roller at their ends. Based on multiple testing a threshold of $\text{Max_value}/2$ was adopted for each section to locate the rollers. Here Max_value represents the maximum correlation value within each section. Figure 11b shows a binary image where white pixels represent locations with values greater than $\text{Max_value}/2$. It can be noticed that a cluster of white pixels exist at the roller locations. At this point, user input was used to specify a seed point, as shown in Figure 11b. Rollers were searched within a buffer of three pixels on both sides along the row of the seed pixel. When a cluster was detected, their average location in row and column directions were considered as a matching location. It should be noted that FFT matching located the lower right corner of the rollers. Using this location, the left and right extents in the X-direction and top and bottom in the Z-direction for every roller on the image were identified as below:

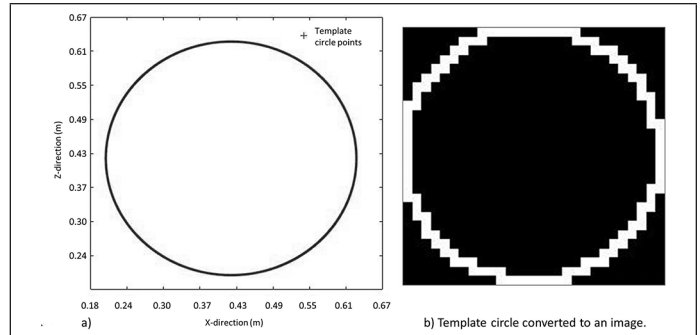


Figure 10. Template roller. (a) Points placed at a standard roller radius and (b) image of the template.

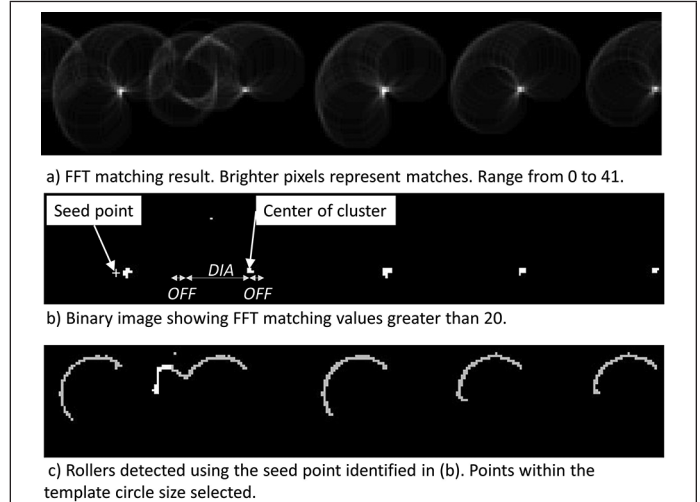


Figure 11. Fast Fourier transform (FFT) matching between the template and the data image. DIA = diameter of the template circle; OFF = four pixels offset.

- Left extent = Center column pixel – size of template circle (DIA) – 4 pixels (OFF)
- Right extent = Center column pixel + 4 pixels (OFF)
- Top extent = Center row pixel – size of template circle (DIA) – 4 pixels (OFF)
- Bottom extent = Center row pixel + 4 pixels (OFF)

These measurements are shown in Figure 11b where DIA stands for the diameter of the template circle and OFF stands for four pixels offset. The offset pixels accounted for the rollers' size variations. Figure 11c shows the extents of the identified rollers. Laser points on every roller were identified using the extents determined. At this stage, the locations of every roller were available. Using the points within these extents, various parameters were extracted as described below.

Determining the Mean Radius and Mean Rotation Axis of an Individual Roller

The points within the extents of a roller consisted of outliers and roller points. Therefore, it was necessary to exclude the outliers to determine the average radius and center of the roller. An iterative refinement approach was implemented to determine the actual radius and the center of the roller, as shown in Figure 12. A threshold of 6.1 mm (0.02 ft – 1/8th of an inch) was used after several tests to shortlist the points belonging to the roller. Points within this threshold were used to fit a circle, compute the radius, and coordinates of the center of the fitted circle.

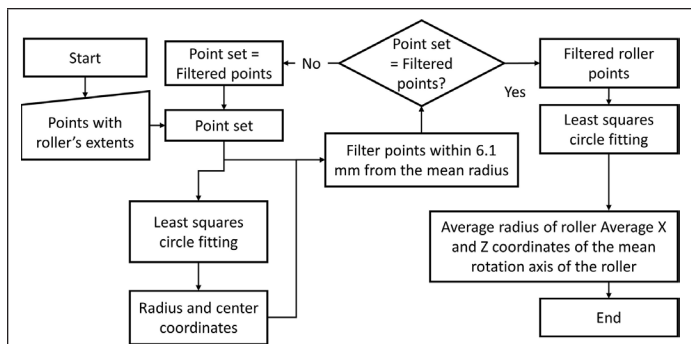


Figure 12. Flowchart to determine a roller's points, average diameter, and the location of the mean rotation axis.

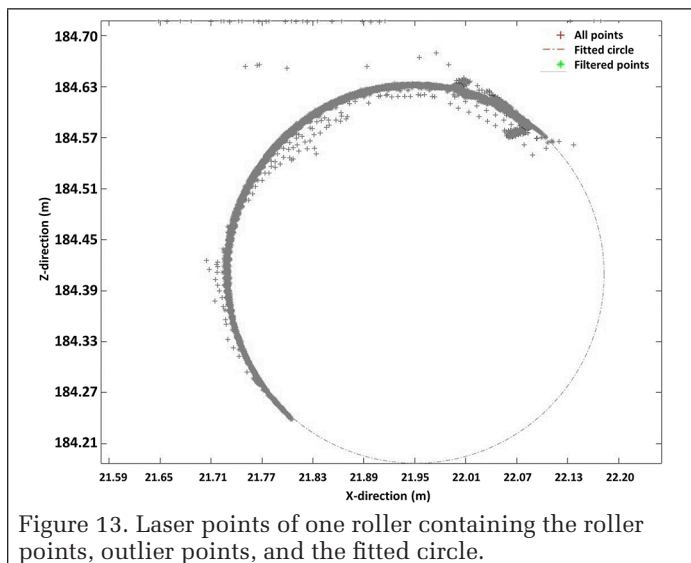


Figure 13. Laser points of one roller containing the roller points, outlier points, and the fitted circle.

Figure 13 shows laser points within the extents of one roller containing the filtered roller points, outlier points, and the fitted circle. The coordinates of the center were considered the mean axis of rotation for the roller.

It was found that the above methodology erroneously selected a few incorrect roller locations. Based on visual examination, it was found that the erroneously detected rollers had significantly different radii and centers' Z-coordinate. Thus, a two-stage filtering process was developed that examined the consistency in the radii and the centers of all the rollers to determine erroneously detected rollers. In the first stage, a moving average roller radius and Z-coordinate at each roller was calculated using the neighboring roller parameters. The

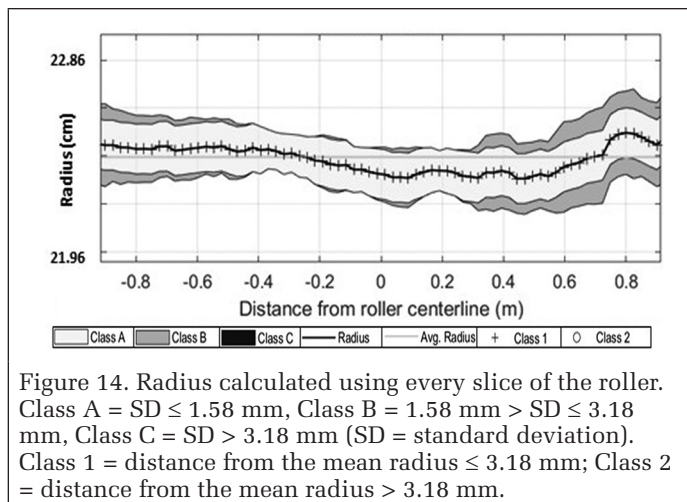


Figure 14. Radius calculated using every slice of the roller. Class A = $SD \leq 1.58$ mm, Class B = $1.58 \text{ mm} > SD \leq 3.18$ mm, Class C = $SD > 3.18$ mm (SD = standard deviation). Class 1 = distance from the mean radius ≤ 3.18 mm; Class 2 = distance from the mean radius > 3.18 mm.

differences between the computed and the average values were calculated and rollers outside certain confidence from the mean separation were considered as outliers. By implementing the above process, erroneously detected rollers were excluded from further analysis. For each roller, its mean radius was added to the Z-coordinate of the roller's centers to determine the top elevation of the rollers' surface. In the second filtering stage, moving average filtering was implemented on the top elevation of the roller's surface to filter outliers. The analysis was performed using different moving average filter sizes and different confidences.

Determination of the Individual Roller's Radius Variation from the Mean Rotation Axis

The steel slabs are primarily supported and transported over the middle length of the roller. Determining the radii variations over the length of the roller could provide essential information about its wear and tear. Therefore, radii variations of every roller with reference to the mean rotation axis were calculated at regular intervals to determine surface undulations. The roller points from the previous section were sliced in the Y-direction at every 25.4 mm (1 inch). A mean radius and its standard deviation were calculated with reference to the mean rotation axis for every slice of data. Figure 14 shows the radii variations and their standard deviations at each slice of the roller.

Determination of Individual Roller's Actual (Tilted) Rotation Axis

As described earlier, the rollers were susceptible to tilt. Tilt results in uneven wear and surface velocities. In this study, the roller's tilt was modeled by computing the radii at the ends of the roller, as shown in Figure 15.

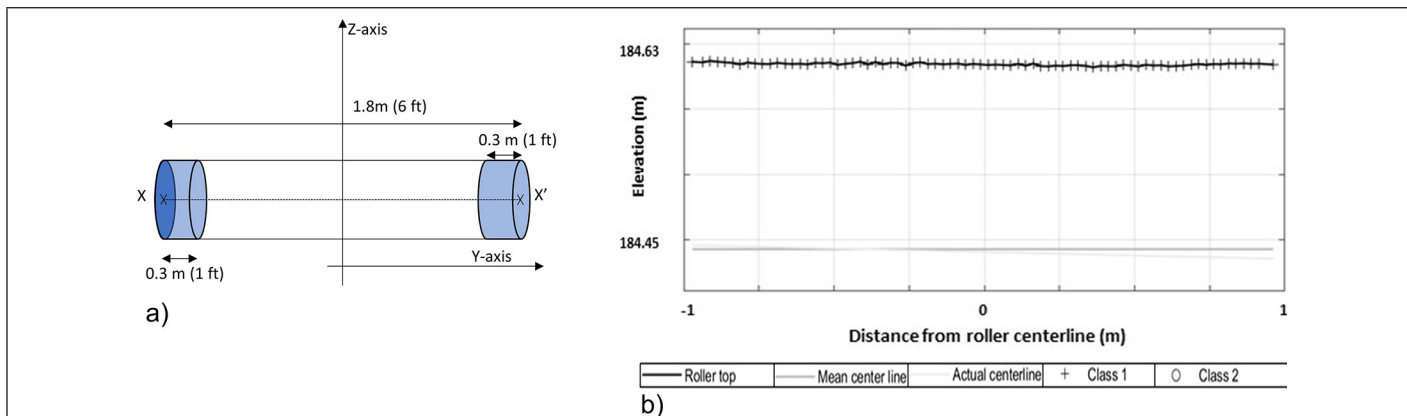


Figure 15. Roller tilt determination. (a) Schematic diagram of the roller tilt axis and (b) mean and actual roller axis and the surface points. Class 1 = distance from the mean radius ≤ 3.18 mm; Class 2 = distance from the mean radius > 3.18 mm.

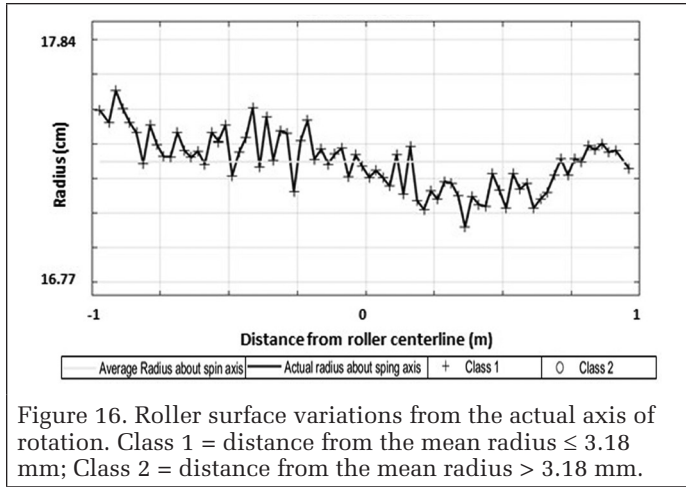


Figure 16. Roller surface variations from the actual axis of rotation. Class 1 = distance from the mean radius ≤ 3.18 mm; Class 2 = distance from the mean radius > 3.18 mm.

Roller points within 0.3 m (1 ft) at both the ends of the roller were shortlisted to determine best-fit circles. The calculated radii and centers of these circles were assumed to be at the ends of the roller. The actual (tilted) rotation axis was created by connecting the centers at both ends of the roller. A positive tilt value represented that X location was higher than X.

Determination of the Individual Roller's Radius Variation from the Actual (Tilted) Rotation Axis

In this section, the roller surface variations with reference to the actual axis of rotation were determined. Roller points were divided into slices of 25.4 m width along its length to calculate the radii from the actual axis of rotation.

Results and Discussion

The above-presented methodologies were implemented on two data sets to validate the proposed methodologies. The first data set contained 372 rollers extending to a length of 350 m and the second data set consisted of 15 rollers extending to a length of seven meters. The second data set was smaller due to limited data availability. The rollers were of different sizes in both the data sets. As it was not possible to include graphical results of all the rollers, salient graphics and tables have been shown to prove the efficacy of the methods. First, the results from the larger data set are presented followed by the second data set.

Data Set 1: Locating Rollers

The first data set covered 372 rollers. The points within a box placed around all the rollers were exported from Cyclone into MATrix LABoratory. These points were converted to voxels of dimensions 15.24 mm (0.05 ft) \times 15.24 mm in the X and Z directions and extending over the entire width in the Y-direction. As explained in the 2D FFT image matching, the input image was created using the voxel data set and the roller template image was created using a standard radius of 20 cm. The entire length of the data was segmented into smaller sections consisting of approximately five rollers. A sufficient overlap was maintained between the sections so that no rollers at the edges were excluded. The rollers' locations identified in each region using the DFT were ordered in ascending X-coordinates and any duplicate locations were eliminated. Extents of each roller were defined from the matched location as explained in Figure 11c to segregate points belonging to each roller. Using the least-squares method, a circle was fitted iteratively to the segregated points to determine the roller's mean radius and mean center coordinates (mean axis of rotation).

Data Set 1: Assessment of Roller Location

Using the 2D FFT, rollers were detected at 393 locations, however, only 372 rollers existed in the data. Data for each roller was manually inspected to identify incorrect rollers. It was found that 366 rollers were correctly identified and modeled (see Figure 17), six rollers were correctly identified but incorrectly modeled (see Figure 18), and the remaining 21 were not roller locations (see Figure 19). Based on this inspection, the FFT matching successfully identified 98.3% (366 out of 372) of rollers (information listed in Table 1).

Figure 20a–c shows the Z-coordinate variations of rollers' center, rollers' radii variations, and the rollers' top surface elevation variations, respectively. Relating to Table 1, the 27 erroneously located or modeled rollers can be visually identified as spikes.

Table 1. Radius, X- and Z-coordinates of incorrectly identified roller. Six locations were rollers. The remaining locations were incorrectly identified. The highlighted outliers were not filtered at 95% confidence using an 11-value moving average filter.

Roller ID	Z-Coordinate (m)	Radius (m)	Roller ID	Z-Coordinate (m)	Radius (m)
20	184.387	0.259	252	184.524	0.175
153	184.519	0.133	297	184.323	0.175
154	184.519	0.127	298	184.512	0.156
156	184.094	0.566	299	184.494	0.171
157	184.796	0.207	300	184.471	0.186
158	184.430	0.226	301	184.511	0.183
203	184.593	0.090	302	184.471	0.188
204	184.530	0.064	303	184.399	0.196
225	184.476	0.153	304	184.436	0.204
229	184.479	0.234	305	184.453	0.217
242	184.438	0.099	389	184.578	0.094
243	184.444	0.082	392	184.388	0.237
244	184.590	0.141	393	184.359	0.106
249	184.467	0.207			

ID = identification.

Data Set 1: Filtering the Data

The erroneously located rollers were filtered in two steps. In the first step, the roller radii and Z-values were filtered using a moving average filter. Tests were conducted using two moving average filters to identify the outliers. The first moving filter used five locations (two on both sides and the location itself) and the second used 11 locations (five on both sides and the location itself) to compute the average values. Moving average values at the start and end of the line used fewer points. Figure 20a and 20b shows the moving averages of the radii and Z-values. The differences between the moving average and the calculated value at each roller were determined and points outside 68.8%, 80%, 90%, and 95% confidences about their mean differences were considered invalid. In the second step, the top elevations of every roller were computed by adding the roller radius to the center's Z-value. Once again, moving average values were computed and outliers were determined based on 68.8%, 80%, 90%, and 95% confidences. The efficacy of the above two steps filtering process was verified by visual inspection. Table 2 summarizes the results. It can be noticed that by decreasing the confidence about the mean, a greater number of incorrect rollers were detected, but more correct rollers were also falsely flagged as outliers. Similarly, an increase in the size of the moving average filter showed better results. At 95% confidence using an 11-size moving average filter, 18-locations out of 27-locations were detected

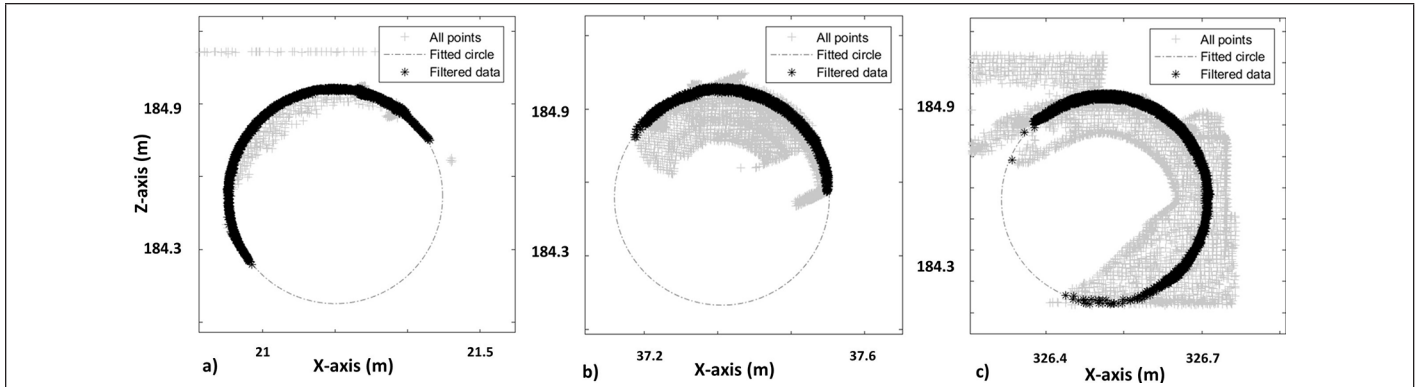


Figure 17. Sample locations with positive discrete Fourier transform matching and roller detection. Several outlier points can be seen that were filtered.

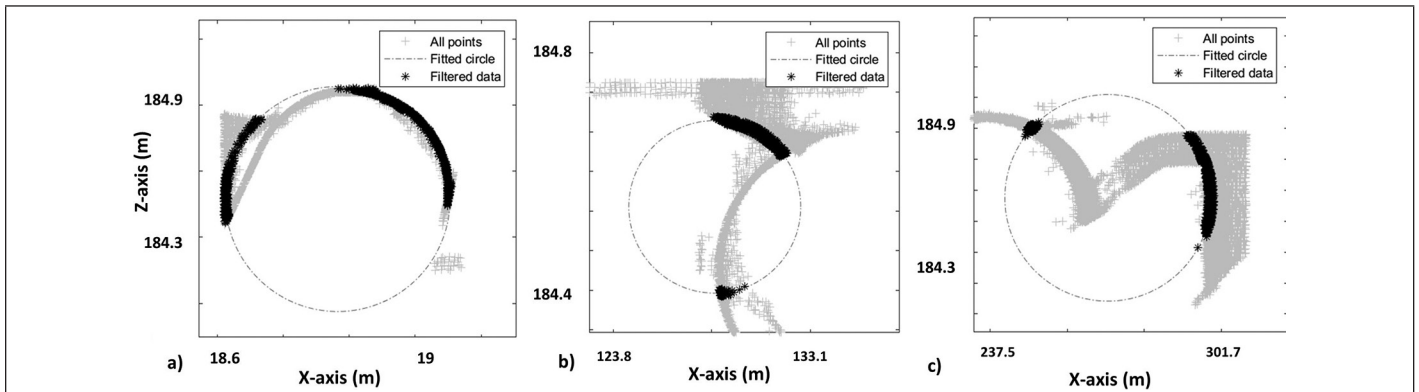


Figure 18. Sample locations where correct roller locations were identified but incorrect parameters were computed. (a) Outlier points on the left side of the roller. This resulted in a larger diameter radius and lower Z-coordinate of the center. See (b) and (c), where part of the roller selected resulted in incorrect parameters.

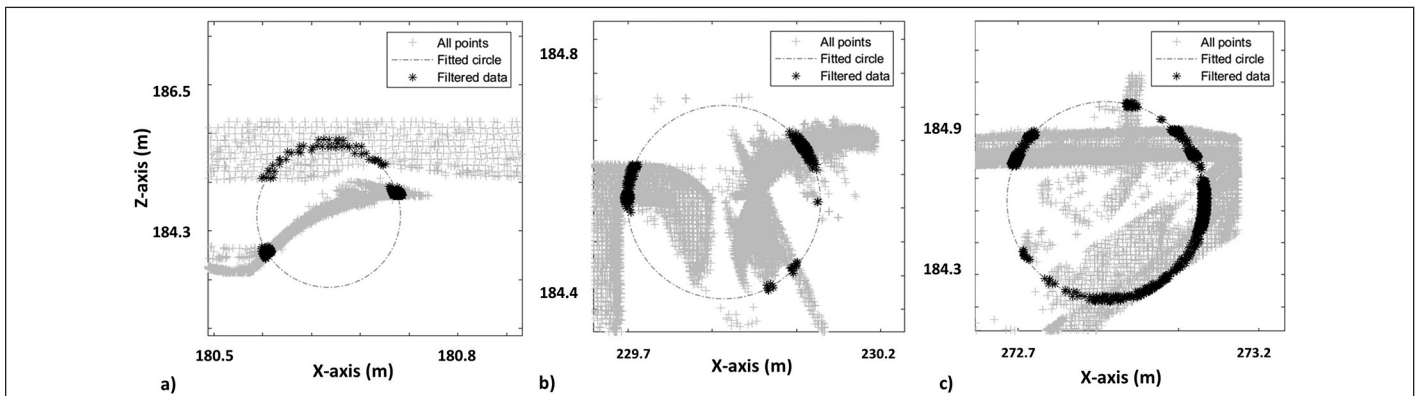
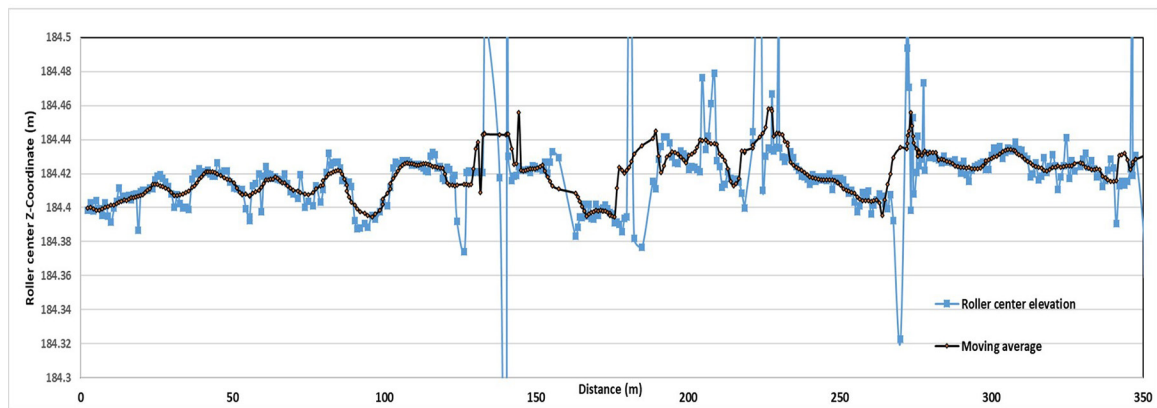


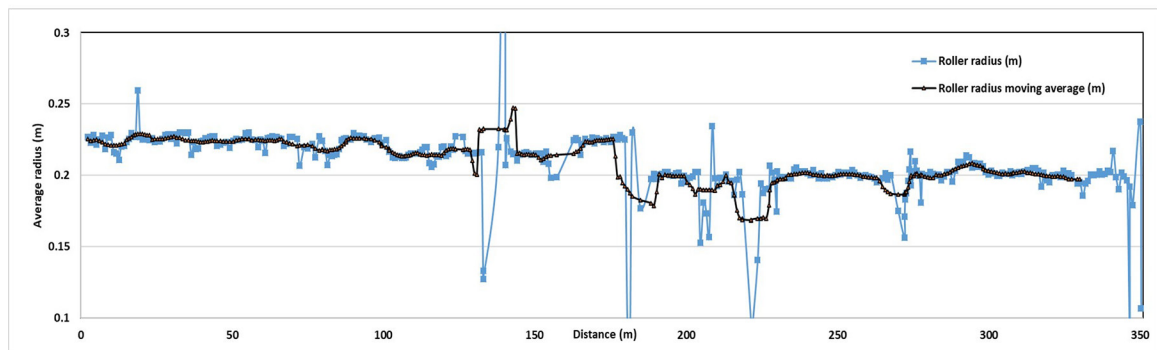
Figure 19. Sample identified locations where rollers were not present.

Table 2. Filtering result at varying confidence intervals.

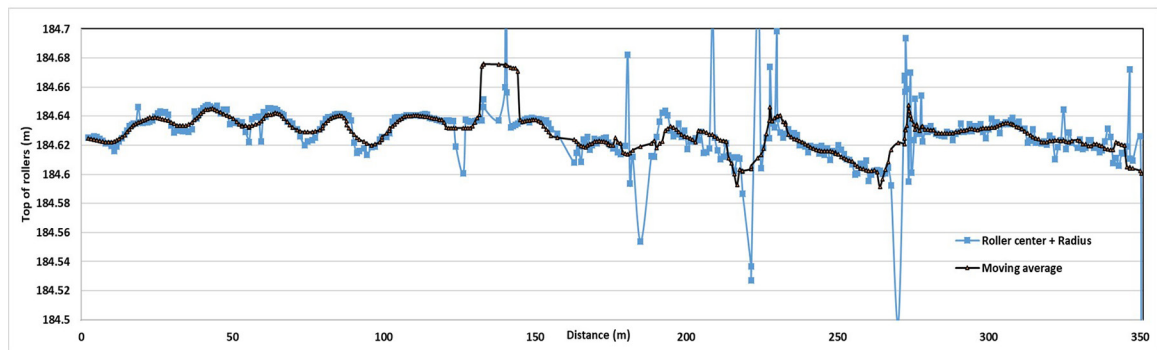
Average Moving Filter Size→	5 Locations				11 Locations			
	Correctly Filtered	Failed to Detect	Falsely Flagged	Success Rate (%)	Correctly Filtered	Failed to Detect	Falsely Flagged	Success Rate (%)
Confidence (%)								
68.0	24	3	19	94.0	25	2	19	94.3
80.0	23	4	11	95.9	21	6	13	94.8
90.0	20	7	7	96.2	19	8	3	97.0
95.0	19	8	4	96.3	18	9	1	97.3



a) Elevation variations of rollers' center of all the rollers.



b) Radii variations of all the rollers.



c) Top surface variations of all the rollers.

Figure 20. Plots showing the centerline of all rollers before filtering the erroneously located rollers.

as outliers. Nine locations were not detected, and 1 roller was falsely detected as an outlier. The total success rate was computed as a ratio of failed and incorrect locations to the total rollers in the data. In this case, $(366 - 9 - 1)/366 = 97.3\%$.

Figure 21a and 21b shows the roller centerline and the radii variation plots after filtering. Continuing the roller's data analysis, desired pertinent measurements were also extracted for all the rollers. These results are discussed in the following sections.

Filtered laser points for every roller were uniformly sliced to determine the average roller radii. The center of the circles was the mean rotation axis. Figure 22 illustrates surface variations with the reference to their mean axes of rotation for four sample rollers. The graphs show the areas of significant surface wear.

The actual (tilted) axis for each roller was subsequently determined by determining circles at both ends. A line connecting these circles was considered as the actual rotation axis. Figure 23 shows the mean and the actual axes of rollers' rotation. The Class 1 and Class 2 points are placed at the radii distance from the mean axis of rotation.

Figure 24 shows radii variations of rollers from the actual rotation axis. The radii variation highlights the surface wear for the rollers.

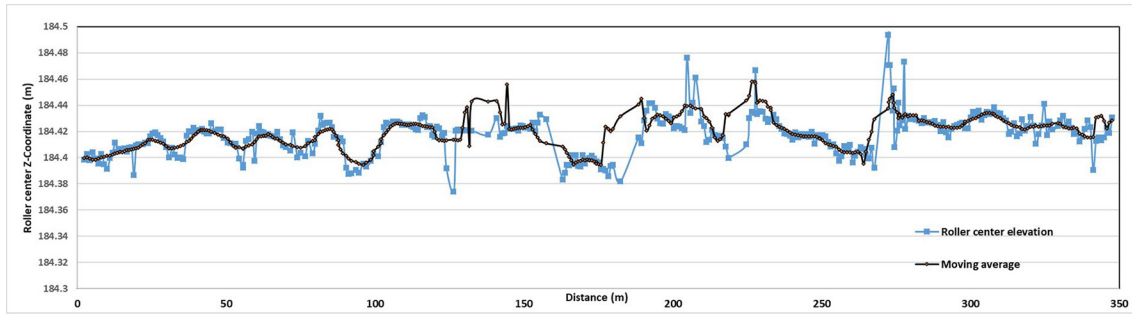
Data Set 2: Locating Rollers

The second data set consisted of 15 rollers of 0.15 m. The procedure explained for data set 1 was implemented on data set 2 by specifying a search radius of 0.15 m. Using FFT, roller points were segregated and using the least-squares method, a circle was fitted iteratively to determine the roller's mean radius and mean center coordinates (mean axis of rotation). All the fifteen rollers were detected. Upon manual inspection it was found that each roller was modelled correctly.

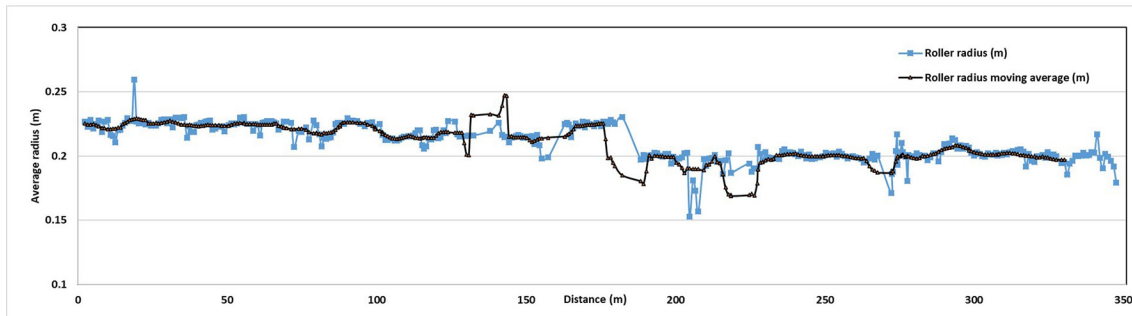
The results obtained for both the data sets were compared to manually extracted parameters as explained in the next section.

Data Set 1 and 2: Accuracy Assessment

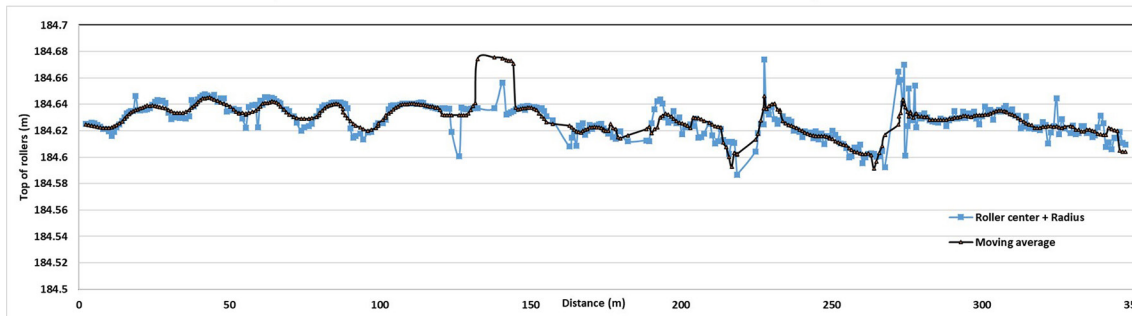
As it was not possible to physically measure the roller parameters due to limited access, the data set was manually processed to extract roller parameters such as the average radius and the elevation of the average axis. The data set was



a) Elevation variations of rollers' center after the two-step filtering.



b) Radii variation after the two-step filtering.



c) Top surface variations after the two-step filtering.

Figure 21. Centerline and radii variation after the two-stage filtering.

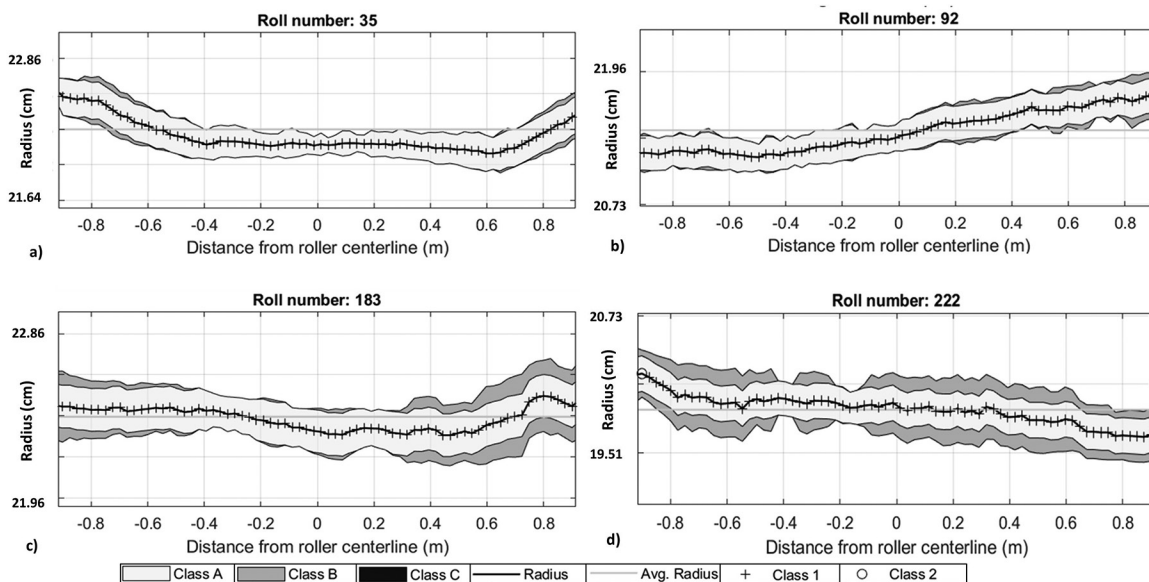


Figure 22. Radii variations of selected roller surfaces. Class A = $SD \leq 1.58$ mm; Class B = 1.58 mm $> SD \leq 3.18$ mm; Class C = $SD > 3.18$ mm (where SD = standard deviation). Class 1 = distance from the mean radius ≤ 3.18 mm; Class 2 = distance from the mean radius > 3.18 mm.

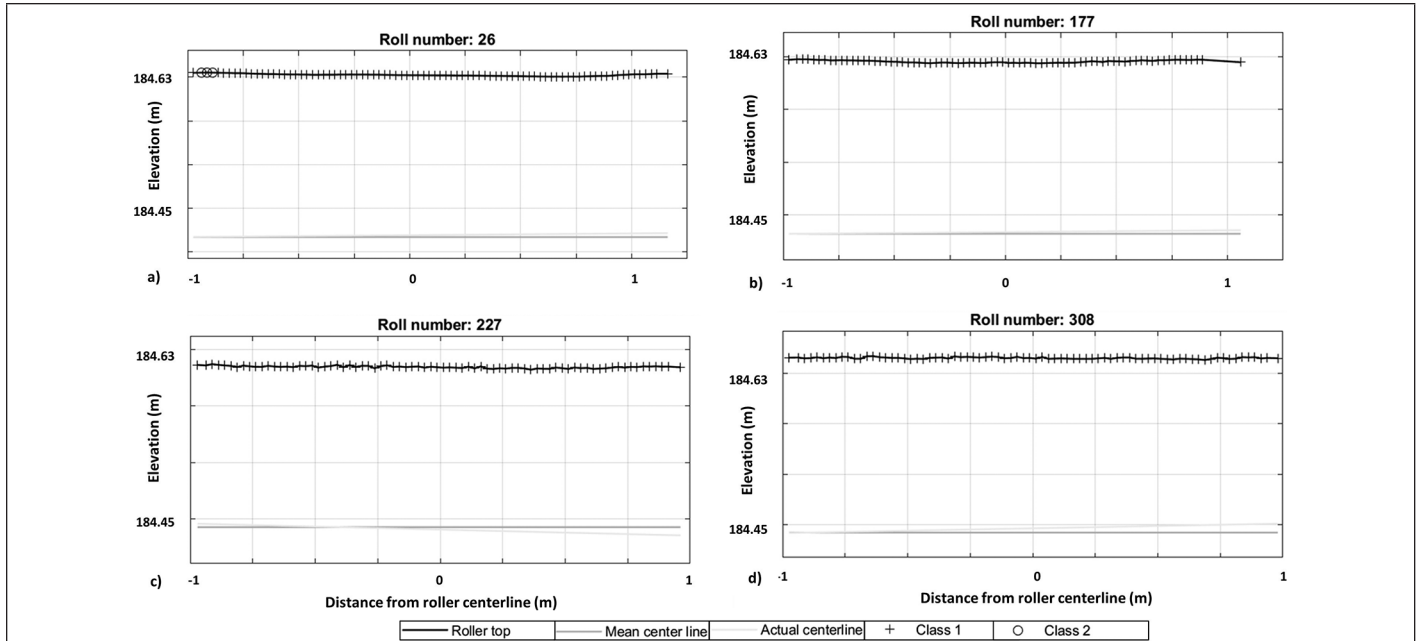


Figure 23. Radii variations with reference to the mean and actual axes of rollers. Class 1 = distance from the mean radius ≤ 3.18 mm; Class 2 = distance from the mean radius > 3.18 mm.

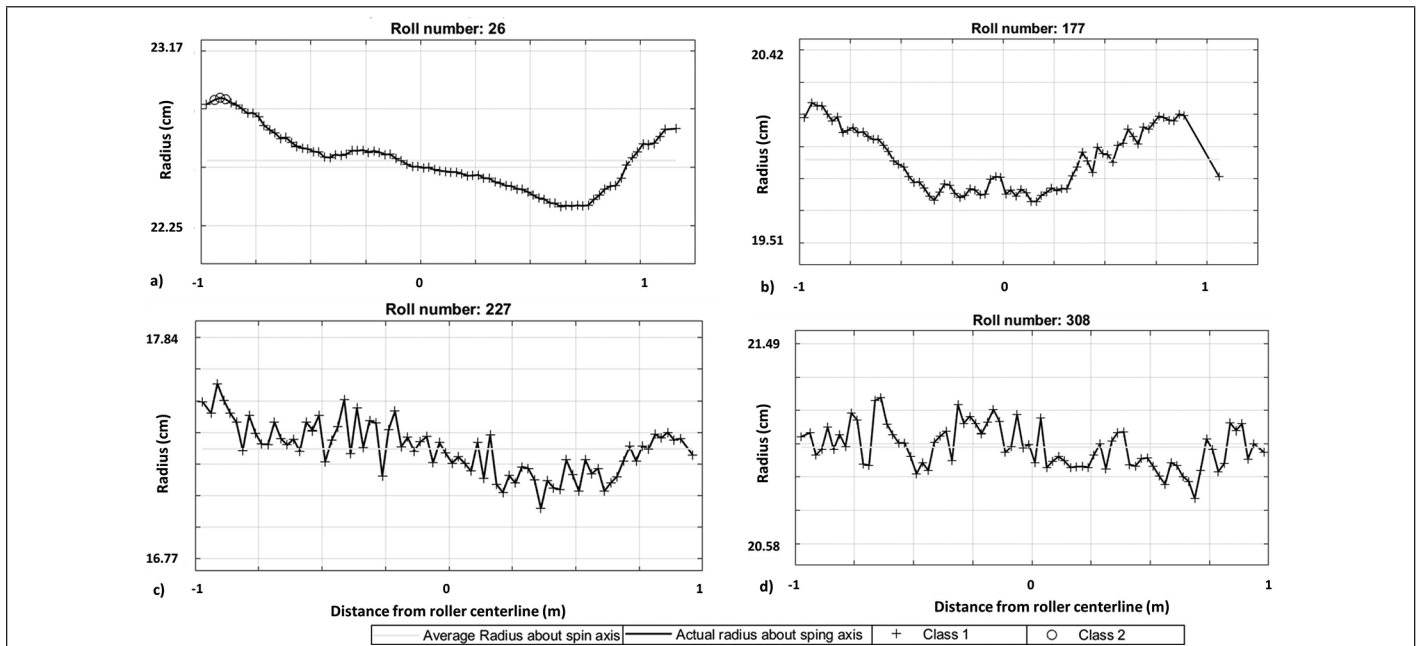


Figure 24. Average radii variations with reference to the actual axis. Class 1 = distance from the mean radius ≤ 3.18 mm; Class 2 = distance from the mean radius > 3.18 mm.

manually segregated for each roller and was modeled using a tool available within Cyclone software. Figure 25a shows the manual selection of roller points and modeling using the available tool in the software and Figure 25b shows the modelled cylindrical shape in the software.

The radius and the elevation of the cylinder were recorded and compared to the finding of the proposed methodology. Table 3 shows the average and standard deviation of both the data sets. The average radii variation was in millimeter level whereas the elevation variation was in centimeter level. It should be noted that the process of manual modeling could also have errors and thus could result in errors shown in Table 3.

Table 3. Average and standard deviation by comparing the computed and measured radii and elevations of rollers for data set 1 and 2.

	Data Set 1		Data Set 2	
	Radius (mm)	Elevation (mm)	Radius (mm)	Elevation (mm)
Mean	4.3	50.0	0.9	26.0
Standard deviation	7.2	10.5	1.0	2.3

Conclusion

Two data sets consisting of different nominal roller radii were analyzed in this study. The first data set consisted of 370

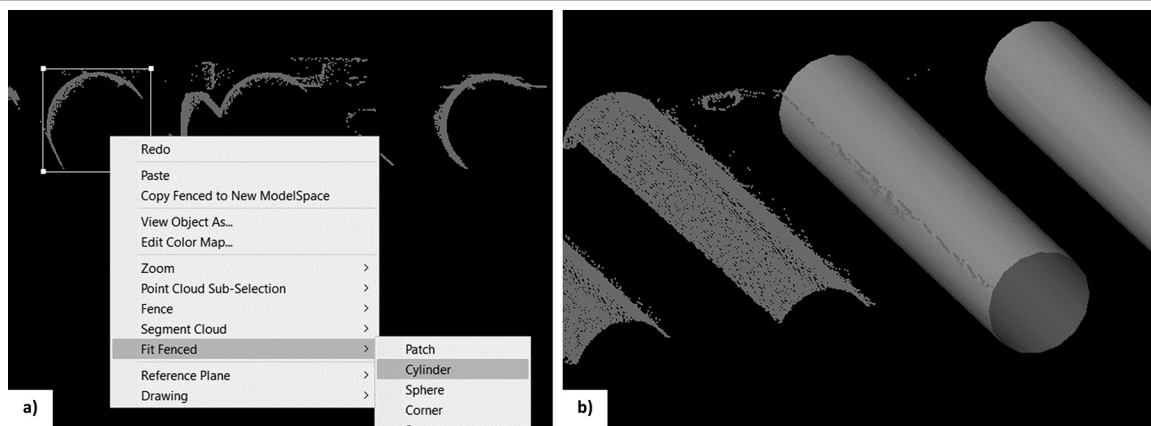


Figure 25. Manual modeling of rollers. (a) Manual extraction of roller points and (b) resulting cylinder using the cylinder tool in Cyclone software.

rollers and the second consisted of 15 rollers. New methodologies were presented to locate and extract roller properties that are important in the steel industry. The primary results were visually inspected to determine the outliers. Two-stage moving average filters were used to identify the outliers for the first data set. The results showed 97.3% success in identifying rollers correctly using an 11-location moving average filter at 95% confidence. A comparison between the manually extracted parameters and the measured parameters revealed that the proposed method was able to achieve millimeter level accuracy. This study also extracted valuable information from the laser points data such as roller's erosion, tilt, and alignment parameters that can be useful to the steel industry to replace rollers. The results showed that the laser scanner can effectively map deformations in rollers.

Limitations and Future Recommendations

The presented methodologies were implemented on data sets that were clipped from a larger data set. Several outliers were present in both the data sets. However, it was noted that excessive outliers could result in incorrect roller modeling. Additionally, it was also observed that the current methodology was sensitive to the nominal search radius used to create the template circle. It was observed that specifying a significantly large or small radius resulted in inaccurate roller identification and modeling.

During this investigation, several avenues were identified for future study, including the use of image data. At present, the entire process is automated with minimum human interpretation. Manual operations were only involved in the clipping of the rollers from the entire steel mill data set, the selection of a seed point, and defining the template roller size. The whole process can be improved to be an entirely automatic procedure, which allows for real-time data processing.

References

Cabaleiro, M., B. Riveiro, P. Arias and J. C. Caamaño. 2015. Algorithm for beam deformation modeling from LiDAR data. *Measurement: Journal of the International Measurement Confederation* 76:20–31. <https://doi.org/10.1016/j.measurement.2015.08.023>.

Cabaleiro, M., B. Riveiro, P. Arias and J. C. Caamaño. 2016. Algorithm for the analysis of deformations and stresses due to torsion in a metal beam from LIDAR data. *Structural Control and Health Monitoring* 23(7):1032–1046.

Cabaleiro, M., B. Riveiro, P. Arias, J. C. Caamaño and J. A. Vilán. 2014. Automatic 3D modelling of metal frame connections from LiDAR data for structural engineering purposes. *ISPRS Journal of Photogrammetry and Remote Sensing* 96:47–56.

Chasmer, L., C. Hopkinson and P. Treitz. 2004. Assessing the three-dimensional frequency distribution of airborne and ground-based lidar data for red pine and mixed deciduous forest plots. *International Archives of Photogrammetry Remote Sensing Spatial Information Science* 36(8):W2.

Deshpande, S. 2021. Tunnel modeling using mobile mapping lidar points. In *Proceedings American Society of Photogrammetry and Remote Sensing*, 29 March–2 April 2021.

Deshpande, S. S. 2013. Improved floodplain delineation method using high density LiDAR data. *Computer Aided Civil and Infrastructure Engineering* 28(1):68–79.

Falk, M., S. Deshpande, D. Zhang and N. Plooster. 2021. Four-dimensional crane rail measurement. U.S. Patent US20210088407A1, filed on 25 March 2021.

Gézero, L. and C. Antunes. 2019. Automated three-dimensional linear elements extraction from mobile LiDAR point clouds in railway environments. *Infrastructures* 4(3):46.

Gonzalez, R. C., R. E. Woods and S. L. Eddins. 2004. *Digital Image Processing Using MATLAB*. New Delhi, India: Pearson Education India.

Liu, J. K., R. Li, S. Deshpande, X. Niu and T. Y. Shih. 2009. Estimation of blufflines using topographic LiDAR data and orthoimages. *Photogrammetric Engineering and Remote Sensing* 75(1):69–79.

Popescu, S. C. and Z. Kaiguang. 2008. A voxel-based lidar method for estimating crown base height for deciduous and pine trees. *Remote Sensing of Environment* 112(3):767–781.

Puente, I., B. Akinci, H. González-Jorge, L. Díaz-Vilariño and P. Arias. 2016. A semi-automated method for extracting vertical clearance and cross sections in tunnels using mobile LiDAR data. *Tunnelling and Underground Space Technology* 59:48–54.

Sánchez-Rodríguez, A., M. Soilán, M. Cabaleiro and P. Arias. 2019. Automated inspection of railway tunnels' power line using LiDAR point clouds. *Remote Sensing* 11(21):2567.

Selvaraj, S. and M. Madhavan. 2018. Geometric imperfection measurements and validations on cold-formed steel channels using 3d noncontact laser scanner. *Journal of Structural Engineering* 144(3):04018010.

Smith, S. W. 1997. *The Scientist and Engineer's Guide to Digital Signal Processing*. San Diego, Calif.: California Technical Publishing, p. 35.

Stein, D., M. Spindler, J. Kuper and M. Lauer. 2016. Rail detection using lidar sensors. *International Journal of Sustainable Development and Planning* 11(1):65–78.

Taheri Andani, M., A. Mohammed, A. Jain and M. Ahmadian. 2018. Application of LIDAR technology for rail surface monitoring and quality indexing. *Proceedings of the Institution of Mechanical Engineers, Part F: Journal of Rail and Rapid Transit* 232(5):1398–1406. <https://doi.org/10.1177/0954409717727200>.

Yi, C., D. Lu, Q. Xie, S. Liu, H. Li, M. Wei and J. Wang. 2019. Hierarchical tunnel modeling from 3D raw LiDAR point cloud. *Computer-Aided Design* 114:143–154.

UAV Remote Sensing Assessment of Crop Growth

Freda Elikem Dorbu, Leila Hashemi-Beni, Ali Karimodini, and Abolghasem Shahbazi

Abstract

The introduction of unmanned-aerial-vehicle remote sensing for collecting high-spatial- and temporal-resolution imagery to derive crop-growth indicators and analyze and present timely results could potentially improve the management of agricultural businesses and enable farmers to apply appropriate solution, leading to a better food-security framework. This study aimed to analyze crop-growth indicators such as the normalized difference vegetation index (NDVI), crop height, and vegetated surface roughness to determine the growth of corn crops from planting to harvest. Digital elevation models and orthophotos generated from the data captured using multispectral, red/green/blue, and near-infrared sensors mounted on an unmanned aerial vehicle were processed and analyzed to calculate the various crop-growth indicators. The results suggest that remote sensing-based growth indicators can effectively determine crop growth over time, and that there are similarities and correlations between the indicators.

Introduction

During the last decade, there have been improvements in the agricultural sector through theoretical and technological developments in many fields, including chemistry, genetics, and robotics (Radoglou-Grammatikis *et al.* 2020), and there has been an increase in the estimated amount of investment toward the development of agricultural-based technology (Tsouros *et al.*, 2019). However, there is still a rising need to increase food production, because of the continuous increase in the human population and urbanization. The adoption of these scientific approaches aims to increase agricultural food by 70% by the year 2050, when the world's population is projected to be 9 billion (Grainger 2010; Perea-Moreno *et al.* 2019), with an increasing demand for crops from 2005 to 2050 (Tilman *et al.* 2011; Tian *et al.* 2021) and a stipulated decrease in cultivated area (Tsouros *et al.* 2019). Intensive use of available farmland to close the yield gaps and reduction of the expansion of agricultural lands could positively affect crop production and improve the supply chain necessary to meet crop demand (Foley *et al.* 2011; Tilman *et al.* 2011; J. Huang *et al.* 2019).

The linear relationship between population and agricultural growth necessitates the acceptance and advancement of a multi-disciplinary method that facilitates monitoring and evaluation of crop fields for growth assessment, through

timely collection and analysis of farm data, to inform decision making (Popescu *et al.*, 2020). In addition, other outcomes from agricultural activities, such as the emission of 30% to 35% of greenhouse gases (Foley *et al.* 2011) and nitrogen pollution due to incomplete absorption by plants (Stuart *et al.* 2014), could be solved by the adoption of a well-structured interdisciplinary approach to optimizing production. Finally, agricultural stakeholders would not be burdened with the limitations of practicing traditional agronomy, which involves expensive and time-consuming methods (Wei *et al.* 2018).

Precision agriculture and smart farming technologies observe and measure an area to respond to spatial and temporal variability in crop fields (Jeppesen *et al.* 2018). This mechanism aims to maximize inputs for more rewarding output without disturbing natural resources, so as to advance environmental sustainability and quality (Mulla *et al.* 2002; Gołaś *et al.* 2020). Whipker and Akridge (2008) estimate that adoption of precision agriculture could contribute to an increase of more than 30% in US agribusiness. Precision and smart agriculture involve the use of sensors and software, coupled with other technologies, to collect and transfer data without the assistance of humans. Precision farming enables monitoring of crop growth and other agronomy processes such as fertilizer application, disease detection, and irrigation routines. The use of such technologies helps in obtaining timely data from the farmland for crop management and decision making in an efficient manner (Aubert *et al.* 2012; Mulla 2013). However, prevailing issues such as compatibility, complexity, and interoperability slow down the rate at which precision agriculture is adopted (Aubert *et al.* 2012). Shadrin *et al.* (2020) provide an overview of the issues and challenges associated with precision agriculture. The main objectives in adopting precision agriculture are to increase crop yield, improve product quality, ensure efficient usage of production inputs, save energy, and prevent environmental pollution (Radoglou-Grammatikis *et al.* 2020).

Remote sensing has been an important technology in precision agriculture (Shafiee *et al.* 2021). In agriculture it involves the use of platforms such as unmanned aerial vehicles (UAVs), satellites, and piloted aircraft to observe and measure reflected radiation from the surfaces of soil and plant materials to ascertain their features. The technology has been applied to different agricultural applications (Pinter *et al.* 2003; Hashemi-Beni and Gebrehiwot 2020; Weiss *et al.* 2020), such as determining crop yield and biomass (Shanahan *et al.* 2001; Chao *et al.* 2019), water stress and nutrients (Tilling *et al.* 2007; Ihuoma and Madramootoo 2017), and weed infestations (Thorp and Tian 2004; Y. Huang *et al.* 2018), as well as detecting plant diseases (Buja *et al.* 2021). Most remote sensing-based agriculture studies have been based on images acquired by either satellite or piloted vehicle to monitor vegetation levels (Mora *et al.* 2017). However, satellite imagery has low spatial resolution, and limitations on the acquisition of temporal-resolution imagery because of the potential unavailability of the satellite at the stipulated time. In addition, image collection by

Freda Elikem Dorbu is with the Computational Data Science and Engineering Department, North Carolina A&T State University, Greensboro, NC 27411 (fedorbu@aggies.ncat.edu).

Leila Hashemi-Beni is with the Geomatics Program, Built Environment Department, North Carolina A&T State University, Greensboro, NC 27411 (lhashemibeni@ncat.edu).

Ali Karimodini is with the Electrical Engineering Department, North Carolina A&T State University, Greensboro, NC 27411 (akarimod@ncat.edu).

Abolghasem Shahbazi is with the Agricultural Science Department, North Carolina A&T State University, Greensboro, NC 27411 (ash@ncat.edu).

Contributed by Alper Yilmaz, August 30, 2021 (sent for review August 30, 2021).

Photogrammetric Engineering & Remote Sensing
Vol. 87, No. 12, December 2021, pp. 891–899.
0099-1112/21/891–899

© 2021 American Society for Photogrammetry
and Remote Sensing
doi: 10.14358/PERS.21-00060R2

satellites is sometimes disrupted by environmental conditions. The use of piloted aircraft is also costly, and deploying multiple flights to acquire extra crop images is often challenging. UAV-based remote sensing systems for crop monitoring are fairly cost-effective, easily retrieve field data, and are very fast. UAVs can be flown on demand at varying altitudes to capture high-spatial- and temporal-resolution data over a crop field. These attributes have contributed to the advancement of precision agriculture. UAVs can be equipped with sensors to monitor crops, evaluate the field, and provide information to assist in identifying problems such as diseases and pests and guide farmers to quickly solving farm-related issues.

UAVs have been used in precision agriculture for several applications, such as weed mapping, monitoring and estimation of vegetation yield, irrigation management, crop spraying, and monitoring of vegetation health and detection of diseases (Tsouros *et al.* 2019; Hashemi-Beni and Gebrehiwot 2020). Allred *et al.* (2018) investigated the use of UAVs in identifying drainage pipes on farms, which are useful to farmers for controlling the amount of water on a field. A lidar sensor mounted on a UAV can assist in determining crop production and health status; images retrieved by lidar have been used for textural analysis to estimate total plant volume and soil surface for particular crops (Christiansen *et al.* 2017). UAVs have been also used in collecting thermal and multispectral information from a field to estimate water stress and the health status of pomegranate crops in Greece (Katsigiannis *et al.* 2016). The nitrogen status of rice has been determined by analyzing hyperspectral data captured using a UAV (Zheng *et al.* 2016). The use of time-series vegetation indices can identify varying crop classes and also indicate growth patterns in crops (de Souza *et al.* 2015). Prediction of wheat yield has been achieved using multi-sensor and multi-temporal remote sensing images taken on different dates (Wang *et al.* 2014). X. Zhou *et al.* (2017) used both UAV-generated single and multi-temporal vegetation indices to predict rice yield. Shafiee *et al.* (2021) have shown that multi-temporal indices generated from time-series data are more highly correlated with crop yield than are single vegetation indices. Time-series UAV data have also been used to determine the pattern of height and phenological changes in each growth cycle of corn of different genotypes (Han *et al.* 2019). Yeom *et al.* (2019) used time-series vegetation indices to determine the differences between no-tillage and conventional-tillage agricultural practices and their effects.

In spite of these works, more research is still required to evaluate the performance of UAV time-series data for precision agriculture. In that context, our research aimed to investigate UAV-based time-series vegetation indices for monitoring and determining the impact of fertilizer application and prescribed burns at the beginning of planting on phenological changes in crops over time. In addition, we conduct analyses of time-series UAV data for monitoring and evaluation of the crop condition in a controlled cornfield, determine the efficiency of remote sensing-based crop-growth indicators and the similarities among them, and estimate the biomass yield of the crop in the field using the time-series UAV data.

The article is organized as follows: The next section explains the study area and data collected for the research. Then the research materials and methodology are described, followed by a presentation and discussion of the results. Last come conclusions and a summary of future research.

Study Area and Data

The study area is a 2-acre controlled test plot, of size 415×210 ft, located at the North Carolina A&T State University research farm in Greensboro, North Carolina. As shown in Figure 1, the plot was divided into three different blocks to evaluate the performance of UAV time-series data for crop-growth assessment considering the effects of burning (killing

the winter crop with herbicide) and/or fertilizing before planting. Blocks 1 and 2 (each 415×70 ft) both had winter crops that were not burned before the new planting. The difference between them is that block 1 received fertilizer and block 2 did not. Block 3 (450×120 ft) received a traditional treatment: burning the winter crop with herbicide before the new planting, and applying the recommended amounts of NPK fertilizer. Corn was planted on the entire field on 24 April 2020.



Figure 1. Study area: the block design of the field. Block 1 was not burned but fertilizer was applied; block 2 was not burned and received no fertilizer; and block 3 was both burned and fertilized.

A UAV was used for collection of red/green/blue and near-infrared imagery over the controlled plot; eight ground control points were implemented for georeferencing. The UAV collected time-series data at 40 and 70 m every 2 wk from seeding time (April 2020) to harvesting (August 2020). The flight altitude of 40 m provided higher-resolution imagery while reducing the image's coverage area, thus increasing the flight duration and number of images required to cover the area of interest. Both flights for each collection took place on the same day, with one flight deployed at the end of the other. This approach aimed to compare maps generated from the images of the field and study the impact of the imagery resolution on the crop-growth assessment. Table 1 describes the time-series data collected.

Table 1. Data collected by two sensors mounted on a UAV at different flight altitudes.

Number of GCPs	Sensors	Flight Altitudes	Spatial Resolutions	Temporal Resolution
8	RGB, NIR	40 and 70 m	1 and 1.9 cm	2 weeks apart

GCP = ground control point; NIR = near-infrared; RGB = red/green/blue; UAV = unmanned aerial vehicle.

Methodology

Data Processing

A structure-from-motion approach was used for 3D reconstruction of the farmland from the 80% overlapping images collected by the UAV. These methods use feature-based image-matching methods and collinearity conditions from camera alignment for, respectively, image-to-image registration and 3D surface construction (Hashemi-Beni *et al.*, 2018). The ground control points were used for georeferencing to ensure

the accuracy of the reconstructed 3D images. A digital elevation model (DEM) map was created after georeferencing, which was used for orthorectification and creation of the 3D model.

Identification of Crop-Growth Indicators

Crop-growth indicators are used as indices to determine changes that occur on a field during the growing season. Determination of these indicators enables timely collection of data from the field for making decisions and taking prompt action if required. The three important indicators of growth change studied in the research are the normalized difference vegetation index, roughness length, and crop-height change from the time of planting to harvesting.

Normalized Difference Vegetation Index (NDVI)

The NDVI, an extensively used vegetation index, indicates the greenness or the photosynthetic status of a vegetative area. It assists in determining the locations of water, bare soil, and plants, as well as whether plants are healthy or stressed. This knowledge is based on the reflectance received from crops. Crops that are healthy and actively photosynthesizing absorb most of the red light they receive and reflect much of the near-infrared light, and the estimated amount of red light reflected by stressed vegetation is greater than near-infrared. NDVI is calculated as (Hashim *et al.* 2019)

$$NDVI = \frac{(NIR - Red)}{(NIR + Red)} \quad (1)$$

Values range from -1 to +1 (Meneses-Tovar 2011; Alface *et al.* 2019), with those between -1 and 0 indicating bare soil, roads, dead plants, or water and those between 0 and 1 indicating live plants (Table 2). In positive values, lower ones indicate stressed or unhealthy plants, and higher ones indicate healthy plants. In this research, time-series NDVI raster layers were obtained by using a raster map algebra using Equation 1.

Vegetated-Surface Roughness Length

Roughness length (RL) is an expression of the variability of elevation of a topographic surface at a given scale, where the scale of analysis is determined by the size of the landforms or geomorphic features of interest, either local or regional. It shows the heterogeneity in land surface. Roughness of vegetated surfaces is dependent on the mean canopy height, the canopy structure, and the plant density (Jasinski and Crago 1999; Urrego *et al.* 2021). Although roughness length is identified by several models as a function of structural parameters of vegetation such as canopy area index, frontal area index (Raupach 1994; Hu *et al.* 2020), and leaf area index (Myneni *et al.* 2002; Hu *et al.* 2020), it closely correlates with NDVI during the period of crop growth (M. Yu *et al.* 2017; Schaudt and Dickinson 2000).

Surface RL measurements depict the nature of features of the land or farm. Table 3 describes the surface of a field based on estimated RL values obtained from analysis. A very rough field has vegetation like a young dense forest, indicating the springing up of new vegetation with 70% canopy density.

For this study, RL was estimated by first computing the total curvature of the individual digital elevation models and then deriving a focal statistic for calculating the standard deviation within a moving neighborhood window of 3×3 pixels. The raster was log-transformed to normalize and reduce skewness. The roughness index is calculated as (Korzeniowska *et al.* 2018)

$$\mu = \log_{10} \sqrt{\frac{\sum_{i=1}^n (x_i - \bar{x}_i)^2}{n}} \quad (2)$$

where x_i represents the curvature value of the center cell, \bar{x}_i represents the mean curvature, and n is the number of pixels (for a 3×3 kernel).

Table 2. Normalized difference vegetation index (NDVI) values indicating vegetation classes (Hashim *et al.* 2019).

Vegetation Class	Description	NDVI Value
Non-vegetation	Barren areas, built-up areas, road network	-1 to 0.199
Low vegetation	Shrub and grassland	0.2 to 0.5
High vegetation	Temperate and tropical urban forest	0.501 to 1.0

Table 3. Roughness-length thresholds (Wieringa 1992; J. Yu *et al.* 2021).

Roughness Length	Landscape Features	Class
0.03	Flat terrain with very low vegetation or grass	Open
0.10	Cultivated area, low crops	Roughly open
0.25	Open landscape, scattered shelter belts	Rough
0.5	Young dense forest	Very rough
1.0	Mature forest	Closed
≥2.0	Irregular distribution of large forest with clearings	Chaotic

Plant Height

Plant height, which is the distance from the highest point of a plant to the lowest point (ground), assists in evaluating both plant growth and yield (Bendig *et al.* 2015). It provides relevant parameters for assessing plant physiology, genetic traits, and environmental impacts (Malambo *et al.* 2018). Figure 2 shows the stages of growth of maize from planting time to harvest time, indicating the stipulated height at each time period and the percentages of water and fertilizer required (Colless 1992). The percentages were determined in the laboratory and will be used for comparison and validation of the UAV-generated information.

In this research, a time-series DEM was processed and used for estimating changes in crop heights across growth stages. The DEM of each time stamp was subtracted from the DEM of the beginning time, 30 April (planting stage). The resultant raster presents the height change, enabling identification of the growth cycle of the crop, which in turn assists in choosing appropriate crop-management practices from the available husbandry options. Height change can be represented mathematically as

$$\text{Height change} = ((\text{Current_time[DEM]} - \text{Planting_time[DEM]})) \quad (3)$$

Statistical Analysis

A quantitative analysis was conducted to study the time-series assessment of the growth indices from planting to harvesting. Thirty-six checkpoints with random distribution were generated for each treatment block on the field (Figure 3). Changes in NDVI, RL, and crop height over time were analyzed for the checkpoints.

Results

Analysis of the time-series UAV and geospatial data was done in Agisoft Photoscan and ArcGIS. All UAV images, taken at both 40 and 70 m, were processed, but for demonstration purposes, only the results from 70 m are shown. Time-series digital elevation models were used in estimating crop height and vegetated RL change, whereas orthomosaics were used in assessing time-series NDVI.

Crop-Growth Indicators

This section provides the results of the three indicators used to determine maize growth from the time of planting to harvest.

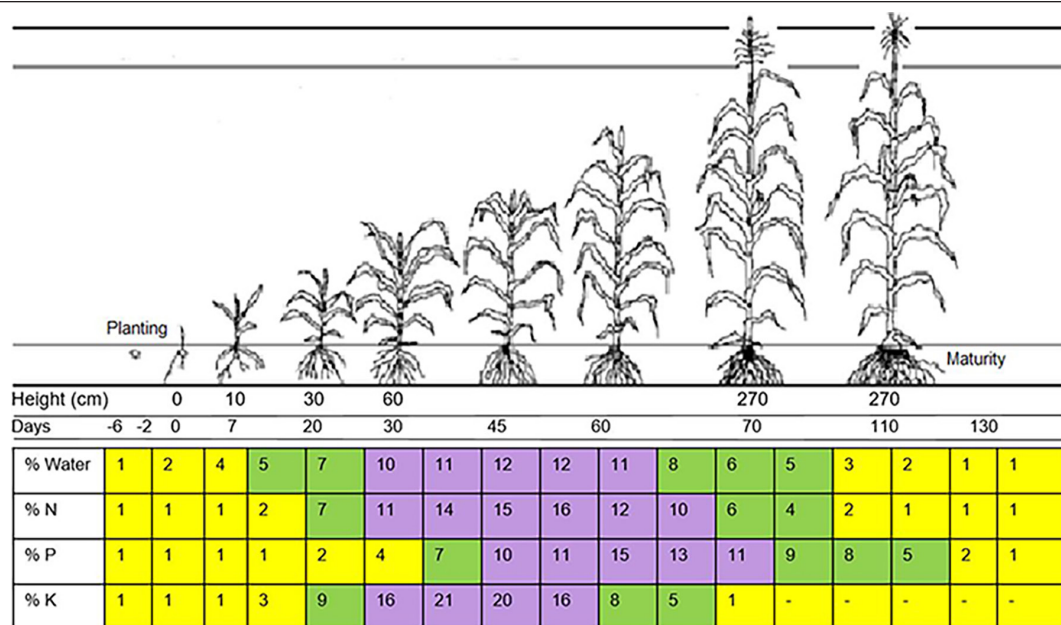


Figure 2. Maize growth cycle (Colless 1992), based on the application of recommended water and fertilizer (N, P, K), coupled with the presence of other essential elements such as sunlight.

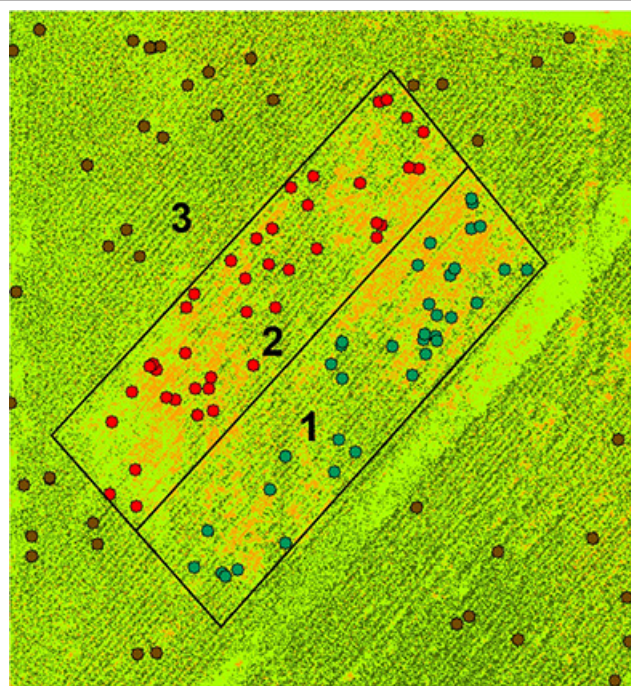


Figure 3. Checkpoints with random distribution in the treatment blocks. These checkpoints were used for assessing and comparing the crop-growth indicators (NDVI, RL, and height change) in the three blocks.

Time-Series NDVI

Results from NDVI analysis affirm the various block treatments applied to the study area. The variation in crop biomass yield across different blocks is due to the differences in block treatments. The time-series NDVI from April through August (Figure 4) shows the progression on the field from nearly bare earth to vast biomass development.

NDVI estimation for the first two blocks is high on 30 April due to the presence of winter crops on the field before and after the sowing of maize seeds. There was a concurrent increase in biomass in the whole field, including high

vegetation looking like a mature forest (NDVI 0.5–1) in the first two blocks from 12 to 29 May. However, biomass in these blocks began to deplete from 29 May until 26 June, when the depletion was massive. This was caused by the gradual withering of the winter crops and weeds in the region due to high temperatures in the summer.

There was a gradual increase in NDVI for block 3 from 30 April through 12 June, when there was a decline in biomass (Figure 5). This was due to the high average temperature of 84°F, which led to high evapotranspiration from the leaves and the soil surface in the field without replacement of water through irrigation, leading to the death of winter crops and thus low vegetation presence. Temperature and precipitation (Figure 6) are climatic conditions which greatly affect vegetation growth (Buitenwerf *et al.* 2015). Changes in climate cause variability in vegetation growth and influence functions that are associated with vegetation (Li *et al.* 2019). An example is the occurrence of frost, which leads to a reduction in vegetation biomass on a maize field (Raun *et al.* 2005). There was not much change in biomass on our whole field from 27 July to 11 August, as corn is ready for harvest as silage and not much phenological development occurred.

Time-Series RL

The vegetated-surface RL variation in the study area depicted a heterogeneous field along several rows. This heterogeneity implies a crop at different growth stages, and inconsistency in cultivation practices. The RL of the field on 30 April indicates open or flat terrain with both low vegetation or low grass-like biomass and vegetation looking like scattered shelter belts. The field can be classified as a rough open space. Vegetation increased by 12 May, when the field looked like a dense forest (Figure 7).

A marginal shift from heterogeneous to homogenous over the period 26 May to 12 June is associated with the increase in biomass along specific rows. From 26 June to 11 August, the study area excluding the alleyway was more closed, consisting of a lot of vegetation in the form of mature forest with a few chaotic instances. Except for blocks 1 and 2, in which some parts were indicated as rough, and the alleyway, the field was almost homogenous (Figure 8f). Corn crops at this time are usually ready to be harvested, since there is not

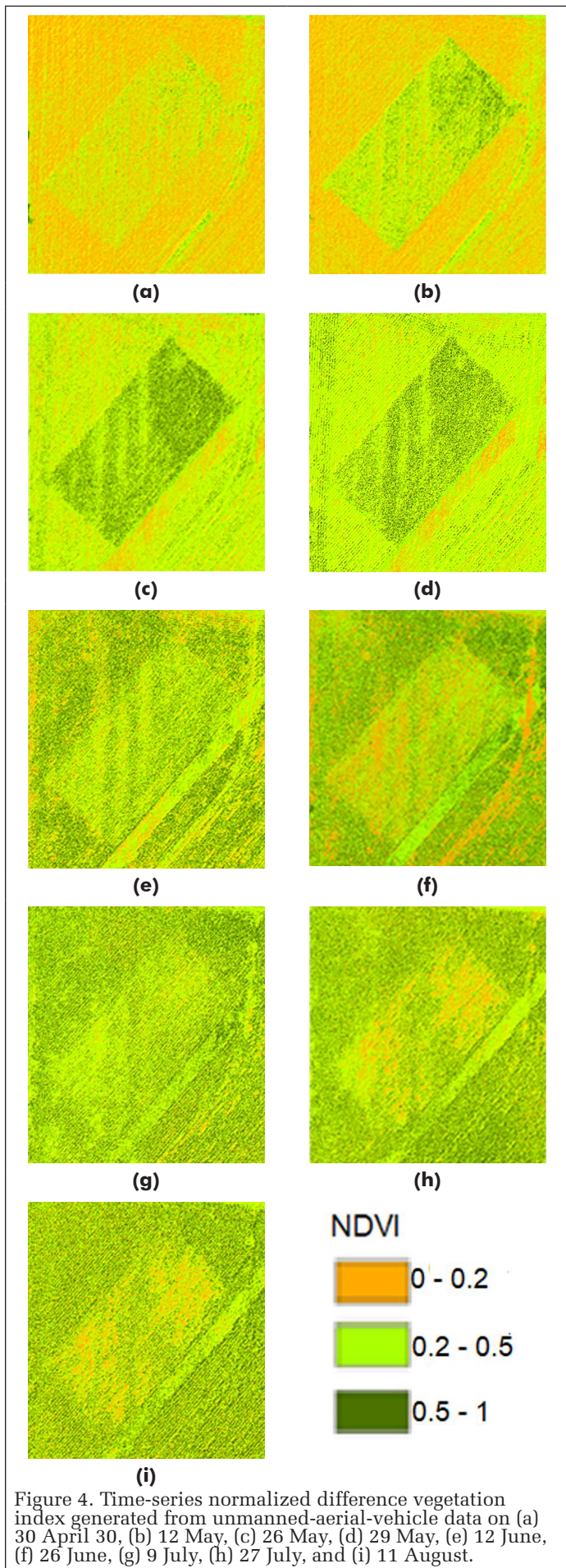


Figure 4. Time-series normalized difference vegetation index generated from unmanned-aerial-vehicle data on (a) 30 April, (b) 12 May, (c) 26 May, (d) 29 May, (e) 12 June, (f) 26 June, (g) 9 July, (h) 27 July, and (i) 11 August.

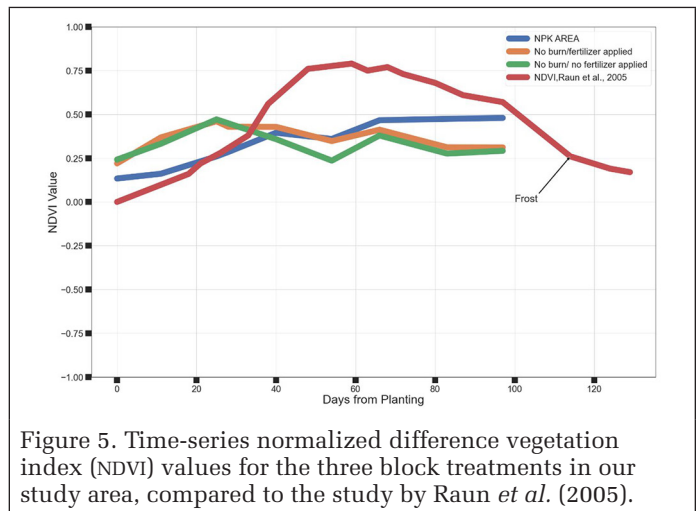


Figure 5. Time-series normalized difference vegetation index (NDVI) values for the three block treatments in our study area, compared to the study by Raun *et al.* (2005).

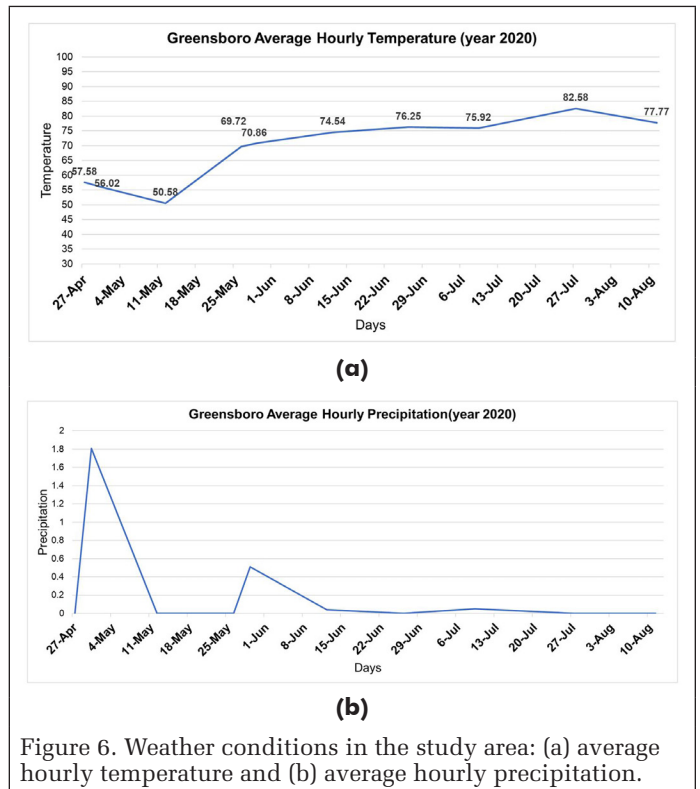


Figure 6. Weather conditions in the study area: (a) average hourly temperature and (b) average hourly precipitation.

much more change in the growth of the crop, and there is uniformity in the growth cycle with less alteration.

Time-Series Crop Height

Figure 9 presents the UAV-based time-series crop-height changes. Although the height estimation did not differentiate the types of vegetation present in the controlled field, the variation in height at the various growth stages assisted in differentiating corn from the winter crops. The decline in crop height on 12 June in the first two blocks was because the average hourly temperature was 75°F, with low precipitation (Figure 6), which led to the death of weeds and winter crops that could not survive the hot summer weather. However, there was an increase in crop height in block 3 due to the absence of winter crops and competition from weeds. The decline in crop height for all three blocks on 9 July shows the effect of lagging climatic conditions leading to the lodging of plants.

Lodging is a result of strong winds and rainstorms (Acorsi *et al.* 2019). These weather conditions lead to corn plants leaning flat to the ground (L. Zhou *et al.* 2020), and sometimes roots becoming dislocated from the soil or stems breaking,

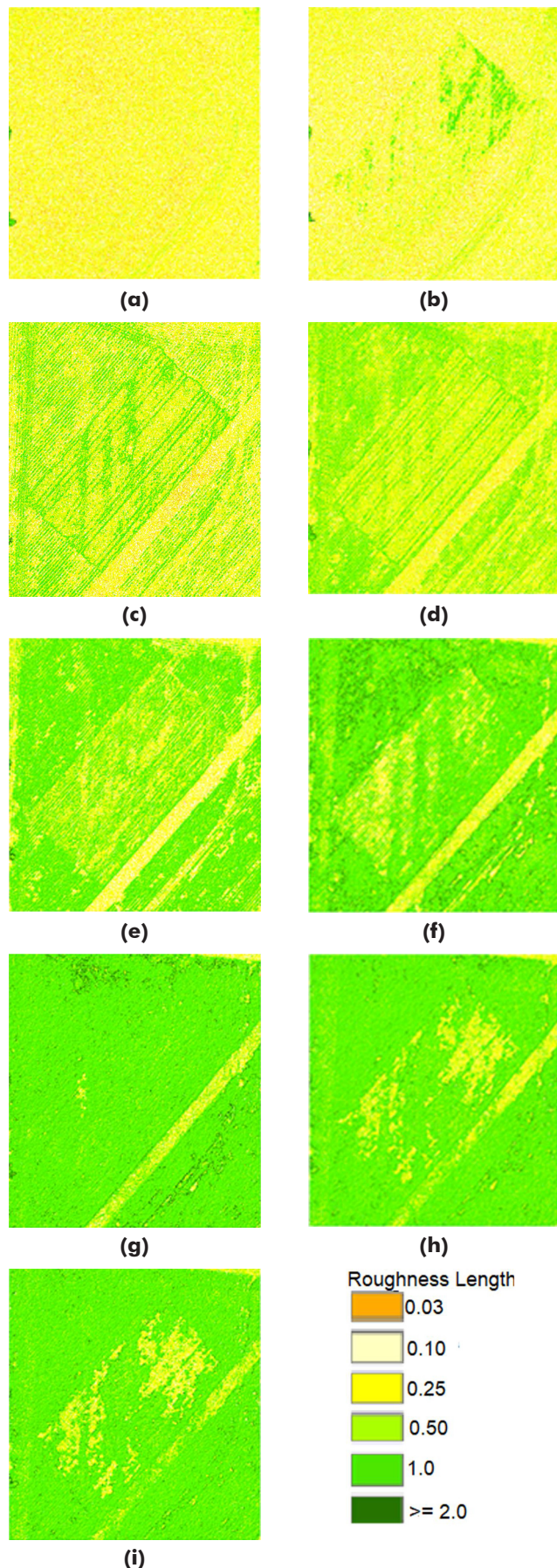


Figure 7. Time-series roughness length, showing the variability of the field surface based on the growth of crops and the canopy density on (a) 30 April, (b) 12 May, (c) 26 May, (d) 29 May, (e) 12 June, (f) 26 June, (g) 9 July, (h) 27 July, and (i) 11 August.

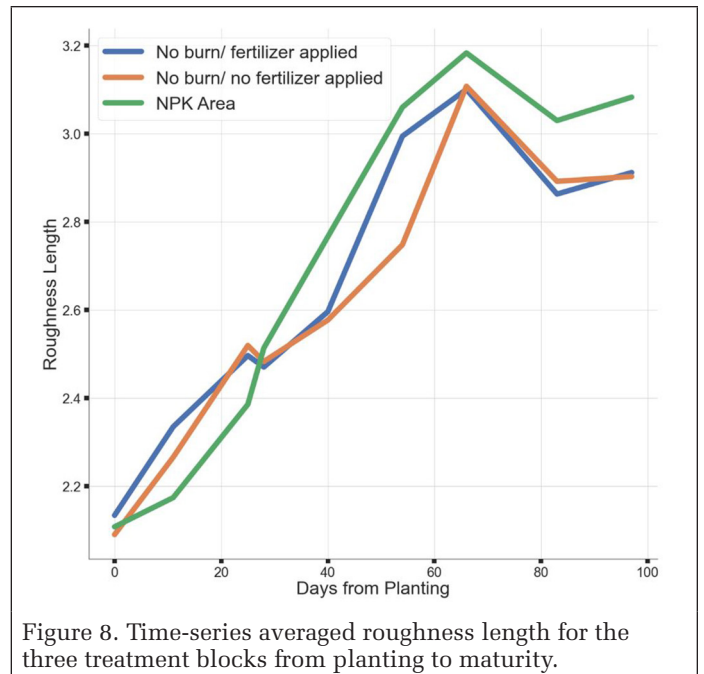


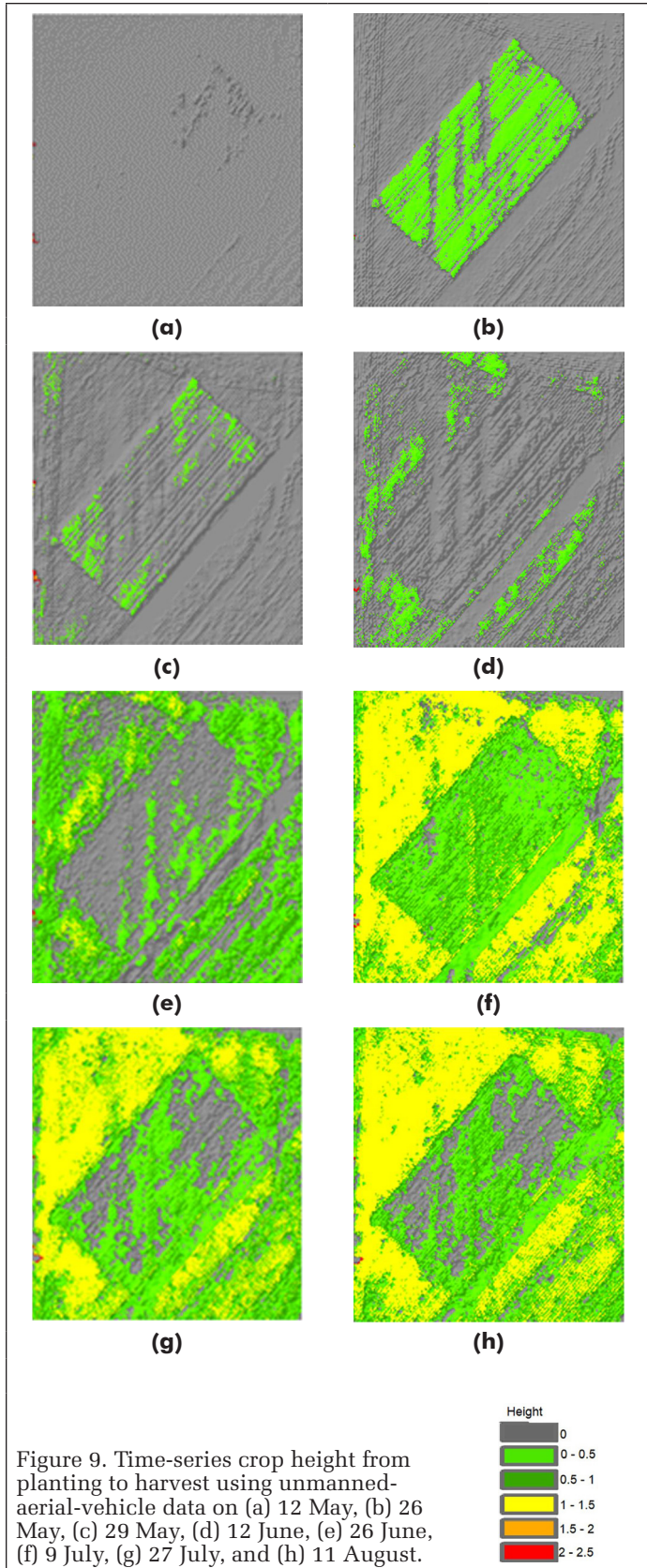
Figure 8. Time-series averaged roughness length for the three treatment blocks from planting to maturity.

reducing maize height. On 9 July, the average hourly precipitation in the study area was 0.05 in, with a wind speed of 13 mi per hr from the north-northeast. Corn height decreased after 9 July in all blocks and then resumed normal growth after 27 July (Figure 10). A correlation matrix for crop height in the three treatment blocks (Figure 11) showed a correlation of 0.93 between blocks 1 and 3, implying a 93% similarity in corn-height changes in the two blocks, which could be due to the presence of fertilization in both. The change in crop height in block 3 (treated with NPK fertilizer) was within a range of 0.5 to 1.5 m on 11 August, whereas the other blocks recorded changes of 0.1 to 0.5 m. Crop heights in the first two blocks are lower because of the competition for nutrients and moisture from unburned weeds.

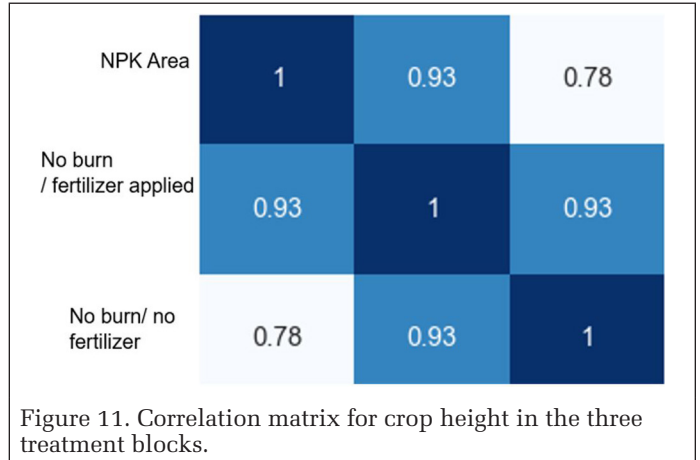
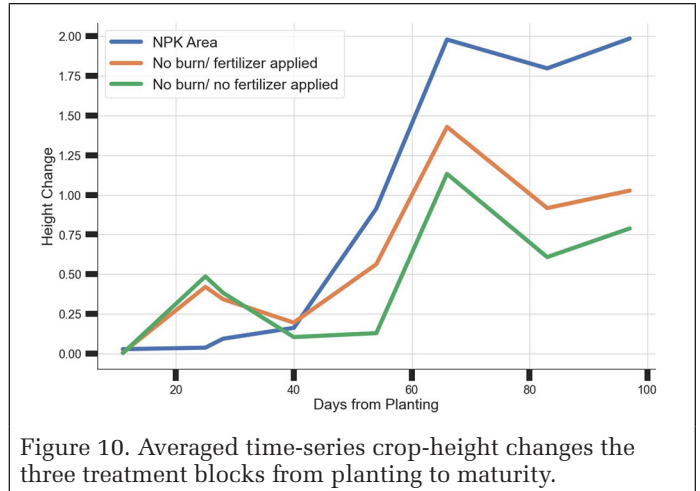
The UAV DEM generated from this study for each time stamp was used to estimate the surface roughness of the field and the change in crop height. Crops that are unevenly spaced and have a lot of seeds per hole encourage competition among the crop and weeds, leading to variability in the canopy surface and to crop failure. The use of UAV multi-temporal data captured the variability caused by these parameters, which can assist in replanting of crops to improve growth and eventually increase crop yield. Changes in crop height are attributed to phenological development in the crop. It is necessary to calculate the height to ensure that the crop has attained acceptable growth before harvesting and to determine fertilizer and water application during the growth cycle. The differences in biomass yield over the entire period assist in detecting unhealthy crops and informing decisions as to intervention to rescue the crop. They also assist in predicting crop yield based on reflection from time-series data of phenotypic development.

Conclusion

UAV has proven to be a reliable source for the collection of multi-temporal data irrespective of time sensitivity of the growth season. It is easily accessible and very flexible, and images can be taken repeatedly. Placement of ground control points on the field of study validates the UAV images collected and ensures accuracy of the 3D image constructed through georeferencing of point clouds. The UAV vegetation indices



evaluated in this study quickly indicated a change in vegetation from the time of planting to the time of harvest, compared to the traditional method of monitoring a field, which is time-consuming and labor-intensive. The normalized



difference vegetation index provided clear information on the vegetation status of the corn crop. Images acquired by remote sensing were used to determine the health status of the crop through estimating the NDVI. Low NDVI values imply crops that are either unhealthy or moderately healthy, whereas high values close to 1 indicate a healthy crop and provide information on biomass yield. UAV-generated time-series results indicated both healthy and unhealthy crop, with high and low vegetation in the field. This analytical result from the NDVI correlates with the vegetated-surface roughness length for each period, which indicates that the level of vegetation can be determined by other indices, not only NDVI. Remote sensing detected the presence of more biomass in the control block compared to the other two blocks, and the RL values implied that the field was heterogeneous due to factors such as plant spacing and density, plant height, and canopy structure for most of the growth cycle. Remote sensing technology indicated that the study area was a heterogeneous field for most of the period of crop growth, becoming slightly homogeneous in the latter stage of the cycle. The height-change results assisted in identifying the impact of weather conditions on the maize crop. In the future, we will use deep learning for classification purposes and time-series analysis.

Acknowledgments

This work was supported in part by the National Science Foundation under grants 1832110 (Developing a Robust, Distributed, and Automated Sensing and Control System for Smart Agriculture) and 1800768 (Remote Sensing for Flood Modeling and Management).

References

- Acorsi, M. G., M. Martello and G. Angnes. 2019. Identification of maize lodging: A case study using a remotely piloted aircraft system. *Engenharia Agrícola* 39 (special issue):66–73.
- Alface, A. B., S. B. Pereira, R. Filgueiras and F. F. Cunha. 2019. Sugarcane spatial-temporal monitoring and crop coefficient estimation through NDVI. *Revista Brasileira de Engenharia Agrícola e Ambiental* 23(5):330–335.
- Allred, B., N. Eash, R. Freeland, L. Martinez and D. Wishart. 2018. Effective and efficient agricultural drainage pipe mapping with UAS thermal infrared imagery: A case study. *Agricultural Water Management* 197:132–137.
- Aubert, B. A., A. Schroeder and J. Grimaudo. 2012. IT as enabler of sustainable farming: An empirical analysis of farmers' adoption decision of precision agriculture technology. *Decision Support Systems* 54(1):510–520.
- Bendig, J., K. Yu, H. Aasen, A. Bolten, S. Bennertz, J. Broscheit, M. L. Gny and G. Bareth. 2015. Combining UAV-based plant height from crop surface models, visible, and near infrared vegetation indices for biomass monitoring in barley. *International Journal of Applied Earth Observation and Geoinformation* 39:79–87.
- Buitenwerf, R., L. Rose and S. I. Higgins. 2015. Three decades of multi-dimensional change in global leaf phenology. *Nature Climate Change* 5(4):364–368. <https://doi.org/10.1038/nclimate2533>.
- Buja, I., E. Sabella, A. G. Monteduro, M. S. Chiriaco, L. De Bellis, A. Luvisi and G. Maruccio. 2021. Advances in plant disease detection and monitoring: From traditional assays to in-field diagnostics. *Sensors* 21(6):2129.
- Chao, Z., N. Liu, P. Zhang, T. Ying and K. Song. 2019. Estimation methods developing with remote sensing information for energy crop biomass: A comparative review. *Biomass and Bioenergy* 122:414–425.
- Christiansen, M. P., M. S. Laursen, R. N. Jørgensen, S. Skovsen and R. Gislum. 2017. Designing and testing a UAV mapping system for agricultural field surveying. *Sensors* 17(12):2703.
- Colless, J. (1992). Maize growing. NSW Agriculture: Orange, Australia.
- de Souza, C.H.W., E. Mercante, J. A. Johann, R.A.C. Lamparelli and M. A. Uribe-Opazo. 2015. Mapping and discrimination of soya bean and corn crops using spectro-temporal profiles of vegetation indices. *International Journal of Remote Sensing* 36(7):1809–1824.
- Foley, J. A., N. Ramankutty, K. A. Brauman, E. S. Cassidy, J. S. Gerber, M. Johnston, N. D. Mueller, C. O'Connell, D. K. Ray, P. C. West, C. Balzer, E. M. Bennett, S. R. Carpenter, J. Hill, C. Monfreda, S. Polasky, J. Rockström, J. Sheehan, S. Siebert, D. Tilman and D.P.M. Zaks. 2011. Solutions for a cultivated planet. *Nature* 478(7369):337–342.
- Goła, M., P. Sulewski, A. W s, A. Kłoczko-Gajewska and K. Pogodzi ska. 2020. On the way to sustainable agriculture—eco-efficiency of Polish commercial farms. *Agriculture* 10(10):438.
- Grainger, M. 2010. World Summit on Food Security (UN FAO, Rome, 16–18 November 2009). *Development in Practice* 20(6):740–742.
- Han, L., G. Yang, H. Dai, H. Yang, B. Xu, H. Feng, Z. Li and X. Yang. 2019. Fuzzy clustering of maize plant-height patterns using time series of UAV remote-sensing images and variety traits. *Frontiers in Plant Science* 10:926. <https://doi.org/10.3389/fpls.2019.00926>.
- Hashemi-Beni, L. and A. Gebrehiwot. 2020. Deep learning for remote sensing image classification for agriculture applications. *The International Archives of the Photogrammetry, Remote Sensing and Spatial Information Sciences* 44:51–54.
- Hashemi-Beni, L., J. Jones, G. Thompson, C. Johnson and A. Gebrehiwot. 2018. Challenges and opportunities for UAV-based digital elevation model generation for flood-risk management: A case of Princeville, North Carolina. *Sensors* 18(11):3843.
- Hashim, H., Z. Abd Latif and N. A. Adnan. 2019. Urban vegetation classification with NDVI threshold value method with very high resolution (VHR) Pleiades imagery. *The International Archives of the Photogrammetry, Remote Sensing and Spatial Information Sciences* 42(4/W16):237–240.
- Hu, X., L. Shi, L. Lin and V. Magliulo. 2020. Improving surface roughness lengths estimation using machine learning algorithms. *Agricultural and Forest Meteorology* 287:107956. <https://doi.org/10.1016/j.agrformet.2020.107956>.
- Huang, J., H. Ma, F. Sedano, P. Lewis, S. Liang, Q. Wu, W. Su, X. Zhang and D. Zhu. 2019. Evaluation of regional estimates of winter wheat yield by assimilating three remotely sensed reflectance datasets into the coupled WOFOST–PROSAIL model. *European Journal of Agronomy* 102:1–13.
- Huang, Y., K. N. Reddy, R. S. Fletcher and D. Pennington. 2018. UAV low-altitude remote sensing for precision weed management. *Weed Technology* 32(1):2–6.
- Ihuoma, S. O. and C. A. Madramootoo. 2017. Recent advances in crop water stress detection. *Computers and Electronics in Agriculture* 141:267–275.
- Jasinski, M. F. and R. D. Crago. 1999. Estimation of vegetation aerodynamic roughness of natural regions using frontal area density determined from satellite imagery. *Agricultural and Forest Meteorology* 94(1):65–77. [https://doi.org/10.1016/S0168-1923\(98\)00129-4](https://doi.org/10.1016/S0168-1923(98)00129-4).
- Jeppesen, J. H., E. Ebeid, R. H. Jacobsen and T. S. Toftegaard. 2018. Open geospatial infrastructure for data management and analytics in interdisciplinary research. *Computers and Electronics in Agriculture* 145:130–141.
- Katsigiannis, P., L. Misopolinos, V. Liakopoulos, T. K. Alexandridis and G. Zalidis. 2016. An autonomous multi-sensor UAV system for reduced-input precision agriculture applications. Pages PP–PP in *2016 24th Mediterranean Conference on Control and Automation (MED)*, held in Athens, Greece, 21–24 June 2016. Edited by J. Editor. Location: IEEE.
- Korzeniowska, K., N. Pfeifer and S. Landtwing. 2018. Mapping gullies, dunes, lava fields, and landslides via surface roughness. *Geomorphology* 301:53–67.
- Li, W., J. Du, S. Li, X. Zhou, Z. Duan, R. Li, S. Wu, S. Wang and M. Li. 2019. The variation of vegetation productivity and its relationship to temperature and precipitation based on the GLASS-LAI of different African ecosystems from 1982 to 2013. *International Journal of Biometeorology* 63(7):847–860. <https://doi.org/10.1007/s00484-019-01698-x>.
- Malambo, L., S. C. Popescu, S. C. Murray, E. Putman, N. A. Pugh, D. W. Horne, G. Richardson, R. Sheridan, W. L. Rooney, R. Avant, M. Vidrine, B. McCutchen, D. Baltensperger and M. Bishop. 2018. Multitemporal field-based plant height estimation using 3D point clouds generated from small unmanned aerial systems high-resolution imagery. *International Journal of Applied Earth Observation and Geoinformation* 64:31–42.
- Meneses-Tovar, C. L. 2011. NDVI as indicator of degradation. *Unasylva* 62(238):39–46.
- Mora, A., T.M.A. Santos, S. Łukasik, J.M.N. Silva, A. J. Falcão, J. M. Fonseca and R. A. Ribeiro. 2017. Land cover classification from multispectral data using computational intelligence tools: A comparative study. *Information* 8(4):147.
- Mulla, D. J., P. Gowda, W. C. Koskinen, B. R. Khakural, G. Johnson and P. C. Robert. 2002. Modeling the effect of precision agriculture: Pesticide losses to surface waters. In *Terrestrial Field Dissipation Studies*, ACS Symposium Series vol. 842, edited by E. L. Arthur, A. C. Barefoot and V. E. Clay, 304–317. Location: American Chemical Society.
- Mulla, D. J. 2013. Twenty five years of remote sensing in precision agriculture: Key advances and remaining knowledge gaps. *Biosystems Engineering* 114(4):358–371.
- Myneni, R. B., S. Hoffman, Y. Knyazikhin, J. L. Privette, J. Glassy, Y. Tian, Y. Wang, X. Song, Y. Zhang, G. R. Smith, A. Lotsch, M. Friedl, J. T. Morisette, P. Votava, R. R. Nemani and S. W. Running. 2002. Global products of vegetation leaf area and fraction absorbed PAR from year one of MODIS data. *Remote Sensing of Environment* 83(1–2):214–231. [https://doi.org/10.1016/S0034-4257\(02\)00074-3](https://doi.org/10.1016/S0034-4257(02)00074-3).
- Perea-Moreno, M.-A., E. Samerón-Manzano and A.-J. Perea-Moreno. 2019. Biomass as renewable energy: Worldwide research trends. *Sustainability* 11(3):863.

- Pinter Jr, P. J., J. L. Hatfield, J. S. Schepers, E. M. Barnes, M. S. Moran, C.S.T. Daughtry and D. R. Upchurch. 2003. Remote sensing for crop management. *Photogrammetric Engineering and Remote Sensing* 69(6):647–664.
- Popescu, D., F. Stoican, G. Stamatescu, L. Ichim and C. Dragana. 2020. Advanced UAV–WSN system for intelligent monitoring in precision agriculture. *Sensors* 20(3):817.
- Radoglou-Grammatikis, P., P. Sarigiannidis, T. Lagkas and I. Moscholios. 2020. A compilation of UAV applications for precision agriculture. *Computer Networks* 172:107148. <https://doi.org/10.1016/j.comnet.2020.107148>.
- Raun, W., J. B. Solie, K. L. Martin, K. W. Freeman, M. L. Stone, G. V. Johnson and R. W. Mullen. 2005. Growth stage, development, and spatial variability in corn evaluated using optical sensor readings. *Journal of Plant Nutrition* 28(1):173–182.
- Raupach, M. R. 1994. Simplified expressions for vegetation roughness length and zero-plane displacement as functions of canopy height and area index. *Boundary-Layer Meteorology* 71(1):211–216. <https://doi.org/10.1007/BF00709229>.
- Schaudt, K. J. and R. E. Dickinson. 2000. An approach to deriving roughness length and zero-plane displacement height from satellite data, prototyped with BOREAS data. *Agricultural and Forest Meteorology* 104(2):143–155.
- Shadrin, D., A. Menshchikov, A. Somov, G. Bornemann, J. Hauslage and M. Fedorov. 2020. Enabling precision agriculture through embedded sensing with artificial intelligence. *IEEE Transactions on Instrumentation and Measurement* 69(7):4103–4113. <https://doi.org/10.1109/TIM.2019.2947125>.
- Shafiee, S., L. M. Lied, I. Burud, J. A. Dieseth, M. Alsheikh and M. Lillemo. 2021. Sequential forward selection and support vector regression in comparison to LASSO regression for spring wheat yield prediction based on UAV imagery. *Computers and Electronics in Agriculture* 183:106036.
- Shanahan, J. F., J. S. Schepers, D. D. Francis, G. E. Varvel, W. W. Wilhelm, J. M. Tringe, M. R. Schlemmer and D. J. Major. 2001. Use of remote sensing imagery to estimate corn grain yield. *Agronomy Journal* 93(3):583–589.
- Stuart, D., R. L. Schewe and M. McDermott. 2014. Reducing nitrogen fertilizer application as a climate change mitigation strategy: Understanding farmer decision-making and potential barriers to change in the US. *Land Use Policy* 36:210–218.
- Thorp, K. R. and L. F. Tian. 2004. A review on remote sensing of weeds in agriculture. *Precision Agriculture* 5(5):477–508.
- Tian, X., B. A. Engel, H. Qian, E. Hua, S. Sun and Y. Wang. 2021. Will reaching the maximum achievable yield potential meet future global food demand? *Journal of Cleaner Production* 294:126285. <https://doi.org/10.1016/j.jclepro.2021.126285>.
- Tilling, A. K., G. J. O’Leary, J. G. Ferwerda, S. D. Jones, G. J. Fitzgerald, D. Rodriguez and R. Belford. 2007. Remote sensing of nitrogen and water stress in wheat. *Field Crops Research* 104(1–3):77–85.
- Tilman, D., C. Balzer, J. Hill and B. L. Befort. 2011. Global food demand and the sustainable intensification of agriculture. *Proceedings of the National Academy of Sciences, USA* 108(50):20260–20264.
- Tsouros, D. C., S. Bibi and P. G. Sarigiannidis. 2019. A review on UAV-based applications for precision agriculture. *Information* 10(11):349.
- Urrego, J.P.F., B. Huang, J. S. Næss, X. Hu and F. Cherubini. 2021. Meta-analysis of leaf area index, canopy height and root depth of three bioenergy crops and their effects on land surface modeling. *Agricultural and Forest Meteorology* 306:108444. <https://doi.org/10.1016/j.agrformet.2021.108444>.
- Wang, L., Y. Tian, X. Yao, Y. Zhu and W. Cao. 2014. Predicting grain yield and protein content in wheat by fusing multi-sensor and multi-temporal remote-sensing images. *Field Crops Research* 164:178–188.
- Wei, M., B. Qiao, J. Zhao and X. Zuo. 2018. Application of remote sensing technology in crop estimation. Pages PP–PP in *2018 IEEE 4th International Conference on Big Data Security on Cloud (BigDataSecurity), IEEE International Conference on High Performance and Smart Computing (HPSC), and IEEE International Conference on Intelligent Data and Security (IDS)*, held in Omaha, Neb., 3–5 May 2018. Edited by J. Editor. Location: IEEE.
- Weiss, M., F. Jacob and G. Duveiller. 2020. Remote sensing for agricultural applications: A meta-review. *Remote Sensing of Environment* 236:111402. <https://doi.org/10.1016/j.rse.2019.111402>.
- Whipker, L. D. and J. T. Akridge. 2008. *2008 Precision Agricultural Services Dealership Survey Results*. Retrieved from
- Wieringa, J. 1992. Updating the Davenport roughness classification. *Journal of Wind Engineering and Industrial Aerodynamics* 41(1–3):357–368. [https://doi.org/10.1016/0167-6105\(92\)90434-C](https://doi.org/10.1016/0167-6105(92)90434-C).
- Yeom, J., J. Jung, A. Chang, A. Ashapure, M. Maeda, A. Maeda and J. Landivar. 2019. Comparison of vegetation indices derived from UAV data for differentiation of tillage effects in agriculture. *Remote Sensing* 11(13):1548.
- Yu, J., T. Stathopoulos and M. Li. 2021. Estimating exposure roughness based on Google Earth. *Journal of Structural Engineering* 147(3):04020353.
- Yu, M., B. Wu, N. Yan, Q. Xing and W. Zhu. 2017. A method for estimating the aerodynamic roughness length with NDVI and BRDF signatures using multi-temporal Proba-V data. *Remote Sensing* 9(1):6.
- Zheng, H., X. Zhou, T. Cheng, X. Yao, Y. Tian, W. Cao and Y. Zhu. 2016. Evaluation of a UAV-based hyperspectral frame camera for monitoring the leaf nitrogen concentration in rice. In *2016 IEEE International Geoscience and Remote Sensing Symposium (IGARSS)*, held in Beijing, China, 10–15 July 2016.
- Zhou, L., X. Gu, S. Cheng, G. Yang, M. Shu and Q. Sun. 2020. Analysis of plant height changes of lodged maize using UAV-LiDAR data. *Agriculture* 10(5):146.
- Zhou, X., H. B. Zheng, X. Q. Xu, J. Y. He, X. K. Ge, X. Yao, T. Cheng, Y. Zhu, W. X. Cao and Y. C. Tian. 2017. Predicting grain yield in rice using multi-temporal vegetation indices from UAV-based multispectral and digital imagery. *ISPRS Journal of Photogrammetry and Remote Sensing* 130:246–255.

IN-PRESS ARTICLES

- Qing Ding, Zhenfeng Shao, Xiao Huang, Orhan Altan, and Yewen Fan. Improving Urban Land Cover Mapping with the Fusion of Optical and SAR Data Based on Feature Selection Strategy.
- Clement E. Akumu and Eze O. Amadi. Examining the Integration of Landsat Operational Land Imager (OLI) with Sentinel-1 and Vegetation Indices in Mapping Southern Yellow Pines (Loblolly, Shortleaf and Virginia Pines).
- Xinyu Ding and Qunming Wang. Augmented Sample-Based Real-Time Spatiotemporal Spectral Unmixing.
- Muhammad Nasar Ahmad, Zhenfeng Shao, and Orhan Altan. Effect of Locust Invasion and Mitigation Using Remote Sensing Techniques: A Case Study of North Sindh Pakistan.
- Raechel Portelli, Paul Pope. Remote Sensing and Human Factors Research: A Review.
- Weixun Zhou, Wanxuan Geng, Shuanggen Jin. Multi-View Urban Scene Classification With A Complementary Information Learning Model.
- Jun Xu, Jiansong Li, Hao Peng, Yanjun He, and Bin Wu. Information Extraction from High-Resolution Remote Sensing Images Based on Multi-Scale Segmentation and Case-Based Reasoning.
- Xuehan Wang, Zhenfeng Shao, Xiao Huang, and Deren Li. Spatiotemporal Temperature Fusion Based on a Deep Convolutional Network.
- Fan Yang, Zhiwei Fan, Chao Wen, Xiaoshan Wang, Xiaoli Li, Zhiqiang Li, Xintao Wen, and Zhanyu Wei. Three-Dimensional Point Cloud Analysis for Building Seismic Damage Information.
- Steven Spiegel, Casey Shanks, and Jorge Chen. Effectiveness of Deep Learning Trained on SynthCity Data for Urban Point-Cloud Classification.
- Linze Bai, Qimin Cheng, Yuxuan Shu, and Sihang Zhang. Estimating the Aboveground Biomass of Urban Trees by Combining Optical and LiDAR Data: A Case Study of Hengqin, Zhuhai, China.
- Qimin Cheng, Haiyan Huang, Yin Pan, Neema Nicodemus Lyimo, Hao Peng, Gui Cheng. Cloud Detection in ZY-3 Multi-angle Remote Sensing Images.
- Xuzhe Duan, Qingwu Hu, Pengcheng Zhao, and Shaohua Wang. A low-cost and portable indoor 3D mapping approach using biaxial line laser scanners and a one-dimension laser rangefinder integrated with MEMS.
- Shaohua Wang, Qingwu Hu, Pengcheng Zhao. A low-cost and portable indoor 3D mapping approach using biaxial line laser scanners and a one-dimension laser rangefinder integrated with MEMS.
- Pennan Chinnasamy, Neetu Singh, Shivanand Mallikarjun Nalgire, Meeta Gupta. Potential of open source remote sensing data for improved spatiotemporal monitoring of inland water quality in India: Case study of Gujarat.
- Jantien Stoter, Ravi Peters, Balázs Dukai, Stelios Vitalis, Jordi van Liempt. Automated 3D reconstruction of LoD2 and LoD1 models for all 10 million buildings of the Netherlands.
- Muhammad Nasar Ahmad, Qimin Cheng, Fang Luo. Dynamic linkage between urbanization, electrical power consumption and suitability analysis using Remote sensing and GIS techniques.
- Mahendra Rajitha Udawalpola, Amit Hasan, Anna K. Liljedahl, Aiman Soliman, Jeffrey Terstriep, Chandri Witharna. An Optimal GeoAI Workflow for Pan-Arctic Permafrost Feature Detection from High-Resolution Satellite Imagery.

MSegnet, a Practical Network for Building Detection from High Spatial Resolution Images

Bo Yu, Fang Chen, Ying Dong, Lei Wang, Ning Wang, and Aqiang Yang

Abstract

Building detection in big earth data by remote sensing is crucial for urban development. However, improving its accuracy remains challenging due to complicated background objects and different viewing angles from various remotely sensed images. The hereto proposed methods predominantly focus on multi-scale feature learning, which omits features in multiple aspect ratios. Moreover, postprocessing is required to refine the segmentation performance. We propose modified semantic segmentation (MSegnet), a single-shot semantic segmentation model based on a matrix of convolution layers to extract features in multiple scales and aspect ratios. MSegnet consists of two modules: backbone feature learning and matrix convolution to conduct vertical and horizontal learning. The matrix convolution comprises a set of convolution operations with different aspect ratios. MSegnet is applied to a public building data set that is widely used for evaluation and shown to achieve satisfactory accuracy, compared with the published single-shot methods.

Introduction

Urban expansion is occurring at a high speed and urgently demands efficient building detection from large-scale, remotely sensed images (Chen et al. 2020; Ning and Lin 2017). An accurate building inventory is required for both military and civilian applications, including urban planning, disaster emergency, and navigation (Liu et al. 2019; Qin et al. 2020). However, due to technological limits, a significant challenge remains in automatically detecting buildings from high spatial resolution images with a reliable accuracy (Ning et al. 2020).

Semantic segmentation is a practical approach to deal with complicated background objects in building detection (Wang et al. 2020). It represents an important research topic in computer vision as it can segment the image by assigning each pixel in the input image with a semantic label. Owing to the rapid development of deep neural networks, semantic segmentation has significantly improved (Yurtkulu et al. 2019). Numerous

network structures have been proposed and achieved remarkable performance. The fully convolutional network (FCN) (Shelhamer et al. 2017) is considered a milestone in semantic segmentation. It replaces a fully connected layer using convolution operation and overcomes the requirement of a specific input image size. However, it is not sensitive to the details of the image and lacks spatial consistency among neighboring pixels. U-Net (Ronneberger et al. 2015), semantic segmentation (SegNet) (Badrinarayanan et al. 2017), pyramid scene parsing network (PSPNet) (Zhao et al. 2017), deconvolution network (DeconvNet) (Noh et al. 2015), and DeepLab series (Chen et al. 2018) models have been proposed for pixel-based segmentation and achieved remarkable accuracies. U-Net takes into context information by concatenation through skip connection so that the decoder can learn the lost feature in each encoder (Ronneberger et al. 2015). SegNet can maintain the integrity of high-frequency details in the image by upsampling the feature map using unpooling operation in the decoder (Badrinarayanan et al. 2017). PSPNet and DeepLab series models improve the segmentation using a spatial pooling module with different strategies to capture multi-scale features. However, most of these models require postprocessing to refine the segmentation performances, especially when applied to building detection (Alshehhi et al. 2017). The commonly used postprocessing strategies comprise conditional random field (Lafferty et al. 2002) and simple linear iterative clustering (Kim et al. 2013). Moreover, the pyramid pooling module in PSPNet and DeepLab series models, which is aimed at learning multi-scale features, lacks feature learning with multiple aspect ratios.

Inspired by MatrixNet (Rashwan et al. 2019), modified semantic segmentation (MSegnet), an end-to-end semantic segmentation framework, is proposed in this paper. MatrixNet proposes a bounding box for each object in the image by regressing the coordinates of the center pixel or anchor pixels. Its framework enlarges the pyramid network structure by adding convolution operations with kernels of different height-width ratios, such that features with multiple scales and aspect ratios can be learned. It outperforms all single-shot object detectors on the Microsoft Common Objects in Context benchmark (Lin et al. 2014). In contrast to MatrixNet, MSegnet is designed to segment buildings at pixel-level from high spatial resolution images and it is evaluated on the Wuhan University (WHU) building data set (Ji et al. 2019), a widely used public data set to evaluate the performance in building detection. It outperforms the published one-shot methods. The main contributions of this study are listed as follows:

1. A novel semantic segmentation framework is proposed by learning features using a matrix of convolution operations.
2. Satisfactory performances were achieved by comparison with published one-shot frameworks in one widely used public building detection data set.

Photogrammetric Engineering & Remote Sensing
Vol. 87, No. 12, December 2021, pp. 901–906.
0099-1112/21/901–906

© 2021 American Society for Photogrammetry
and Remote Sensing
doi: 10.14358/PERS.21-00016R2

Bo Yu, Fang Chen, Ning Wang, and Aqiang Yang are with Key Laboratory of Digital Earth Science, Aerospace Information Research Institute, Chinese Academy of Sciences, Beijing 100094, China.

Fang Chen and Ning Wang are also with Hainan Key Laboratory of Earth Observation, Aerospace Information Research Institute, Chinese Academy of Sciences, Sanya 572029, China. Fang Chen is also with the University of Chinese Academy of Sciences, Beijing 100049, China.

Fang Chen and Lei Wang are with the State Key Laboratory of Remote Sensing Science, Aerospace Information Research Institute, Chinese Academy of Sciences, Beijing 100094, China.

Ying Dong is with the College of Economics and Management, South China Agricultural University, Guangzhou, Guangdong, Guangdong 510642, China (aliceying@scau.edu.cn).

Contributed by Ribana Roscher, April 6, 2021 (sent for review June 7, 2021; reviewed by Chengyi Wang, DongMei Chen).

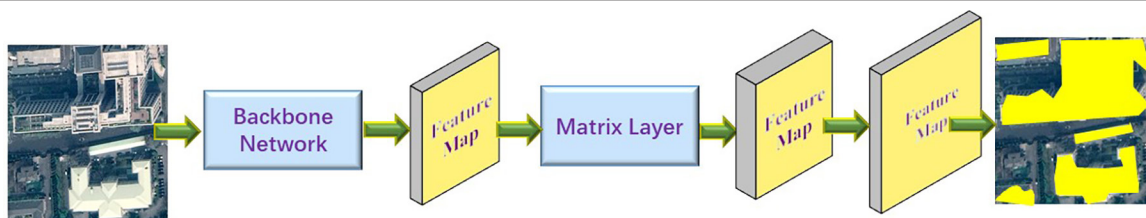


Figure 1. Flowchart of proposed MSegnet.

Related Studies

We present a literature review on building detection from optical remotely sensed images. Generally, studies conducting building detection witnessed three processes, namely, manual thresholding, machine learning, and deep learning-based modeling. The first two processes are recognized as traditional methods, focusing on spectral and textural feature engineering. The scale-invariant feature transform (Lowe 2004), Histogram of Oriented Gradients (Dalal and Triggs 2005), local binary patterns (Ojala *et al.* 2002), grey level co-occurrence (Gomez *et al.* 2012), and Haar wavelet transform (Guf and Jiang 1996) are the commonly used features in building detection (Konstantinidis *et al.* 2017). Moreover, geometry properties, material properties (Lee *et al.* 2003; Mayer 1999), and graph-based theory (Walde *et al.* 2013) have been explored as well. The random forest (Breiman 2001), support vector machine (Burges 1998), Bayesian maximum likelihood method (Khoshelham *et al.* 2008), and Adaboost (Fleyeh and Davami 2013) are the commonly used machine learning models and have achieved outstanding performances in building detection (Cetin *et al.* 2010; Hänsch and Hellwich 2010; Li *et al.* 2011). However, the methods mentioned above require massive feature engineering, which relies heavily on the expertise and experience in related applications.

The advent of deep learning has given rise to significant improvements in building detection and avoided the feature engineering requirement. U-net has been widely used in building detection (Hamaguchi and Hikosaka 2018; Li *et al.* 2018); it represents a simple encoder-decoder network and efficient implementation. Apart from U-Net, there is significant research in applying other semantical segmentation model structures in building detection, such as Mask-Regional Convolutional Neural Network (Zhao *et al.* 2018), LinkNet (Golovanov *et al.* 2018), and DeepLab (Boonpook *et al.* 2018). The published studies predominantly adopt postprocessing steps to refine the segmentation results, which are time consuming (Yu *et al.* 2018). Moreover, the segmentation described above lacks multi-scale feature learning in different directions. To address this issue, we propose MSegnet, inspired by MatrixNet. MSegnet is a pixel-wise end-to-end semantic segmentation framework wherein postprocessing is not required. Because most buildings in high spatial resolution images assume different spectral characteristics with different shapes and orientations, the structure of MSegnet provides a potential approach to learn complicated features of buildings from various background objects.

Proposed Framework

The general pipeline of the proposed MSegnet is illustrated in Figure 1. It mainly consists of two components, backbone network and matrix convolution layer. The backbone network uses ResNet-50 (He *et al.* 2016), a 50-layer residual network. ResNet is a widely used backbone structure for encoding input images into feature maps (Peng *et al.* 2020; Qin *et al.* 2020). The reason that we use a 50-layer residual network is due to the fact that the buildings in our study have large variability in shapes and sizes. Small buildings will be easily filtered out by deep residual network, and big buildings will be likely learned insufficiently by a shallow residual network.

Table 1. Network structure of ResNet-50.

Block Name	Convolution Operation	Number of Blocks
Conv1	7×7×64	1
	3×3 max pooling	
Conv2	1×1×64	3
	3×3×64	
	1×1×256	
Conv3	1×1×128	4
	3×3×128	
	1×1×512	
Conv4	1×1×256	6
	3×3×256	
	1×1×1024	
Conv5	1×1×512	3
	3×3×512	
	1×1×2048	

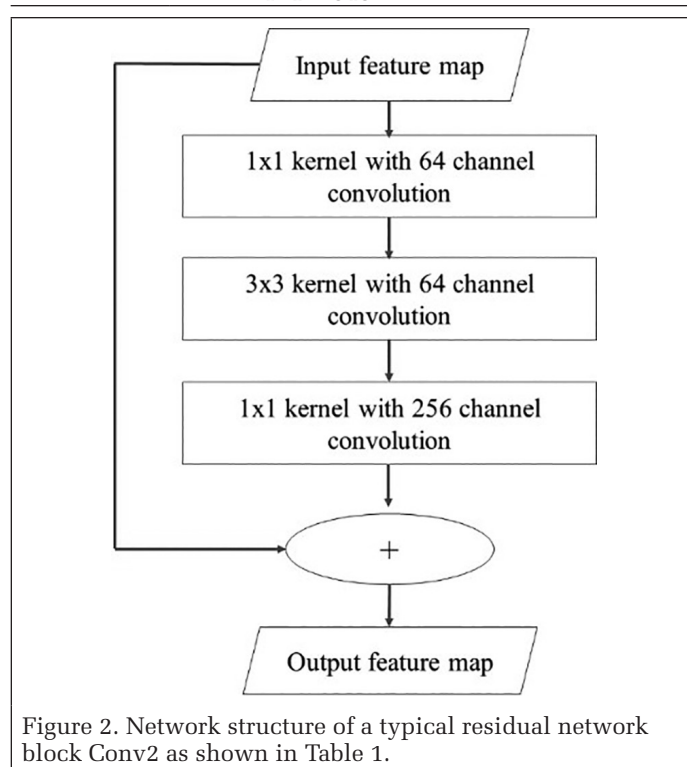
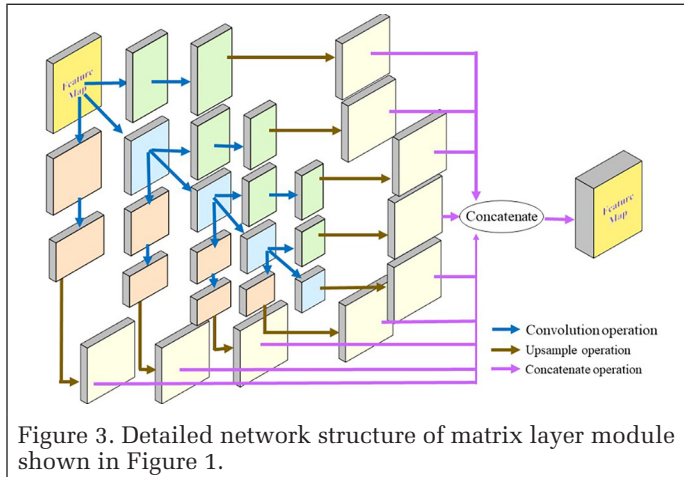


Figure 2. Network structure of a typical residual network block Conv2 as shown in Table 1.

Therefore, we used ResNet-50 to generally learn features for multi-scale buildings in our study. The network structure of ResNet-50 is demonstrated in Table 1, wherein a detailed residual network structure of typical convolution block Conv2 is demonstrated as an example in Figure 2. The input image is firstly convoluted by a 64-channel 7×7 kernel and encoded by a 3×3 maximum pooling operation. Following Conv1 convolution operation in Table 1, four convolution blocks organized in a residual manner are conducted gradually to generate the feature map used for further extraction in the module of Matrix Layer, as demonstrated in Figure 1. The number of each convolution block listed in Table 1 indicates

the number of times each corresponding convolution block repeats on the feature map. In terms of each residual convolution block, as demonstrated in Figure 2, the input feature map is convoluted by a 1×1 , 3×3 , and 1×1 kernel with different channels continuously and added directly with the feature map after continuous convolution to generate the output feature map. Such addition enables the network to alleviate the problem of gradient disappearance that increasing depth in the deep neural network brings about (He and Sun 2015).



The feature maps encoded by ResNet-50 are used to learn multi-scale features with different aspect ratios by the matrix convolution layer. Its detailed network structure is shown in Figure 3, wherein multiple convolution operations with strides of 1×2 , 2×1 , and 2×2 are conducted to down-sample the input feature maps horizontally, vertically, and diagonally, respectively. The corresponding calculated feature maps are displayed in green, pink, and blue. Each output feature map in each direction is upsampled by a bilinear operation to the same size and finally concatenated as the output feature map of the Matrix convolution layer. The concatenated feature map is further upsampled and used for generating a pixel-wise label prediction image, as shown in Figure 1.

The activation function of the proposed network is the Rectified Linear Unit (Nair and Hinton 2010), which is commonly used in neural networks (Ronneberger *et al.* 2015; Shelhamer *et al.* 2017). Moreover, focal loss function (Lin *et al.* 2020) is adopted for training our network. It was proposed to deal with the unbalanced sample distribution issue in the one-shot segmentation framework. Compared with the traditional cross entropy loss function in Equation 1, the focal loss enables the network to focus more on difficult samples that are easily to be misclassified by adding *gamma*. For example, a positive sample *S* has a prediction probability of 0.98; thus, its gamma power of $1-0.98$ will be very small, and the focal loss will be small as well. On the condition that the positive sample has a prediction probability of 0.21, its gamma power will be very large, and the corresponding focal loss will be large as well. The same principle applies to negative samples. Therefore, this mechanism reduces the impact of samples that are easily classified and enhances the difficult ones. This is more effective in training models. Furthermore, α is added into the L_{focal} expression in Equation 2 as a balancing element to balance the uneven proportion between positive and negative samples. This proves to be significant in our research, as building samples are comparatively fewer than background objects in high spatial resolution images. Following the studies in Lin *et al.* (2020), gamma is set to 2, and α is set to 0.25 in our framework.

$$L_{ce} = -gt(x, y) \log \text{pred}(x, y) - (1 - gt(x, y)) \log(1 - \text{pred}(x, y)) \quad (1)$$

$$L_{focal} = -\alpha gt(x, y)(1 - \text{pred}(x, y))^{\gamma} \log \text{pred}(x, y) - (1 - \alpha)(1 - gt(x, y)) \text{pred}(x, y)^{\gamma} \log(1 - \text{pred}(x, y)) \quad (2)$$

Experiments

To evaluate the robustness and reliability of our proposed MSegnet, we apply it on the WHU building data set (Ji *et al.* 2019), a public data set widely used for evaluation purposes (Lin *et al.* 2019; Liu *et al.* 2019). The corresponding evaluation statistics are calculated and compared with other published performances.

Data Set

The WHU building data set spans 450 km², comprising Christchurch and New Zealand. The images adopted in our study include approximately 187 000 buildings with a spatial resolution of 0.3 m, and all images were cropped to a 512 × 512 pixel size for each tile. The training data set includes 4736 tiles, containing approximately 130 500 buildings. Approximately 14 500 buildings from 1036 tiles are assigned to the evaluation data set, and the test data set contains 2416 tiles with ~42 000 building examples. Its ground truth images are labeled as building and nonbuilding.

Implementation Details and Evaluation Metrics

Our proposed model is implemented on the Pytorch platform. The experiments are conducted with two global positioning units (GPUs) with a memory of 12 GB each. Adaptive moment estimation optimization strategy (Kingma and Ba 2014) is adopted to optimize the proposed network. The initial learning rate is set to 0.0001 and divided by 10 after 100 epochs. Regarding the GPU memory and the complexity of our model, the batch size is set to four, with a chunk size of two for each GPU.

In accordance with most recent studies on building detection (Alshehhi *et al.* 2017; Boonpook *et al.* 2018; Lin *et al.* 2019; Liu *et al.* 2019), the precision, recall, F1-score, and intersection-over-union (IOU) are calculated as evaluation statistics. Precision represents the percentage of segmented building pixels that are correctly classified. Recall indicates the percentage of ground truth building pixels that are correctly segmented as buildings. The F1-score is a comprehensive index demonstrating the general performance. IOU is calculated by division between the corrected classified building pixel number over the pixel number after subtracting corrected classified background pixels from the total image pixels.

Results and Discussion

The proposed framework is applied on the WHU building data set, and the corresponding evaluation statistics are listed in Table 2. Moreover, to provide a more direct comparison, the published state-of-the-art performances obtained by one-shot networks are listed in Table 2 as well. In terms of the WHU

Table 2. Evaluation statistics (%) on WHU building data set.^a

Method	Precision	Recall	F1-Score	IOU
U-NET (Ji <i>et al.</i> 2019)	90.3	94.5	92.35	85.8
SegNet (Liu <i>et al.</i> 2019)	92.11	89.93	91.01	85.56
FCN-8s (Ji <i>et al.</i> 2018)	89.2	95.3	92.15	85.4
SRI-NET (Liu <i>et al.</i> 2019)	95.21	93.28	94.23	89.09
SR-FCN (Ji <i>et al.</i> 2018)	94.4	93.9	93.25	88.9
MSegnet	96.45	92.44	94.40	89.40

FCN = fully convolutional network; IOU = intersection-over-union; MSegnet = modified semantic segmentation; SegNet = semantic segmentation; SR-FCN = xxxx; SRI-NET = xxxx; U-NET = xxxx; WHU = Wuhan University.

^aData in bold indicates best result.

building data set, the proposed MSegnet outperforms the three typical network structures, including U-Net, SegNet, and FCN-8s. According to the works in Ji *et al.* (2019), Liu *et al.* (2019), U-Net, and SegNet were used with the same network structure as proposed in the original research, respectively (Ronneberger *et al.* 2015; Badrinarayanan *et al.* 2017). MSegnet differs from typical network structures by adding multiple height-width ratio convolutions in the network design, which can be recognized as a kind of novel basic network module in image segmentation. From the comparisons of different network modules, we find that MSegnet outperforms the widely used U-Net, SegNet, and FCN-8s building detection modules by almost 4% in terms of IOU, 3.39% in F1-score, and 7.25% in precision. Moreover, it is apparent that the precision and recall of each widely used typical network module exhibit larger gaps compared to that of MSegnet, indicating that the latter performs in a more balanced manner by distinguishing between buildings and background objects, despite different pixel distributions.

SRI-NET (Liu *et al.* 2019) and SR-FCN (Ji *et al.* 2018) are modified from the typical network modules SegNet and FCN, respectively, and their performances have achieved remarkable improvements. SRI-NET has achieved the state-of-the-art performance in terms of the F1-score and IOU evaluations among the published results. Nevertheless, our proposed MSegnet obtains 1.24% higher precision than SRI-NET, and 0.74% lower recall. The synthesized evaluation statistics F1-score and IOU of MSegnet are both slightly higher than SRI-NET by 0.17% and 0.31%, respectively. Apart from the recall, MSegnet achieves the best performance among all models listed in Table 2. This further validates the strong ability of the matrix convolution module in capturing features for multi-scale and multi-shape building detection.

To analyze detection errors, we selected four test images with typical detection errors and presented the corresponding original, ground truth, and detection result images in Figure 4. From the visual comparisons in the WHU building data set, we recognize that the proposed MSegnet accurately detects most buildings. The morphological characteristics are maintained; however, several small buildings are omitted, as shown in the green circles in column (b) of Figure 4. Apart from the omitted buildings, there are some open squares in the background with similar spectral and textural characteristics as buildings. These are misidentified as buildings in the detection results and marked in yellow circles in column (c) of Figure 4. This occurrence is attributed to the lower number of small buildings in the training data set than large ones, making the trained model more likely to focus on the detection of large buildings. Therefore, we may use the strategy of oversampling in future studies, as performed in the small objects detection (Kisantal *et al.* 2019). Generally, this experiment demonstrates the strong applicability potential of the matrix convolution module for building detection by learning features in multiple scales and aspect ratios.

Conclusions

An end-to-end semantic segmentation framework, MSegnet is proposed. It is composed of two main modules: backbone feature encoding and matrix layer convolution. The matrix layer convolution module captures features at multiple scales and aspect ratios by conducting a matrix of convolution operations on the encoded feature maps from the backbone with stripes of size 1×2 and 2×1 . The generated feature maps at different scales and aspect ratios are upsampled and concatenated through matrix feature learning for further pixel-wise label prediction. MSegnet is applied to a widely used public building detection data set for evaluation and demonstrates a

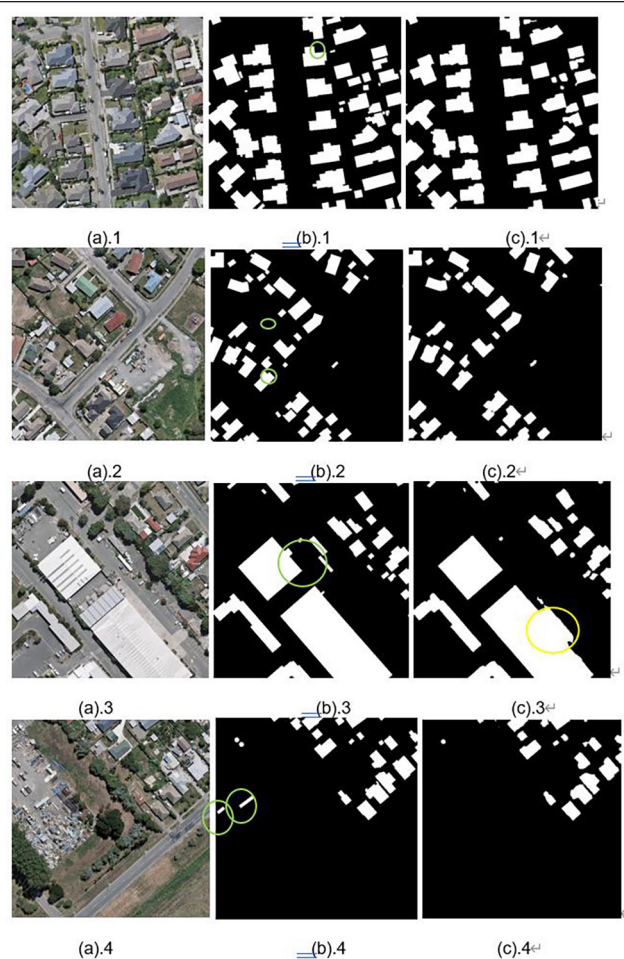


Figure 4. Building detection visualization of typical test samples in WHU building data set: (a) original test samples; (b) ground truth images; (c) detection results of our proposed MSegnet.

1.7% higher F1-score and 0.31% higher IOU compared to the state-of-the-art performance of published one-shot semantic segmentation models, as far as the authors are aware. The experiment confirms the strong potential applicability and robustness of our proposed framework in detecting objects of interest in practical cases. However, there is significant room for improvement of the proposed network in our future work, particularly regarding the detection of small buildings by adopting strategies such as oversampling.

Acknowledgments

The research was financially supported by the National Key R&D Program of China (No. 2019YFD1100803).

The authors declare that there is no conflict of interest regarding the publication of this paper.

Code, Data, and Materials Availability:

The WHU building data set can be accessed from <http://gpcv.whu.edu.cn/data/>.

The implementation code of our manuscript is provided at <https://github.com/yubozuzu123/MatrixSegnet>.

References

- Alshehhi, R., P.R. Marpu, W.L. Woon and M.D. Mura. 2017. Simultaneous extraction of roads and buildings in remote sensing imagery with convolutional neural networks. *ISPRS Journal of Photogrammetry and Remote Sensing* 130:139–149.
- Badrinarayanan, V., A. Kendall and R. Cipolla. 2017. SegNet: A deep convolutional encoder-decoder architecture for image segmentation. *IEEE Transactions on Pattern Analysis and Machine Intelligence* 39(12):2481–2495.
- Boonpook, W., Y. Tan, Y. Ye, P. Torteeka, K. Torsri and S. Dong. 2018. A deep learning approach on building detection from unmanned aerial vehicle-based images in riverbank monitoring. *Sensors*, 18(11):3921.
- Breiman, L. 2001. Random forests. *Machine Learning* 45(1):5–32.
- Burges, C.J.C. 1998. A tutorial on support vector machines for pattern recognition. *Data Mining and Knowledge Discovery* 2(2):121–167.
- Cetin, M., U. Halici and O. Aytekin. 2010. Building detection in satellite images by textural features and Adaboost. Pages 1–4 in *Proceedings 2010 IAPR Workshop on Pattern Recognition in Remote Sensing*, held in Istanbul, Turkey, 22 August 2010.
- Chen, L.-C., Y. Zhu, G. Papandreou, F. Schroff and H. Adam. 2018. Encoder-decoder with Atrous separable convolution for semantic image segmentation. In *Computer Vision—ECCV 2018. Lecture Notes in Computer Science*, vol. 11211, edited by V. Ferrari, M. Hebert, C. Sminchisescu, and Y. Weiss, 833–851. Cham, Switzerland: Springer.
- Chen, Q., L. Wang, S.L. Waslander and X. Liu. 2020. An end-to-end shape modeling framework for vectorized building outline generation from aerial images. *ISPRS Journal of Photogrammetry and Remote Sensing* 170:114–126.
- Dalal, N. and B. Triggs. 2005. Histograms of oriented gradients for human detection. Pages 886–893 in *Proceedings of the IEEE Computer Society Conference on Computer Vision and Pattern Recognition (CVPR'05)*, held in San Diego, Calif., 20–25 June 2005.
- Fleyeh, H. and E. Davami. 2013. Multiclass Adaboost based on an ensemble of binary Adaboosts. *American Journal of Intelligent Systems* 3:57–70.
- Golovanov, S., R. Kurbanov, A. Artamonov, A. Davydov and S. Nikolenko. 2018. Building detection from satellite imagery using a composite loss function. Pages 219–2193 in *Proceedings IEEE/CVF Conference on Computer Vision and Pattern Recognition Workshops*, held in Salt Lake City, Utah, 18–22 June 2018.
- Gomez, W., W.C. Pereira and A.F. Infantosi. 2012. Analysis of co-occurrence texture statistics as a function of gray-level quantization for classifying breast ultrasound. *IEEE Transactions on Medical Imaging*, 31(10):1889–1899.
- Guf, J.S. and W.S. Jiang. 1996. The Haar wavelets operational matrix of integration. *International Journal of Systems Science* 27(7):623–628.
- Hamaguchi, R. and S. Hikosaka. 2018. Building detection from satellite imagery using ensemble of size-specific detectors. Pages 223–2234 in *Proceedings of the IEEE/CVF Conference on Computer Vision & Pattern Recognition Workshops*, held in Salt Lake City, Utah, 18–22 June 2018.
- Hänsch, R. and O. Hellwich. 2010. Random forests for building detection in polarimetric SAR data. Pages 460–463 in *Proceedings of the IEEE International Geoscience and Remote Sensing Symposium*, held in Honolulu, Hawaii, 25–30 July 2010.
- He, K. and J. Sun. 2015. Convolutional neural networks at constrained time cost. Pages 5353–5360 in *Proceedings of the IEEE Conference on Computer Vision and Pattern Recognition (CVPR)*, held in Boston, Mass., 7–12 June 2015.
- He, K., X. Zhang, S. Ren and J. Sun. 2016. Deep residual learning for image recognition. Pages 770–778 in *Proceedings of the IEEE Conference on Computer Vision and Pattern Recognition (CVPR)*, held in Las Vegas, Nev., 27–30 June 2016.
- Ji, S., S. Wei and M. Lu. 2018. A scale robust convolutional neural network for automatic building extraction from aerial and satellite imagery. *International Journal of Remote Sensing* 40(1). <https://doi.org/10.1080/01431161.2018.1528024>.
- Ji, S., S. Wei and M. Lu. 2019. Fully convolutional networks for multisource building extraction from an open aerial and satellite imagery data set. *IEEE Transactions on Geoscience and Remote Sensing* 57(1):574–586.
- Khoshelham, K., S. Nedkova and C. Nardinocchi. 2008. A comparison of Bayesian and evidence-based fusion methods for automated building detection in aerial data. *The International Archives of the Photogrammetry, Remote Sensing and Spatial Information Sciences* 37(B7). https://www.isprs.org/proceedings/xxxvii/congress/7_pdf/6_wg-vii-6/24.pdf.
- Kim, K.S., D. Zhang, M.C. Kang and S.J. Ko. 2013. Improved simple linear iterative clustering superpixels. Pages 259–260 in *Proceedings of the IEEE International Symposium on Consumer Electronics*. <https://doi.org/10.1109/ISCE.2013.6570216>.
- Kingma, D. and J. Ba. 2014. Adam: A method for stochastic optimization. In *Proceedings 3rd International Conference on Learning Representations*, held in San Diego, Calif.
- Kisantal, M., Z. Wojna, J. Murawski, J. Naruniec and K. Cho. 2019. Augmentation for small object detection. arXiv:1902.07296.
- Konstantinidis, D., T. Stathaki, V. Argyriou and N. Grammalidis. 2017. Building detection using enhanced HOG–LBP features and region refinement processes. *IEEE Journal of Selected Topics in Applied Earth Observations and Remote Sensing* 10(3):888–905.
- Lafferty, J., A. McCallum and F. Pereira. 2002. Conditional random fields: Probabilistic models for segmenting and labeling sequence data. Pages 282–289 in *Proceedings of the Eighteenth International Conference on Machine Learning*, held in Williamstown, Mass., 28 June–1 July 2001.
- Lee, D.S., J. Shan and J.S. Bethel. 2003. Class-guided building extraction from Ikonos imagery. *Photogrammetric Engineering & Remote Sensing* 69(2):143–150.
- Li, P., B. Song and H. Xu. 2011. Urban building damage detection from very high resolution imagery by one-class SVM and shadow information. Pages 1409–1412 in *Proceedings of the IEEE International Geoscience and Remote Sensing Symposium*, held in Vancouver, Canada, 24–29 July 2011.
- Li, W., C. He, J. Fang and H. Fu. 2018. Semantic segmentation based building extraction method using multi-source GIS map datasets and satellite imagery. Pages 233–2333 in *Proceedings of the IEEE/CVF Conference on Computer Vision and Pattern Recognition Workshops (CVPRW)*, held in Salt Lake City, Utah, 18–22 June 2018.
- Lin, J., W. Jing, H. Song and G. Chen. 2019. ESFNet: Efficient network for building extraction from high-resolution aerial images. *IEEE Access*, 7:54285–54294.
- Lin, T.-Y., M. Maire, S. Belongie, J. Hays, P. Perona, D. Ramanan, P. Dollár and C.L. Zitnick. 2014. Microsoft COCO: Common objects in context. Pages 740–755 in *Proceedings of the Computer Vision (ECCV 2014)*, held in Zurich, Switzerland, 6–12 September 2014.
- Lin, T., P. Goyal, R. Girshick, K. He and P. Dollár. 2020. Focal loss for dense object detection. *IEEE Transactions on Pattern Analysis and Machine Intelligence* 42(2):318–327.
- Liu, P., X. Liu, M. Liu, Q. Shi, J. Yang, X. Xu and Y. Zhang. 2019. Building footprint extraction from high-resolution images via spatial residual inception convolutional neural network. *Remote Sensing* 11(7). <https://doi.org/10.3390/rs11070830>.
- Liu, Y., L. Gross, Z. Li, X. Li, X. Fan and W. Qi. 2019. Automatic building extraction on high-resolution remote sensing imagery using deep convolutional encoder-decoder with spatial pyramid pooling. *IEEE Access* 7:128774–128786.
- Lowe, D.G. 2004. Distinctive image features from scale-invariant keypoints. *International Journal of Computer Vision* 60(2):91–110.
- Mayer, H. 1999. Automatic object extraction from aerial imagery—A survey focusing on buildings. *Computer Vision and Image Understanding* 74(2):138–149.
- Nair, V. and G.E. Hinton. 2010. Rectified linear units improve restricted boltzmann machines. Pages 807–814 in *Proceedings of the 27th International Conference on International Conference on Machine Learning*, held in Haifa, Israel, 21 June 2010.

- Ning, W., C. Fang, Y. Bo and Q. Yuchu. 2020. Segmentation of large-scale remotely sensed images on a Spark platform: A strategy for handling massive image tiles with the MapReduce model. *ISPRS Journal of Photogrammetry and Remote Sensing* 162:137–147.
- Ning, X. and X. Lin. 2017. An index based on joint density of corners and line segments for built-up area detection from high resolution satellite imagery. *ISPRS International Journal of Geo-Information* 6(11):338.
- Noh, H., S. Hong and B. Han. 2015. Learning deconvolution network for semantic segmentation. Pages 1520–1528 in *Proceedings of the IEEE International Conference on Computer Vision (ICCV)*, held in Las Condes, Chile, 7–13 December 2015.
- Ojala, T., M. Pietikainen and T. Maenpaa. 2002. Multiresolution gray-scale and rotation invariant texture classification with local binary patterns. *IEEE Transactions on Pattern Analysis and Machine Intelligence* 24(7):971–987.
- Peng, S., W. Jiang, H. Pi, X. Li, H. Bao and X. Zhou. 2020. Deep snake for real-time instance segmentation. https://openaccess.thecvf.com/content_CVPR_2020/papers/Peng_Deep_Snake_for_Real-Time_Instance_Segmentation_CVPR_2020_paper.pdf
- Qin, H., Y. Li, J. Lei, W. Xie and Z. Wang. 2020. A specially optimized one-stage network for object detection in remote sensing images. *IEEE Geoscience and Remote Sensing Letters*:1–5.
- Rashwan, A., A. Kalra and P. Poupart. 2019. Matrix nets: A new deep architecture for object detection. Pages 2025–2028 in *Proceedings of the IEEE/CVF International Conference on Computer Vision Workshop (ICCVW)*, held in Seoul, South Korea, 27–28 October 2019.
- Ronneberger, O., P. Fischer and T. Brox. 2015. U-Net: Convolutional networks for biomedical image segmentation. Pages 234–241 in *Proceedings International Conference on Medical Image Computing and Computer-Assisted Intervention, Lecture Notes in Computer Science*, vol. 9351. https://doi.org/10.1007/978-3-319-24574-4_28
- Shelhamer, E., J. Long and T. Darrell. 2017. Fully convolutional networks for semantic segmentation. *IEEE Transactions on Pattern Analysis and Machine Intelligence* 39:640–651.
- Walde, I., S. Hese, C. Berger and C. Schmullius. 2013. Graph-based mapping of urban structure types from high-resolution satellite image objects—Case study of the German cities Rostock and Erfurt. *IEEE Geoscience & Remote Sensing Letters* 10(4):932–936.
- Wang, S., X. Hou and X. Zhao. 2020. Automatic building extraction from high-resolution aerial imagery via fully convolutional encoder-decoder network with non-local block. *IEEE Access* 8:7313–7322.
- Yu, B., L. Yang and F. Chen. 2018. Semantic segmentation for high spatial resolution remote sensing images based on convolution neural network and pyramid pooling module. *IEEE Journal of Selected Topics in Applied Earth Observations and Remote Sensing* 11(9):3252–3261.
- Yurtkulu, S.C., Y.H. ahin and G. Unal. 2019. Semantic segmentation with extended DeepLabv3 architecture. Pages 1–4 in *Proceedings of the 27th Signal Processing and Communications Applications Conference (SIU)*. <https://doi.org/10.1109/SIU.2019.8806244>.
- Zhao, H., J. Shi, X. Qi, X. Wang and J. Jia. 2017. Pyramid scene parsing network. Pages 6230–6239 in *Proceedings 2017 IEEE Conference on Computer Vision and Pattern Recognition (CVPR)*, held in Honolulu, Hawaii, 21–26 July 2017.
- Zhao, K., J. Kang, J. Jung and G. Sohn. 2018. Building extraction from satellite images using mask R-CNN with building boundary regularization. *Proceedings of the IEEE/CVF Conference on Computer Vision and Pattern Recognition Workshops (CVPRW)*, held in Salt Lake City, Utah, 18–22 June 2018.

Estimation of Rock Characteristics Based on Polarization Spectra: Surface Roughness, Composition, and Density

Feizhou Zhang, Xufang Liu, Yun Xiang, Zihan Zhang, Siyuan Liu, and Lei Yan

Abstract

Surface polarization characteristics provide crucial structural information of the Earth's surface. As two key elements of the natural geographical environment, rocks and soils play an important role in the study of surface processes. Inherent surface characteristics, such as surface roughness, composition, and density are critical parameters for the remote monitoring of land surfaces as they affect the polarization characteristics of scattered light waves. In this study, we investigated the relationship between surface roughness, composition, and density, and the polarization spectra of limestone-dolomite series rock. Results reveal a power function relationship between the surface roughness and the degree of polarization peaks among different detection zenith and azimuth angles. The depth and position of the absorbing waveband are significantly correlated with the characteristic component contents. The rock density was determined via the polarized reflection spectra, with the Earth's surface density calculations associated with a 2.6% divergence from the current recognized data. Our results demonstrate the ability of polarized spectra to retrieve surface roughness, composition, and density, with potential for further development in future work.

Introduction

The surfaces of natural objects range between an ideal mirror surface and an ideal Lambertian surface. The roughness, texture structure, chemical composition, moisture content, and other physical and chemical characteristics of the surface affect the polarization characteristics of light scattered onto the surface. Surface roughness is a key influencing factor for numerous land surface processes, and as a result, an extensive amount of surface parameter characterization and measurement techniques have been developed (Jiang *et al.* 2012). For example, Su *et al.* (2016) considered the refractive index, extinction coefficient, and roughness in a polarization characteristic model, using the measured degree of polarization (DOP) to invert these three parameters for green paint coating and quartz glass. Kang *et al.* (2013) used a surface bidirectional reflection geometric optical model to invert soil surface roughness, with optical multi-angle observation information as the input. Ling *et al.* (2016) integrated the different

polarized reflection characteristics of rough object surfaces under different light bands into a polarization spectra bidirectional reflection distribution function (BRDF) model based on Kirchhof theory, and subsequently conducted simulation and comparison experiments under varying conditions. In Lv and Zhao (2015), the bidirectional reflection spectra information of the flat and rough sand formed via wind erosion simulations were fused with a BRDF model to invert the roughness characteristics. The aforementioned studies have made great advancements in the application of the polarized spectra to invert the surface roughness. Furthermore, Zhao *et al.* (2004a; 2004b; 2004c; 2003) added to this progress by measuring the multi-angle polarized spectra of different rock and soil types.

As two of the most important elements of the natural environment, rock and soil are crucial for the study of surface processes. Previous literature has generally focused on the characteristics of the polarized rock mineral and soil spectra in the 2π hemisphere, while studies on the relationships between polarization and the physical properties of rock minerals and soil are lacking. However, determining the relationship between the surface roughness, composition, and density of mineral rocks from the polarized spectra of rocks and soil is a promising technique with an important role in promoting the basic application of remote sensing. In the current study, we analyzed the relationship between the polarization spectra of rock and the three key physicochemical properties of rocks (i.e., surface roughness, rock composition, and surface density) in order to estimate the density of various rock minerals and the Earth.

Measuring Instrument

Multi-angle spectra measurement and polarization spectra measurement are conducted by a multi-angle measurement device. Figure 1 presents the multi-angle measurement device, including three parts: incident light source, rotating platform, and detection frame. By adjusting the light source, the incident angle is able to change from 0° – 90° and the accuracy is within 0.5° . The objective table was fixed, and the sample was placed on the center of the whole multi-angle measurement device. The rotating platform and the detection frame are precisely controlled by the driving motor to change the detection azimuth and zenith angle, and the angle accuracy is within 0.1° .

In our study, this device was used to measure the optical spectra and polarization spectra in the azimuth angle from 0° to 360° and zenith angle from -90° to 90° . For measurement of intensity or polarization reflected from the samples, Analytical Spectral Devices, Inc. (ASD) FieldSpec3 spectrometer was used to measure the hyper-spectra from 350 nm to

Feizhou Zhang, Xufang Liu, Zihan Zhang, Siyuan Liu, and Lei Yan are with the Institute of Remote Sensing and Geographic Information System, School of Earth and Space Science, Peking University, Beijing 100871, China.

Yun Xiang is with Hebei Institute of Meteorological Sciences, Shijiazhuang 050021, China.

Lei Yan is with Key Laboratory of UAV Telemetry, Guilin Institute of Aerospace Technology, Guilin 541004, China..

Contributed by Alper Yilmaz, April 6, 2021 (sent for review June 1, 2021; reviewed by Bin Yang, Wei Chen).

Photogrammetric Engineering & Remote Sensing
Vol. 87, No. 12, December 2021, pp. 907–912.
0099-1112/21/907–912

© 2021 American Society for Photogrammetry
and Remote Sensing
doi: 10.14358/PERS.21-00014R2

2500 nm and a broadband spectrometer EWA-700 was used to measure the broadband spectral response from 760 nm to 1100 nm. The spectrometer was equipped with a polarizing prism. When the polarizing prism is installed in front of the spectrometer probe, it can be used for multi angle polarization spectra measurement.

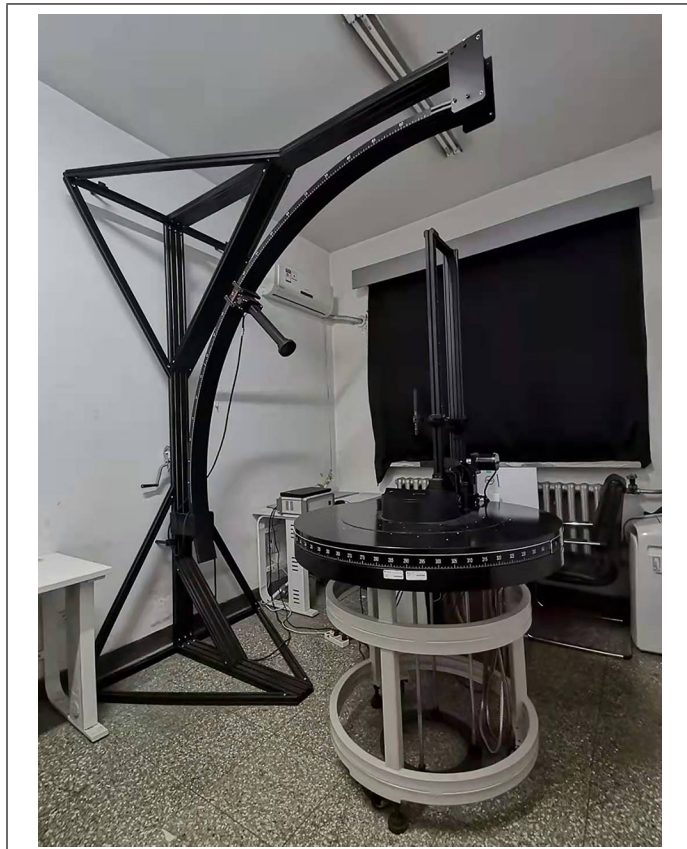


Figure 1. The indoor large multi-angle measurement device.

The Influence of Surface Roughness on Polarization Spectra

Principles and Research Methods

The definition of rock surface roughness is related to the incident zenith angle of light. According to the Rayleigh criterion, namely, $\sigma < \lambda/8\cos\theta$, the smaller the incident angle, the smoother the rock surface and vice versa. For example, at 1100 nm, the surface is considered smooth only if $\sigma < 137.5$ nm for an incident angle of 0° . However, the rock surface can also be considered as smooth for $\sigma < 275$ nm and an incident angle of 60° . Thus, as the incidence angle increases, the smooth surface degree of the same roughness varies with incidence angle. More specifically, rough surfaces become smoother with for an increasing incident angle.

For example, when basalt is cut and polished into a smooth sample, the reflection intensity of different wavebands at different incident and reflection angles can be quantified by a bidirectional reflectance photometer (Zhao *et al.* 2003), with the electrical current (in milliamper, i.e., mA) directly measured by the photoelectric conversion device inside the instrument.

The samples used in this experiment is basalt and biotite plagioclase gneiss. Basalt is a fine-grained extrusive igneous rock formed from the rapid cooling of low-viscosity lava rich in magnesium and iron exposed at or very near the surface of a rocky planet or a moon. Biotite plagioclase gneiss is a common and widely distributed type of metamorphic rock. The rock is dark green with uniform structure and hard texture.

Results and Analysis

Effect of Different Rock Surface Roughness on Intensity

Figure 2a–f presents the spectra curves of basalt in the 2π detection space within the incident zenith angle range of 10° – 60° and the 760–1100 nm spectral region. The reflection spectra of basalt in the 2π space are observed to shift from Lambertian to specular reflection with the increase of the incident zenith angle. This is attributed to the Rayleigh criterion, whereby the rock surface is always considered to be rough for small incidence angles. For larger incidence angles, the surface of the rock gradually becomes smooth, and specular reflection is observed, with the specular reflection becoming stronger for increasing incident zenith angles.

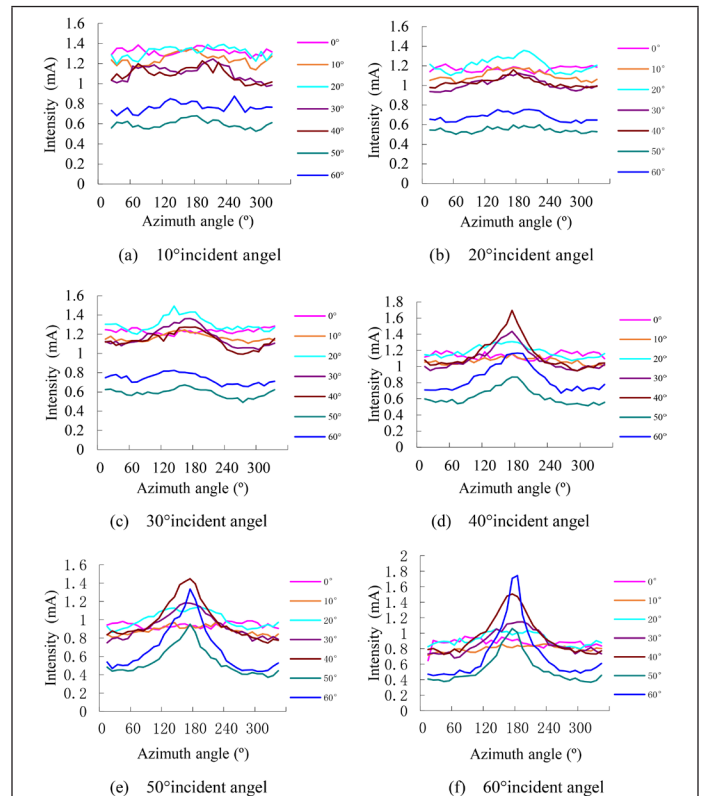


Figure 2. Spectra of different observing zenith angle of basalt without polarizer on the 760–1100 nm band, with varying incident angles. (The x-axis represents the relative observation azimuth angle, taking the azimuth of the incident light as a reference, which varies from 0° – 360° . The y-axis is the reflection intensity spectra of the rock.)

Effects of Different Rock Surface Roughness on DOP

Testing was performed on a piece of biotite plagioclase gneiss that was divided into five pieces (h1–h5). The surface was polished to five gradients with different abrasives, and the surface roughness can be measured via a needle-tracing surface-roughness-meter (Xiang *et al.* 2011). The arithmetical mean deviations of the profile (Ra) were $4.08 \mu\text{m}$, $2.91 \mu\text{m}$, $1.47 \mu\text{m}$, $0.86 \mu\text{m}$, and $0.33 \mu\text{m}$, for h1–h5, respectively. We then evaluated the influence of the surface roughness factor on the zenith angles and azimuth DOP of the rock within 350–2500 nm. For a fixed incident zenith angle and varying rock surface roughness, the DOP was observed to vary with the detection zenith and azimuth angles of specular reflection (180° relative detection azimuth angle). More specifically, the DOP initially increased to its maximum value and subsequently declined. At the observation zenith angle corresponding to the incident zenith angle, the DOP reached a maximum at 180° , and subsequently decreased

gradually with a distance of 180° from the observation azimuth on both sides, ultimately tending to zero.

Rocks with different surface roughness have different peaks and corresponding angles in spectra. The appearance and value of the specular reflection peak are a function of the surface roughness. The smaller the surface roughness, the smoother the rock, the higher the specular reflection peak, and the closer the distance between the appearance and specular reflection angles and vice versa.

The nonmirror peak phenomenon assumes that the surface roughness is greater than or equal to the light wave wavelength ($\delta < \lambda \leq 1$) (Ourlier *et al.* 2001; Torrance and Sparrow 1967). According to this criterion, at 520 nm, h1–h4 should produce nonspecular peaks, while the polished h5 rocks should produce specular peaks. This is consistent with our observations.

The characteristic band at 520 nm \pm 10 nm (dark green rock, corresponding to the green absorption band) was selected to perform correlation analysis between the peak value of the DOP along the observation zenith angle and the surface roughness. Results reveal a power function relationship ($y = 0.604x^{0.297}$, $R^2 = 0.9854$) between the two variables. Moreover, at the observation azimuth angle of 180°, a power function relationship was also observed between the surface roughness and the DOP peak and surface roughness ($y = 0.5822x^{-0.333}$, $R^2 = 0.9843$). F tests for these regression models demonstrate the significant correlation between the DOP peak and the surface roughness.

Correlation Between Rock Composition and DOP

Sampling and Experimental Method

Selection and Preparation of Rock Samples

The experimental samples comprised two carbonate rock types, namely limestone and dolomite. These samples were used to investigate the relationship between the polarized spectra and the chemical compositions of rocks in the visible to near infrared bands. The main components to exhibit variations were Ca^{2+} and Mg^{2+} . The limestone and dolomite rock samples included four rock rocks, namely oolitic limestone, dolomite limestone, calcite dolomite, and dolomite, denoted as D1\D2\D3\D4, respectively. The principal components of limestone and dolomite are CaCO_3 and $\text{CaMg}(\text{CO}_3)_2$, respectively. The surfaces of the four rock samples were cut into planes and ground with a 120# emery abrasive. The processing time of each sample was consistent. Following the processing, hyperspectral and polarized spectra were measured. A small sample with a surface area consistent to that where their spectral measurements were conducted was select for further analysis in the laboratory. In particular, the specific components of the sample were measured using a sequential X-ray fluorescence spectrometer (<1% primary component analyses error). X-ray fluorescence spectroscopy is a widely used method for rock composition detection. Measurements were conducted by Hebei Comprehensive Geological Brigade. Table 1 reports the key components determined from the measurements.

Note, loss on ignition (LOI) is the amount of burning loss. After measuring the amount of burning loss of samples, the mass percentage of the main metal oxides in the carbonate rocks was determined via X-ray fluorescence spectrometry.

The contents of Ca^{2+} and Mg^{2+} appear to vary across the rock samples. In particular, the content of Ca^{2+} and Mg^{2+} is observed to be similar for oolitic limestone and dolomite, while calcareous dolomite and dolomite exhibit (nonsignificant) differences.

Rock Spectra

Figure 3 depicts the spectra measured for each sample. The reflectivity of the dolomite rock samples is higher than that of the limestone rock samples. The spectra of the two limestone samples are almost equal, with the exception of the 350–1050 nm spectral region. In addition, the reflectivity of the samples is correlated with the variations in Ca^{2+} and Mg^{2+} observed in Table 1. More specifically, the Ca^{2+} and Mg^{2+} content in oolitic and dolomite limestone is relatively consistent, yielding similar spectra, while the Ca^{2+} content in dolomite and calcareous dolomite is lower than that in limestone, and the content of Mg^{2+} is higher than that in limestone, leading to higher spectral values.

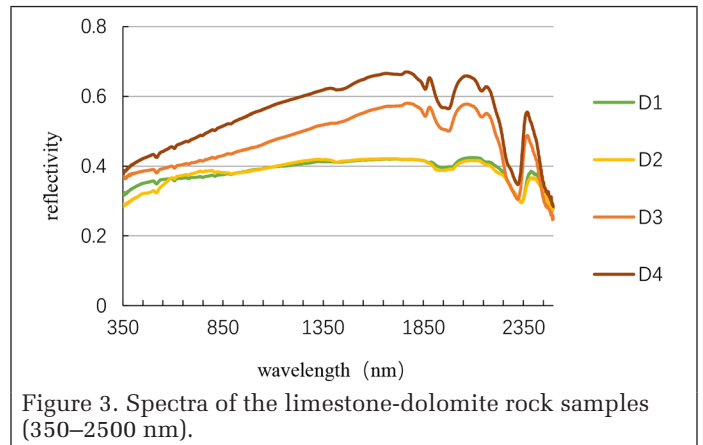


Figure 3. Spectra of the limestone-dolomite rock samples (350–2500 nm).

Figure 4 presents the spectral values at the nonfeature absorption bands of 950 nm, 1550 nm, 2050 nm, and 2350 nm. The dolomitic limestone surface exhibits a red area, while the surface of the other three rocks is uniform in color (gray or gray-white). This red area corresponds to the Fe_2O_3 content (0.33%) of dolomitic limestone, which is significantly higher than that of the other three rocks (0.05%) (Table 1). Furthermore, the dolomitic limestone exhibits a steeper drop to the blue-band direction compared to the other three samples, while a wider absorption band is identified around 870 nm. These observations can be attributed to Fe^{3+} (Yan *et al.* 2003).

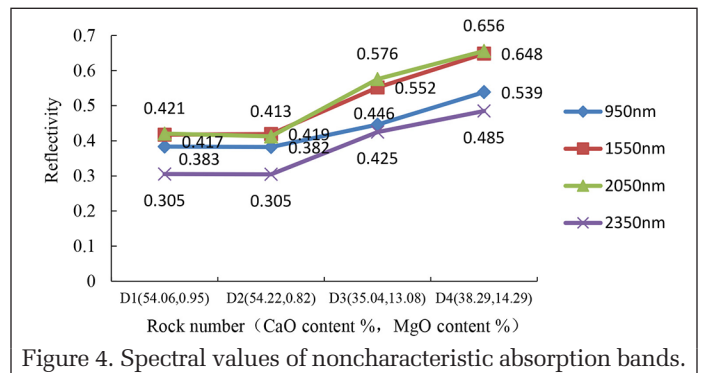


Figure 4. Spectral values of noncharacteristic absorption bands.

Table 1. Components of the limestone-dolomite rock samples (%).

Rock	SiO_2	Al_2O_3	Fe_2O_3	CaO	MgO	K_2O	Na_2O	MnO_2	TiO_2	P_2O_5	LOI
Oolitic limestone D1	0.680	0.240	0.050	54.060	0.950	0.040	<0.010	<0.001	0.008	0.152	43.720
Dolomite limestone D2	1.910	0.580	0.330	54.220	0.820	0.180	0.050	0.007	0.024	0.199	41.720
Calcite dolomite D3	0.950	0.140	0.050	35.040	13.080	0.010	<0.010	0.006	<0.001	0.193	46.240
Dolomite D4	0.560	0.110	0.050	38.290	14.290	0.010	<0.010	0.006	0.002	0.217	46.550

LOI = loss on ignition.

The characteristic absorption regions of the four rocks can be summarized as follows: 520 nm, 1400 nm, 1860 nm, 1900–2050 nm, 2130 nm, and 2300–2350 nm (Table 2). The absorption bands appearing after 1.3 μm are caused by vibrations and are the double or combined frequency of water or carbonate ion itself. Note that while water is rare in carbonates, Figure 3 presents a very shallow water absorption band at 1400 nm. Common absorption bands are typically located within 1.6–2.5 μm . Hunt and Salisbury (1970) attributed these bands to the doubling and merging of the internal vibrations of the CO_3^{2-} group, or the interaction of these groups with the lattice vibrations.

Table 2. Four commonly characterized bands.

	Band I (μm)	Band II (μm)	Band III (μm)	Band IV (μm)
Calcite	1.88	2.0	2.16	2.35
Colomite	1.86 or 1.87	1.99	2.14 or 2.16	2.33 or 2.34

Chen *et al.* (1998) demonstrated that for the Keping area of Xinjiang, China, absorption peaks of dolomite and limestone were significantly different at 2.35 μm , while the strong absorption peak of dolomite was in the short-wave band region, 10 nm away from that of limestone. This band is also the strongest characteristic absorption band across the whole spectra and thus 2300–2350 nm is selected for subsequent analysis.

Analysis of the Relationship Between DOP Spectra and Composition

Figure 5 presents the DOP of the limestone and dolomite rock samples. Due to the use of a polarization prism, the detected light intensity is reduced, and the DOP is calculated using 90° and 0° polarization spectra, which increases the noise of the polarization results. The peaks and troughs of the spectra correspond to the hyperspectral measurement noise, rather than the absorption features of the samples. Thus, we used a moving average to reduce the noise. Spectral envelope elimination (Xu *et al.* 2005; Clark 1983) can effectively remove baseline influences to determine standard curves that reflect the properties of the surface feature absorption peaks. We therefore used this method to extract the effective characteristic bands. The lower envelopes of the spectra in Figure 5 ($\text{DOP}_{\text{down}_c}$) were determined and subsequently divided by the original DOPs to obtain the spectra in Figure 6. Table 3 reports the valley depth and corresponding wavelength locations of the absorption bands within the range 2300–2350 nm. We then determined the correlation of the valley depth and wavelength location with the CaO and MgO contents (Table 4).

Table 3. Position and depth of the DOP characteristic band following continuum removal.

Rock Sample	Wavelength (nm)	Valley Depth (x)
D1	2344	0.350183
D2	2334	0.264137
D3	2323	0.578864
D4	2321	0.603101

DOP = degree of polarization.

Table 4. Correlation coefficient (r) between the contents of the two target compounds and the position and depth of the DOP characteristic band following continuum removal.

	Valley Depth (x)	Wavelength (nm)
CaO Content	-0.96139*	0.900281*
MgO Content	0.979317*	-0.92089*

*Indicates the correlation coefficient is significant at 0.05 level.

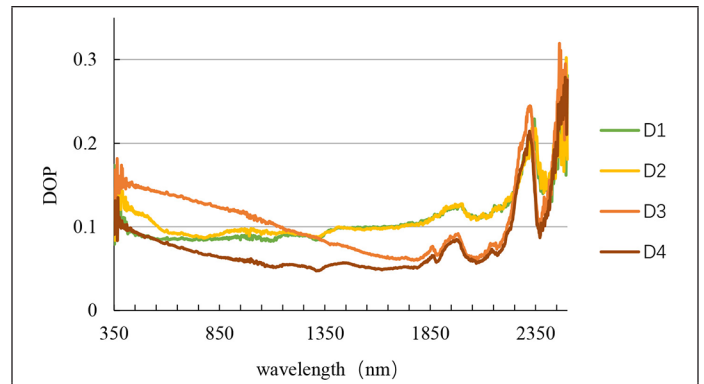


Figure 5. Degree of the polarization (DOP) of the limestone-dolomite rock samples.

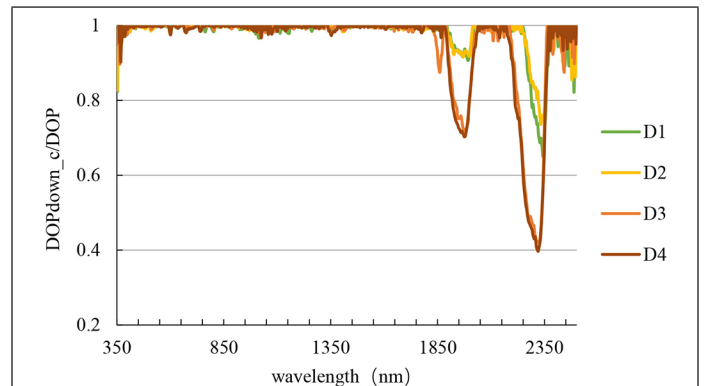


Figure 6. Degree of polarization (DOP) of limestone-dolomite rock samples after continuum removal.

The correlation between valley depth and CaO (MgO) content is greater than the critical correlation coefficient value of $\gamma_{0.05,2} = 0.950$, indicating that the regression model is significant at the 0.05 level. In addition, the correlation between the wavelength and CaO (MgO) is greater than the critical correlation coefficient value of $\gamma_{0.10,2} = 0.900$, indicating that the regression model is significant at the 0.10 level. These results demonstrate that there exists a relationship between the contents of CaO and MgO and the DOP peak value and corresponding wavelength. The DOP peak value within the 2300–2350 nm band increases with CaO and MgO content, and the more the wavelength corresponding to the peak tends to short wavebands. This is consistent with the results from the hyperspectral analysis, with a distinction in that the characteristic bands are expressed as absorption troughs in the hyperspectral measurements and peaks in the DOP.

Inverting Land Surface Density Using DOP

The Density Theory of Land Surface Inversion

The surface density of an earth target can be calculated from the polarized reflection spectra of rock, soil, etc. The refractive index is obtained by the polarized reflection spectra and the density of the surface is determined via the refractive index.

The reflection spectra DOP of the rock surface can be determined as follows:

$$\text{DOP} = \frac{2\cos\alpha\cos\beta\sin\alpha\sin\beta}{\cos^2\alpha\cos^2\beta + \sin^2\alpha\sin^2\beta} = \frac{2}{\frac{1}{\tan\alpha\tan\beta} + \tan\alpha\tan\beta} \quad (1)$$

where α and β refer to the incidence zenith and refraction angles, respectively.

We can apply the law of refraction to eliminate the refraction angle via the refractive index, N , of the rock:

$$\text{DOP} = \frac{2\cos\alpha \sqrt{1 - \frac{\sin^2\alpha}{N^2}} \sin\alpha \frac{\sin\alpha}{N}}{\cos^2\alpha \frac{N^2 - \sin^2\alpha}{N^2} + \sin^2\alpha \frac{\sin^2\alpha}{N^2}} = \frac{2\sin\alpha \text{tg}\alpha \sqrt{N^2 - \sin^2\alpha}}{N^2 - \sin^2\alpha + \sin^2\alpha \text{tg}^2\alpha} \quad (2)$$

N can be directly derived using the known incident angle and the DOP. The density of the rock can then be determined with the Lorentz-Lorenz refraction formula as follows:

$$\frac{N^2 - 1}{N^2 + 2} \times \frac{1}{\rho} = \text{constant} = \gamma_{LL} \quad (3)$$

where ρ is the density and the constant is typically set equal to 0.12. Equation 3 was derived in 1880 by Lorentz. The refraction index is theoretically measured at an infinite wavelength, yet in practice it is generally measured using yellow light. Equation 3 allows for the estimation of density at a given refraction index. Taking ordinary pyroxene as an example, $N = 1.713$ and thus the corresponding density is 3.330 g/cm^3 , lying in the range of $3.23\text{--}3.52 \text{ g/cm}^3$. Therefore, the refractive index can effectively estimate mineral density.

Results and Analysis

Rock Density Estimations

We used the theory proposed in the Section “The Density Theory of Land Surface Inversion” to calculate the refractive index and density of rocks. In order to verify the reliability of calculating rock density through the degree of polarization, we selected seven relatively common rock samples, mainly igneous rock. The density of rocks was calculated by degree of polarization and measured by geological measurements at the same time. Then, the errors of the two results were analyzed. Table 5 reports the estimated and measured primary mineral densities of seven rock types. There is a strong agreement between the DOP-based estimations and the measurements. The mean error is generally less than 10%, while that of gabbro reaches 20%. However, the mineral composition of rock is complex, and it is thus inaccurate to consider the rock as a single mineral. Further work is required in the future, such as improvements in the instrument and investigating the functional relationship between the DOP and rock density.

Estimation of the Earth’s Surface Density

We then proposed a method to determine the surface density of stars. By measuring the majority of the Earth’s rocks, the average specific refraction K of the total rocks and minerals on the Earth’s surface can be obtained (~ 0.21). Despite their varying refractive indices and densities, most of the Earth’s rock minerals have a K value close to 0.21. The specific refraction (K) values of SiO_2 , Al_2O_3 , MgO , Na_2O , K_2O , CaO , and P_2O_5 range between 0.20 and 0.23, while that of FeO is lower (0.188) and the Fe_2O_3 and H_2O (liquid) values are greater (0.290 and 0.340, respectively). These components are

synthesized into the rock minerals and the average K is taken as 0.21.

The average specific refraction of 0.21 represents the K level of the total rock mineral on the Earth’s surface. We integrate the Glaston-Dyer and Lorentz-Lorenz refraction formulas to obtain the following:

$$\frac{N - 1}{\rho} = K_{\text{earth}} = 0.21 \quad (4)$$

$$\frac{N^2 - 1}{N^2 + 2} \times \frac{1}{\rho} = \text{constant} = \gamma_{LL} = 0.12 \quad (5)$$

Combining Equations 4 and 5 results in the following equation:

$$4N^2 - 7N + 1 = 0 \quad (6)$$

and thus, we have:

$$N_1 = \frac{7 + \sqrt{33}}{8} \quad (7)$$

$$N_2 = \frac{7 - \sqrt{33}}{8} \quad (8)$$

N_2 is impossible as the refractive index of air is bigger than 1. N_1 can be substituted into Equation 4 as follows:

$$\rho = \frac{N - 1}{0.21} \approx 2.824 \text{ g/cm}^3 \quad (9)$$

This density estimation is in good agreement with the Earth’s surface density data reported Bullen and Bolt (1963) via a model of the Earth’s density depth distribution (2.824 g/cm^3 and 2.9 g/cm^3 , relative error = 2.6%). At depths less than 1000 m, the average density of the ellipsoid layer is taken as 2.9 g/cm^3 . The estimation of Bullen and Bolt (1963) was achieved by fitting the boundary conditions and all available observations, particularly those of the seismic discontinuity. These results demonstrate the feasibility of the Earth’s surface density estimations using the average K of the Earth. Moreover, K is also a reflection of the total rock on the Earth’s surface. Thus, estimating the surface density using the average K of stars is a reliable approach.

Conclusion and Outlook

In the current study, we investigated the relationship between surface roughness, composition, density, and the polarization spectra with rock as an example. Analysis of the rock surface roughness effect on the reflected polarized light demonstrates that the DOP peaks and surface roughness measured at different observation zenith angles and observation azimuths exhibit a significant power function relationship, with the regression model determination coefficient greater than 0.98. Furthermore, investigations of the relationship between rock

Table 5. Primary mineral densities calculated by polarization spectroscopy.

	Peridotite	Pyroxenite	Gabbro	Diorite	Quartz Porphyry	Syenite	Serpentinite
Density calculated by DOP (g/cm^3)	3.30–3.50	3.23–3.52	2.60–2.76	3.10–3.40	2.50–2.80	2.56–2.58	2.50–2.65
Density measured by geological measurements (g/cm^3)	3.27–3.48	3.02–3.45	3.02–3.45	2.50–3.30	—	2.50–3.30	~2.57
Mean error (%)	0.7	4.1	20.7	10.7	—	12.8	2.0

DOP = degree of polarization.

compositions and DOP reveal that the depth and wavelength position of characteristic absorption bands caused by rock compositions are significantly correlated with the content of the characteristic components. DOP is able to accurately estimate rock density, with an error of 2.6% determined for the Earth's surface density calculated by this method.

Results prove the feasibility of the inversion of surface structural parameters such as roughness, composition, and density via the application of polarization spectra. We demonstrate a new remote sensing approach that is an alternative for traditional optical techniques. The proposed method provides information of an additional dimension (i.e., polarization) in order to solve the ill-posed problems of surface parameter inversions using remote sensing methods. However, further work is required to perfect the inversion of these parameters.

Natural surfaces range between ideal mirror and ideal Lambert surfaces. The scattering characteristic is the superposition of the specular reflection and diffuse reflection components. The specular reflection proportion increases with the surface smoothness. We summarized the correlation between polarized light and surface roughness structural characteristics, providing a basis for further studies on the modeling, corresponding feasibility, and the potential applications.

We provided a correlation analysis of DOP and rock composition. However, the composition of rock is extremely complex and investigating the relationship between the characteristic bands and polarized intensity based on rock spectral libraries is reserved for future work.

When calculating the surface density, the measured DOP is the DOP on the rough surface, not the smooth surface of the rock. Thus, there is a discrepancy between the calculated and measured values. In addition, rocks typically have a higher DOP in the mirror direction compared to the other directions. Substituting the mean DOP values will reduce this difference.

Acknowledgments

This research was funded by the National Key Research and Development Program of China (grant number 2017YFB0503003, 2017YFB0503004).

References

- Bullen, K.E and B.A. Bolt. 1963. *An Introduction to the Theory of Seismology*. London: Cambridge University Press, 215–216.
- Chen, S.P., Q.X. Tong and H.D. Guo. 1998. *Mechanism of Remote Sensing Information*. Beijing, China: The Science Press, 159–162.
- Clark, R.N. 1983. Spectral properties of mixtures of montmorillonite and dark carbon grains: Implications for remote sensing minerals containing chemically and physically adsorbed water. *Journal of Geophysical Research* 88(12):10633–10635.
- Hunt, G.R. and J.W. Salisbury. 1970. Visible and near-infrared spectra of minerals and rocks: I silicate minerals. *Modern Geology* 5(1):283–300.
- Jiang C.Y., H.L. Fang and S.S. Wei. 2012. Review of land surface roughness parameterization study. *Advances in Earth Science* 27(3):292–303.
- Kang, Y.H., J.D. Wang, H.M. Zhou and Y. Liu. 2013. Soil surface roughness estimation using multiangular remote sensing observations: A preliminary study. *Journal of Remote Sensing* 17(1):180–192.
- Ling, J.J., G. Li, R.B. Zhang, Q. Tang and Q. Ye. 2016. Modeling and simulation of spectral polarimetric BRDF. *Spectroscopy and Spectral Analysis* 36(1):42–46.
- Lv, Y.F. and Y.S. Zhao. 2015. Study of retrieving the sandy surface roughness land based on the bidirectional reflectance model. *Spectroscopy and Spectral Analysis* 35(11):3123–3128.
- Ourlier, C., G. Berginc and J. Saillard. 2001. The theoretical study of the Kirchhoff integral from two-dimensional randomly rough surface with shadowing effect: Application to the backscattering coefficient for a perfectly-conducting surface. *Waves in Random Media* 11(1):91–118
- Su, Z.Q., C.X. Yan, J.Q. Zhang and B. Yang. 2016. Inversion of quartz glass and green paint based on polarization characters. *China Optics* 9(5):547–553.
- Torrance, K.E. and E.M. Sparrow. 1967. Theory for off-specular reflection from roughened surface. *Journal of the Optical Society of American* 57(9):1104–1105.
- Xiang, Y., L. Yan, Y.S. Zhao, Z.Y. Gou and W. Chen. 2011. Influence of surface roughness on degree of polarization of biotite plagioclase gneiss varying with viewing angle. *Spectroscopy and Spectral Analysis* 31(12):3423–3428.
- Xu, Y.J., G.D. Hu and Z.F. Zhang. 2005. Continuum removal and its application to the spectra classification of field object. *Geography and Geo-Information Science* 21(06):11–14.
- Yan, S.X., B. Zhang, Y.C. Zhao, L.F. Zheng, Q.X. Tong and K. Yang. 2003. Summarizing the VIS-NIR spectra of minerals and rocks. *Remote Sensing Technology and Application* 18(4):191–201.
- Zhao, H., L. Yan and Y.S. Zhao. 2003. Study on multi-angle polarized reflectance spectra of basalt. *Geography and Geo-Information Science* 19(4):81–83.
- Zhao, H., L. Yan and Y.S. Zhao. 2004a. Multi-angle polarized reflectance spectra of peridotite. *Geology and Prospecting* 40(2):51–54.
- Zhao, H., L. Yan and Y.S. Zhao. 2004b. Study on multi-angle polarized reflectance spectra of granite. *Journal of Mineralogy and Petrology* 24(2):9–13.
- Zhao, H., L. Yan and Y.S. Zhao. 2004c. Multi-angle polarized reflectance spectra of soil. *Acta Pedologica Sinica* 41(3):476–479.

Automatic Registration of Mobile Mapping System Lidar Points and Panoramic-Image Sequences by Relative Orientation Model

Ningning Zhu, Bisheng Yang, Zhen Dong, Chi Chen, Xia Huang, and Wen Xiao

Abstract

To register mobile mapping system (MMS) lidar points and panoramic-image sequences, a relative orientation model of panoramic images (PROM) is proposed. The PROM is suitable for cases in which attitude or orientation parameters are unknown in the panoramic-image sequence. First, feature points are extracted and matched from panoramic-image pairs using the SURF algorithm. Second, these matched feature points are used to solve the relative attitude parameters in the PROM. Then, combining the PROM with the absolute position and attitude parameters of the initial panoramic image, the MMS lidar points and panoramic-image sequence are registered. Finally, the registration accuracy of the PROM method is assessed using corresponding points manually selected from the MMS lidar points and panoramic-image sequence. The results show that three types of MMS data sources are registered accurately based on the proposed registration method. Our method transforms the registration of panoramic images and lidar points into image feature-point matching, which is suitable for diverse road scenes compared with existing methods.

Introduction

Mobile mapping systems (MMS) can quickly obtain 2D optical image sequences and 3D lidar points simultaneously, and have been extensively used to underpin many applications, e.g., autonomous vehicle navigation, high-precision mapping, virtual reality, and online street views. In order to capture optical images with a large field of view, panoramic cameras are commonly used in MMS. Comprising two types of MMS data, the registration of lidar points and panoramic-image sequences is important for texturing 3D models (Abayowa *et al.* 2015; Shan *et al.* 2019; Yang and Dong 2019), object extraction (Yang *et al.* 2013, 2017), and point-cloud classification (Barnea and Filin 2013; Yang and Dong 2013).

Currently, many registration methods exist for both 2D and 3D data, and can be divided into three categories: 2D-2D (Taylor and Nieto 2013; Gong *et al.* 2014; Parmehr *et al.* 2014; Brown *et al.* 2015; Lv and Ren 2015; Pascoe *et al.* 2015; Miled *et al.* 2016; Plötz and Roth 2017; Zhu *et al.* 2018), 2D-3D (Lepetit *et al.* 2009; Liu and Stamos 2012; Shao *et al.* 2017;

Zang *et al.* 2019; Zhu *et al.* 2019) and 3D-3D (Kaminsky *et al.* 2009; Corsini *et al.* 2013; Zheng *et al.* 2013; Yang and Chen 2015; Dong *et al.* 2020; Liang *et al.* 2020). However, panoramic images are special 2D optical images that can be difficult to register (Zhu *et al.* 2018; Zhu 2019). The existing registration methods for MMS lidar points and panoramic images mostly rely on global positioning systems (GPSs)/inertial measurement units (IMUs; Yao *et al.* 2017), by which the position and orientation parameters are obtained directly, but the accuracy can be affected by signal dropouts, leading to unreliable registration results (Miled *et al.* 2016). Another common method is point-based registration (Zhu *et al.* 2019), which has accurate precision, but automatic extraction of feature points from lidar points and panoramic-image sequences is difficult (Dong *et al.* 2017; Dong *et al.* 2018; Ma *et al.* 2018; Zai *et al.* 2018; Wen *et al.* 2019), and manual selection in a panoramic-image sequence is unrealistic.

In addition, Cui *et al.* (2017) extracted line features from lidar points and corresponding mono-images; however, this method requires manual intervention. Chen *et al.* (2018) proposed an automatic registration method for MMS lidar points and panoramic-image sequences where hierarchical object extraction is applied to lidar data to extract building facades; hence this registration method relies on the existence of building objects. Li *et al.* (2018) extracted vehicles from panoramic images via Faster-RCNN, then used particle-swarm optimization to refine the translation parameters; however, this method relies on parked vehicles.

Zhu *et al.* (2018) proposed a skyline-based method to automatically register lidar points and panoramic-image sequences. The skyline-based registration method requires consistency of the skyline in the image and lidar points, but the lidar sensor is limited by scanning distance. In an urban area, such as data set I in this article, the skyline is mostly composed of nearby buildings, in which case the skyline-based registration method is useful. However, in the case of data set II in this article, which is along a high-speed road, the skyline in the panoramic image is mainly composed of distant mountains, and the skyline in lidar points is composed only of near ground objects; thus this method would fail for such scenes (a similar situation holds with data set III in this article). Second, the skyline-based method is an optimization method, meaning if the initial parameters are not accurate, the optimization could stop at local minima; otherwise, the optimization effect is not obvious.

Later, Zhu *et al.* (2019) proposed a method based on road lamps and lanes to register MMS lidar points and panoramic-image sequences. The method uses feature points to solve the

Ningning Zhu, Bisheng Yang, Zhen Dong, and Chi Chen are with the State Key Laboratory of Information Engineering in Surveying, Mapping and Remote Sensing, Wuhan University, Wuhan 430079, China (bshyang@whu.edu.cn).

Xia Huang is with the School of Remote Sensing and Information Engineering, Wuhan University, Wuhan 430079, China.

Wen Xiao is with the School of Engineering, Newcastle University, Newcastle Upon Tyne NE1 7RU, UK.

Contributed by Bo Wu, March 3, 2021 (sent for review June 16, 2021; reviewed by Xuming Ge, Wai Yeung Yan).

Photogrammetric Engineering & Remote Sensing
Vol. 87, No. 12, December 2021, pp. 913–922.
0099-1112/21/913–922

© 2021 American Society for Photogrammetry
and Remote Sensing
doi: 10.14358/PERS.21-00006R2

registration parameters directly. First, road lamps and lane markings are common objects in a road scene, which means this method has broader applicability than the skyline-based method in data set I. Second, the requirement for initial parameters is low, i.e., only the initial position parameters. Third, as to the registration accuracy, the average error of this method is better than that of the skyline-based method using the same panoramic images. However, this method will also fail in a scene without road lamps and lanes, such as data set II.

In summary, current registration methods are mainly limited by the scene, hence we propose using a relative orientation model to register MMS lidar points and panoramic-image sequences. As a panoramic-image sequence has high overlap, feature points can be easily extracted and matched from panoramic-image pairs. Our registration method tackles only the image pairs, and does not extract features from lidar points, which is suitable for diverse road scenes compared with existing methods.

Materials and Method Overview

Three sets of test data—data sets I, II, and III—are used in this article, representing three different road scenes. Figure 1 shows the MMS lidar points (3.8 million points) and corresponding 10 panoramic images (4000 × 8000 pixels) in data set I (located in Wuhan, China), in which the distance interval between adjacent images is about 7 m. The length and height difference of this road surface are, respectively, 250 m and 4.6 m. Figure 2 shows the MMS lidar points (8.2 million points) and corresponding seven panoramic images (4096 × 8192 pixels) in data set II (located in Chongqing, China), in which the distance interval between adjacent images is about 20 m. The length and height difference of this road surface are, respectively, 350 m and 2.2 m. Figure 3 shows the MMS lidar points (18.5 million points) and corresponding 11 panoramic images (4096 × 8192 pixels) in data set III (located in Shanghai, China), in which the distance between adjacent images is about 16 m. The length and height difference of this road surface are, respectively, 550 m and 0.5 m. The initial values of the camera position and attitude are all known in all three data sets; however, attitude parameters have large errors, and thus cannot be

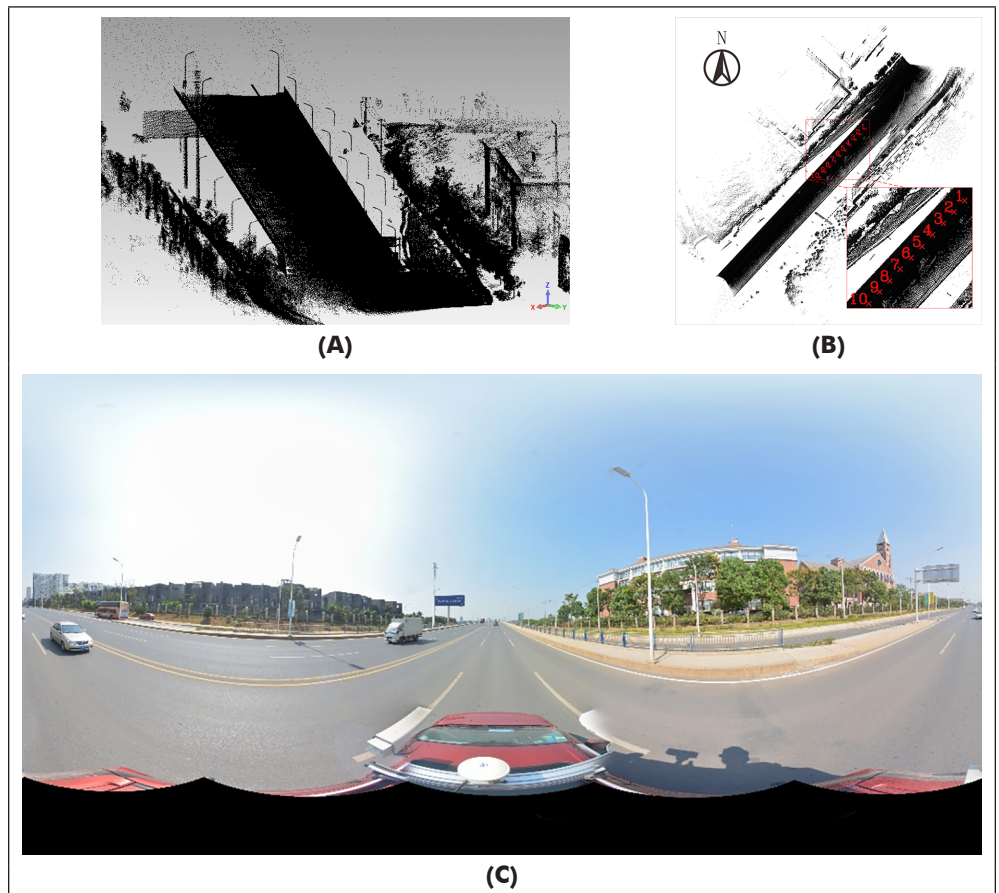


Figure 1. Data set I. (A) and (B) The mobile mapping system lidar points; red numbers in (b) mark the locations of the 10 panoramic images. (C) Panoramic image 1.

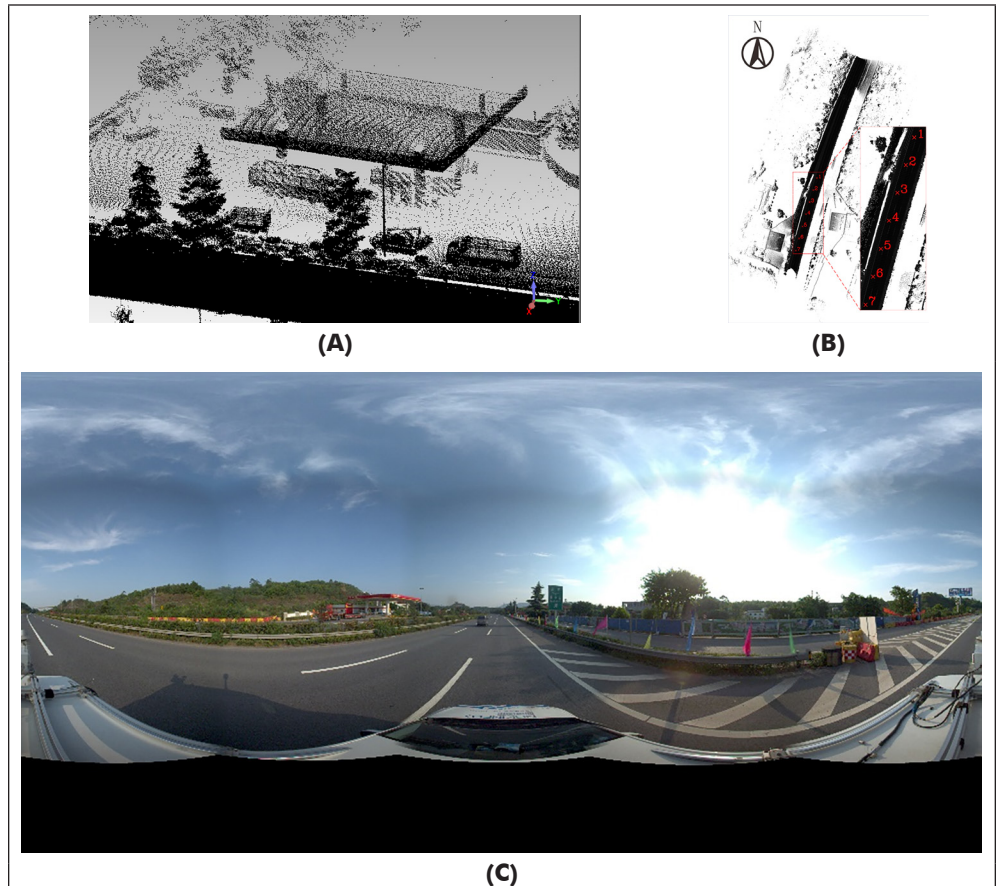


Figure 2. Data set II. (A) The mobile mapping system lidar points; red numbers mark the locations of the seven panoramic images. (B) Panoramic image 1.

directly used for registration (Zhu *et al.* 2018).

Figure 4 shows the flowchart of our registration method. First, the SURF algorithm (Bay *et al.* 2008) is used to extract and match feature points from panoramic-image pairs (Figure 4A and 4B). Second, a relative orientation model for panoramic images (PROM) is used to calculate the relative parameters by the matched points. Third, the absolute parameters of the next panoramic image (Figure 4B) can be calculated by the relative parameters and absolute parameters of the previous panoramic image (Figure 4A). The remainder of the article is organized as follows. The next section explains the PROM of panoramic images. In the section after that, comparative experiments are conducted to verify the effectiveness of the proposed registration method. Then the precision, automation, and weaknesses of the method are discussed. Finally, the conclusions are presented.

The PROM

In this section, the PROM is proposed that is used to calculate the attitude parameters. Then the optimization of the PROM is investigated. The diagram and notations of the PROM are shown in Figure 5.

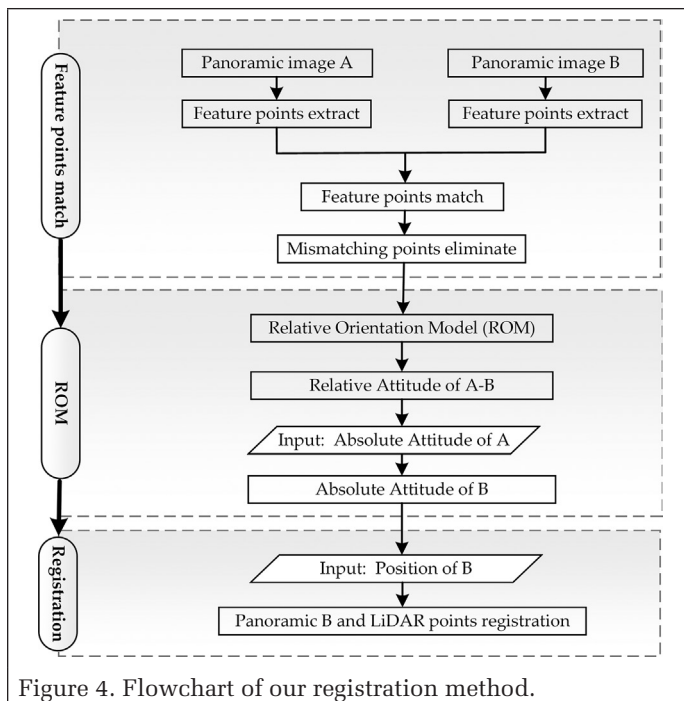


Figure 4. Flowchart of our registration method.

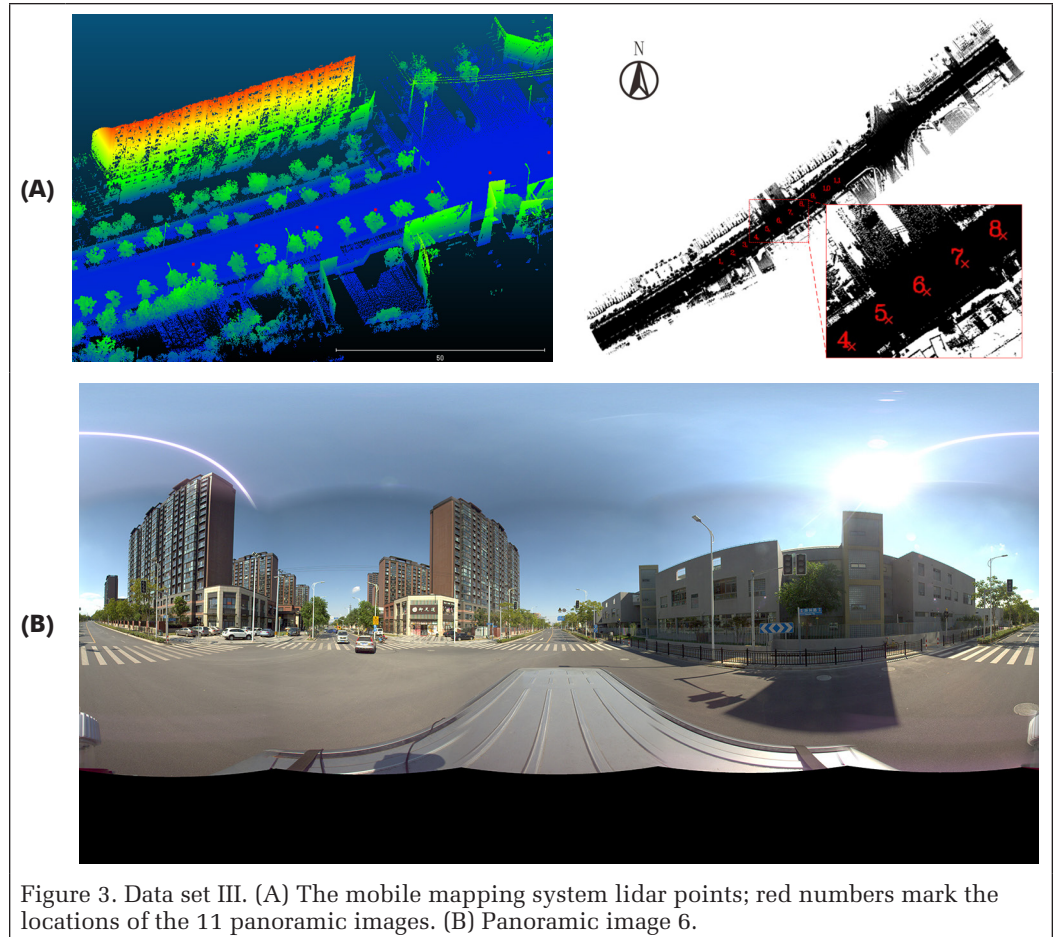


Figure 3. Data set III. (A) The mobile mapping system lidar points; red numbers mark the locations of the 11 panoramic images. (B) Panoramic image 6.

Description

The PROM is the relative orientation model of a panoramic-image pair. A panoramic image is formed by stitching multiple images from different perspectives based on a fixed projection. The most common panoramic camera model (Zhu 2019) is

$$\begin{cases} r_p = \tan^{-1} \left(\frac{\bar{Z}}{\sqrt{\bar{X}^2 + \bar{Y}^2}} \right) \times D \\ c_p = \tan^{-1} \left(\frac{\bar{X}}{\bar{Y}} \right) \times D \end{cases} \quad (1)$$

where $[\bar{X} \ \bar{Y} \ \bar{Z}]^T = \mathbf{R} \times [x - X_s \ y - Y_s \ z - Z_s]^T$, \mathbf{R} is the angular rotation matrix, (x, y, z) is the coordinates of object, (X_s, Y_s, Z_s) is the coordinates of the camera center, r_p and c_p

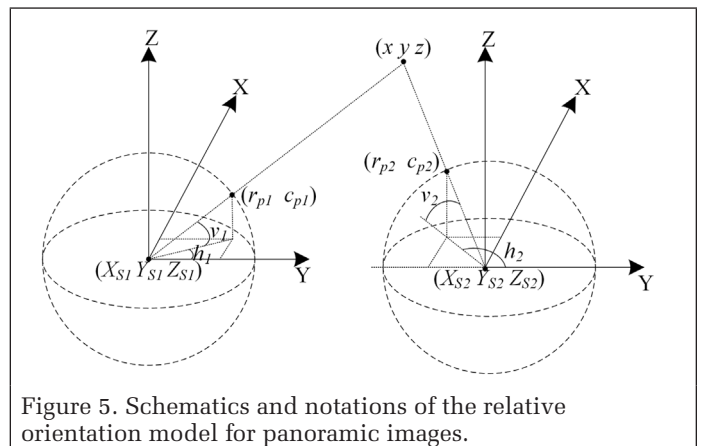


Figure 5. Schematics and notations of the relative orientation model for panoramic images.

are the coordinates of the object in the panoramic image, and D (pixels/rad) is used to convert radians and image sizes.

The epipolar line is expressed as

$$[x - X_s \quad y - Y_s \quad z - Z_s]^T = |\bar{Y}| \cdot \mathbf{R}^{-1} \cdot [\bar{X}/\bar{Y} \quad 1 \quad \bar{Z}/\bar{Y}]^T \quad (2)$$

where $\bar{X}/\bar{Y} = \tan h$, $\bar{Z}/\bar{Y} = \tan v / \cosh$, $v = r_p / \text{row} \cdot \pi$ and $h = c_p / \text{col} \cdot 2\pi$ are the vertical and horizontal angles, row and col are the size of the panoramic image, and \mathbf{R}^{-1} is the inverse of \mathbf{R} .

The baseline between panoramic images A and B is $[X_{s2} - X_{s1} \quad Y_{s2} - Y_{s1} \quad Z_{s2} - Z_{s1}]$, where (X_{s1}, Y_{s1}, Z_{s1}) and (X_{s2}, Y_{s2}, Z_{s2}) are the respective camera centers of the images. Then the coplanar equation constructed by the baseline and corresponding epipolar line is

$$\begin{vmatrix} X_{s2} - X_{s1} & x - X_{s1} & x - X_{s2} \\ Y_{s2} - Y_{s1} & y - Y_{s1} & y - Y_{s2} \\ Z_{s2} - Z_{s1} & z - Z_{s1} & z - Z_{s2} \end{vmatrix} = 0 \quad (3)$$

The position parameters (X_s, Y_s, Z_s) have little effect on the registration, which can be used directly from GPS in most cases (Zhu 2019). The relative angular rotation matrix \mathbf{R}_e can be expressed by three attitude parameters $(\kappa, \varphi, \omega)$. Considering that the distance interval between panoramic-image sequences is small, so are the attitude changes, so Equation 3 can be reduced to

$$\begin{vmatrix} d'_x & c & c' - \kappa - \varphi r' \\ d'_y & 1 & \kappa c' + 1 - \omega r' \\ d'_z & r & \varphi c' + \omega + r' \end{vmatrix} = 0 \quad (4)$$

where $[dx' \quad dy' \quad dz']^T = \mathbf{R}_1 \cdot [X_{s2} - X_{s1} \quad Y_{s2} - Y_{s1} \quad Z_{s2} - Z_{s1}]^T$, $c = \tan h$, $r = \tan v / \cosh$, $c' = \tan h'$, $r' = \tan v' / \cosh'$, \mathbf{R}_1 and \mathbf{R}_2 are the rotation matrices of panoramic images A and B, and $\mathbf{R}_e = \mathbf{R}_2^{-1} \mathbf{R}_1$,

$$\mathbf{R}_e = \begin{bmatrix} 1 & -\kappa & -\varphi \\ \kappa & 1 & -\omega \\ \varphi & \omega & 1 \end{bmatrix}$$

To solve the model, Equation 4 is converted to

$$(nc' - m) \cdot \kappa + (pc' - mr') \cdot \varphi + (p - nr') \cdot \omega = -(mc' + n + pr') \quad (5)$$

where $m = d'_y r - dz'$, $n = dz' \cdot c - dx' \cdot r$, and $p = dx' - d'_x \cdot c$.

The solution model composed of t points is expressed as

$$\mathbf{A}_{t \times 3} \cdot \mathbf{X}_{3 \times 1} = \mathbf{B}_{t \times 1} \quad (6)$$

where $\mathbf{A}_{t \times 3} = [nc' - m \quad pc' - mr' \quad p - nr']$, $\mathbf{X}_{3 \times 1} = [\kappa \quad \varphi \quad \omega]^T$, and $\mathbf{B}_{t \times 1} = [-(mc' + n + pr')]$.

Finally, the unknown matrix $\mathbf{X}_{3 \times 1}$ can be calculated by

$$\mathbf{X} = (\mathbf{A}^T \mathbf{A})^{-1} \cdot (\mathbf{A}^T \mathbf{B}) \quad (7)$$

The absolute attitude matrix \mathbf{R}_2 of panoramic image B is then obtained by

$$\mathbf{R}_2 = \mathbf{R}_e^{-1} \mathbf{R}_1 \quad (8)$$

Optimization

The mismatched feature points from panoramic-image pairs will affect the solution of the PROM, so the RANSAC algorithm is used to optimize the solution. Assuming that the number of matching feature points is m , of which n are randomly selected, there are C_m^n combinations. The average error v is taken as the optimization criterion to select the best group, and the calculation of v in the PROM is explained later.

As shown in Equation 10, after $\mathbf{X}_{3 \times 1}$ is solved by one group of matching feature points in the PROM, the model residuals τ_i of the feature-point pair (r_i, c_i) and (r'_i, c'_i) can be calculated:

$$\tau_{i(i=1,2,\dots,n)} = a_i \cdot m_i + b_i \cdot n_i + c_i \cdot p_i \quad (10)$$

where $a_i = c'_i - \kappa - \varphi r'_i$, $b_i = \kappa c'_i + 1 - \omega r'_i$, $c_i = \varphi c'_i + \omega + r'_i$, $m_i = d'_y \cdot r_i - dz'$, $n_i = dz' \cdot c_i - dx' \cdot r_i$, and $p_i = dx' - d'_x \cdot c_i$.

As shown in Equation 11, δ_i^A and δ_i^B are the distance from (r'_i, c'_i) in panoramic image A and (r_i, c_i) in panoramic image B to the epipolar line:

$$\begin{cases} \delta_i^A = |\tau_i| / \sqrt{(p_i - m_i \varphi - n_i \omega)^2 + (m_i + n_i \kappa + p_i \varphi)^2} \\ \delta_i^B = |\tau_i| / \sqrt{(a_i \cdot d'_y - b_i \cdot d'_x)^2 + (b_i \cdot d'_z - c_i \cdot d'_y)^2} \end{cases} \quad (11)$$

Thus, the kernel error δ_i of the feature point is expressed (in pixels) as

$$\delta_i = D \cdot \sqrt{\delta_i^{A2} + \delta_i^{B2}}, \quad (i = 1, 2, \dots, n) \quad (12)$$

Finally, v , taken as the evaluation index, is calculated by averaging each δ_i as shown in Equation 13. The group of feature points with the lowest v is selected as the optimal solution.

$$v = \sum_{i=1}^n \delta_i / n \quad (13)$$

Experiments and Results

Data sets I, II, and III are used to assess the proposed PROM method in the experiments. The manual point-based registration method is used for comparison.

Registration with the Manual Method

The manual method is taken as the reference for comparison with the PROM method. Feature points are selected manually from MMS lidar points and panoramic-image sequences, which are also the checkpoints for evaluating registration accuracy. We selected 38, 17, and 20 feature points, respectively, from data sets I, II, and III, but some of them may be occluded in some panoramic-image sequences, so not every feature point is involved in all registrations. The panoramic-image sequence and lidar points are manually registered by these feature points. Tables 1, 2, and 3 list the registration

Table 1. The registration accuracy of 10 panoramic images with the manual method in data set I.

Parameter	1	2	3	4	5	6	7	8	9	10
p	37	37	38	37	36	34	35	36	36	35
d (m)	0.22	0.14	0.37	0.35	0.30	0.62	0.54	0.57	0.48	0.48
δ (pixels)	4.69	6.77	5.62	5.09	5.03	6.16	5.92	6.53	6.70	7.31

Table 2. The registration accuracy of seven panoramic images with the manual method in data set II.

Parameter	1	2	3	4	5	6	7
p	14	15	17	16	16	14	12
d (m)	0.0	0.26	0.44	0.27	0.21	0.27	0.28
δ (pixels)	2.83	2.39	2.68	3.60	4.67	3.24	3.44

Table 3. The registration accuracy of 11 panoramic images with the manual method in data set III.

Parameter	1	2	3	4	5	6	7	8	9	10	11
p	10	14	16	19	12	12	17	17	19	20	20
d (m)	0.24	0.16	0.20	0.18	0.15	0.15	0.22	0.11	0.22	0.21	0.11
δ (pixels)	2.10	2.07	2.34	1.85	2.19	2.32	2.02	3.30	2.84	2.62	2.66

accuracy with 10 panoramic images in data set I, seven in data set II, and 11 in data set III.

In the tables, p is the number of control points in the registration, d is the difference in position parameters between GPS and the manual method, and δ expresses the root-mean-square error of checkpoints in each image. There are 34 (image 6) to 38 (image 3) points used in data set I, 12 (image 7) to 17 (image 3) points used in data set II, and 10 (image 1) to 20 (images 10 and 11) points used in data set III. The error d of position parameters is less than 0.62 m in all three data sets, because the position parameters have little effect on the registration, which can be used directly from GPS. The registration accuracy is good with the manual method, especially for the starting image, where $\delta = 4.69$ pixels (image 1 in data set I), 2.83 pixels (image 1 in data set II), and 2.32 pixels (image 6 in data set III).

Extraction and Matching of Feature Points

As seen in the panoramic images, the rich texture from objects on both sides of road is mainly located in the middle area of the image (separated by the road in the center). Therefore, the

panoramic image is divided into left and right parts automatically by a center column, and then feature points are extracted and matched by the SURF algorithm, which includes the extraction parameter Q and matching parameter T . In addition, we exchange the matched and to-be-matched images, and retain only the feature points match successfully in both directions. Then, since the objects in the panoramic-image sequence gradually move backward relative to the MMS direction of movement, this directional constraint can eliminate mismatching points. Finally, we use the coordinate difference of matching points in different images (external filtering) and in the same image (internal filtering) to optimize the number and distribution of matching points.

Figure 6 shows the feature-point matching of panoramic-image pairs 1-2 in data sets I and II and 6-7 in data set III ($Q = 2000$, $T = 0.4$). Taking pair 1-2 in data set I as an example, both images are divided into left and right parts, and the feature points are extracted and matched respectively. White lines are connections of feature points before filtering, black

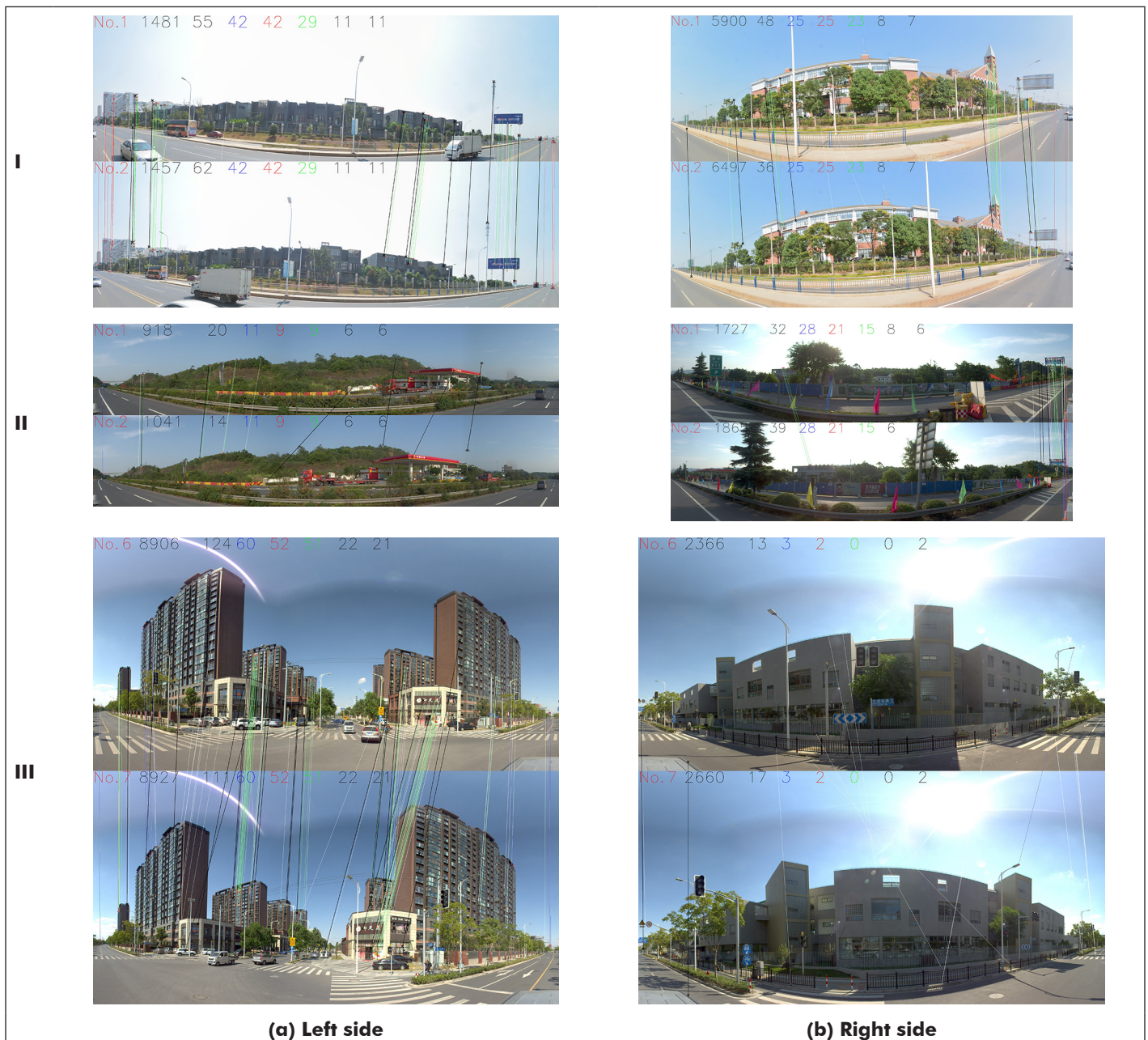


Figure 6. Feature-point matching of panoramic-image pairs 1-2 in data sets I and II and 6-7 in data set III.

Table 4. Extraction and matching of feature points in data set I.

Image Pair	Left Side							Right Side							t
	m_l	n_l	s_l	k_l	p_{l1}	p_{l2}	t_l	m_r	n_r	s_r	k_r	p_{r1}	p_{r2}	t_r	
1-2	1	1481	55	42	42	29	11	5900	48	25	25	23	8	7	18
			62												
2-3	2	1457	53	33	26	17	9	6497	36	13	13	10	8	9	19
			57												
3-4	3	1313	56	31	30	17	8	6199	27	8	8	5	9	4	12
			51												
4-5	4	1445	47	32	32	20	12	6009	24	16	14	11	4	5	17
			53												
5-6	5	1449	58	34	27	17	12	5557	26	14	13	12	5	5	17
			46												
6-7	6	1533	53	28	24	10	6	5164	31	15	13	10	5	8	14
			50												
7-8	7	1435	33	21	18	6	5	4439	26	11	8	6	8	4	9
			40												
8-9	8	1664	48	36	32	16	12	4332	21	9	7	4	4	4	16
			53												
9-10	9	1380	62	42	40	31	14	3740	25	20	18	14	4	5	19
			60												
	10	1346	60					3593	28				5		

dots and lines are feature points and their connections after filtering, and blue, red, and green lines are feature-point connections in the middle of the processes.

First, Figure 6(A) shows in dataset I that the numbers of feature points m_l extracted from images 1 and 2 are 1481 and 1457, of which 55 points in image 1 match with image 2 (n_l) and 62 points in image 2 match with image 1 (n_r); the number of coincident matching points s_l is 42. Second, the number of matching points remains 42 after the direction filtering (k_l). Third, the matching points that are close in different images (p_{l1}) or in the same image (p_{l2}) are eliminated. Setting the threshold to 20 pixels for the former type, 29 points remain after filtering. For the latter type, only one point in a local area is kept if there are multiple matching points. Setting the threshold to 50 pixels, both 11 points remain after filtering in the image pair, so the final number t_l of matched points from the left image is 11. Figure 6(b) shows in data set I the matching points on the right side of the image pair 1-2, where the parameters are the same as the left image and the variables use lowercase r instead of lowercase l. Finally, the matching points from the left and right images ($t = t_l + t_r$) make up the total matching points. Similarly to image pair 1-2, we extract and match the feature points of all 10 panoramic images in data set I. Table 4 lists the results.

As shown in the table, many feature points are initially extracted from the panoramic-image pairs—about 1500 on the left side and 5000 on the right. The number of points after coincidence matching is between 8 and 42. Then after directional, external, and internal filtering, the number is reduced to 4 to 14, and the total number of matched points on both sides is between 9 and 19.

Registration with the PROM Method

The MMS lidar points and panoramic-image sequences are registered by PROM in data sets I, II, and III. We calculate the relative attitude parameters by matched feature points from image pairs, and then compare the results with those of the manual method.

Data Set I

As the accuracy of matched feature points may vary, and not all points are required for optimization, a combination of six points is selected from all matching points to calculate the

Table 5. The registration of nine image pairs in data set I.

Parameter	1-2	2-3	3-4	4-5	5-6	6-7	7-8	8-9	9-10
q	18	19	12	17	17	14	9	16	19
t	18 584	27 132	924	12 376	12 376	3003	84	8008	27 132
v (pixels)	1.29	4.26	1.66	2.99	6.21	4.92	2.05	1.19	1.89
δ (pixels)	4.93	6.24	6.35	6.51	8.14	7.35	8.99	10.34	10.67

relative attitude parameters of panoramic-image pairs, and the one with minimum average parallax is taken as the optimal result after traversing all combinations. Then the registration of next pairs is carried out sequentially. Table 5 shows results for nine image pairs in data set I, in which q and t ($t = C_q^6$) are the numbers of matched feature points and combinations, respectively, and v and δ are the average parallax of matched points and the registration error.

The final registration results are obtained by minimizing v after traversing all combinations. As shown in Table 5, we optimize parameters, with v between 1.19 and 6.21 pixels and δ between 4.93 and 10.67 pixels. These nine pairs are optimized different times; the lowest pair, 7-8, which has 9 matching points and 84 combinations, and the greatest—2-3 and 9-10—both have 19 matching points and 27 132 combinations.

The MMS lidar points are projected to panoramic images according to the parameters solved by the PROM. Limited by space, Figure 7 shows partial registration results of panoramic images 2, 6, and 10. The experimental results show that the lidar points and images are well aligned, and hence the registration method is effective. Table 6 shows the registration accuracy of the 10 panoramic images in data set I with the manual and PROM methods.

In the table, image 1 is the starting image in the PROM method, which is registered by the manual method, so the accuracy is 4.69 pixels for both methods. Excluding image 1, the average registration errors of images 2 through 10 by the two methods are 6.12 pixels for the manual method and 7.72 pixels for the PROM method, showing that the manual method is slightly better. Note that the registration error of the PROM method increases gradually from image 1 to image 10 (image 7 is the only exception). This shows that the PROM method has limitations, i.e., the registration error will accumulate with increasing images. In this case, we can reselect and



Figure 7. The registration results of panoramic images (A) 2, (B) 6, and (C) 10 in data set I.

recalculate the starting image with the manual method, then use the PROM method to register the subsequent images.

Data Sets II and III

Using the same process as with data set I, a combination of six feature points is selected from panoramic-image pairs in data sets II and III. Note that image 1 is the starting image in data set II (1-2, ..., 6-7) and image 6 is the starting image in data set III (6-5, ..., 2-1, 6-7, ..., 10-11). Traversing all combinations, the one with the minimum average parallax of both images is taken as the optimal result. Tables 7 and 8 show the registration process in the two data sets.

As shown in the tables, the number of matching points q is between 7 and 15 in data set II and between 6 and 23 in data set III. The registration error δ is between 2.87 and 4.89 pixels in data set II and between 3.84 and 8.45 pixels in data set III. Figure 8 shows partial registration results of panoramic images 2, 4, and 7 in data set II. Figure 9 shows partial registration results of panoramic images 1, 3, 5, 7, 9, and 11 in data set III.

As shown in the figures, the MMS lidar points are projected onto panoramic images according to the parameters solved by the PROM. The results show that the lidar points are well registered with the images. Again, excluding image 1, the average registration error of images 2 through 7 in data set II using the manual and PROM methods, respectively, is 3.34 and 4.02 pixels. Excluding image 6, the average registration error of images 1 through 11 in data set III using the two methods is 2.40 and 5.77 pixels, respectively.

Table 6. Registration accuracy (in pixels) of 10 panoramic images in dataset I with the manual and PROM methods.

Method	1	2	3	4	5	6	7	8	9	10
Manual	4.69	6.77	5.62	5.09	5.03	6.16	5.92	6.53	6.70	7.31
PROM	4.69	4.93	6.24	6.35	6.51	8.14	7.35	8.99	10.34	10.67

Table 7. The registration of six image pairs in data set II.

Parameter	1-2	2-3	3-4	4-5	5-6	6-7
q	12	15	15	10	13	7
δ (pixels)	2.87	3.23	4.02	4.89	4.83	4.33

Table 8. The registration of 11 image pairs in data set III.

Parameter	2-1	3-2	4-3	5-4	6-5	6-7	7-8	8-9	9-10	10-11
q	11	7	12	10	23	23	17	8	8	6
δ (pixels)	7.64	7.75	4.75	3.84	4.05	4.01	6.27	4.86	6.16	8.45

Discussion

The Precision of Panoramic Registration

Feature points are selected manually from MMS lidar points and panoramic-image sequences as checkpoints to evaluate the registration accuracy. In theory, checkpoints located in the top and bottom of panoramic images have larger registration errors (Zhu 2019), so the registration accuracy is influenced by the distribution of checkpoints. In the foregoing experiments, 38, 17, and 20 checkpoints were selected from data

sets I, II, and III, respectively, evenly distributed to mitigate that influence. In this section, we analyze the influence of checkpoint distribution in detail, taking the 10 images in data set I and the manual method as an example. Table 9 shows the registration accuracy influenced by checkpoint distribution.

As shown in the table, we use checkpoints in different areas, which are divided by row in the panoramic image. The first and last row correspond to 0.5π and -0.5π , respectively, but all 38 checkpoints are located in the top and middle ($>0\pi$) of these images. We set the range of rows, such as $[0-0.5\pi]$ or $[0-0.45\pi]$, in which points are used for registration, and then we can obtain the registration accuracy of the 10 panoramic images with different ranges (corresponding to different number of checkpoints).

The registration accuracy improves with decreasing range. In the case of image 1, there are 38, 37, and 31 checkpoints, respectively, in the rows lower than 0.2π , 0.15π , and 0.1π , and the corresponding accuracy values are 5.24, 4.69, and 3.77 pixels. There are also cases of increasing values, such as in images 2 (0.15π to 0.1π), 7 (0.2π to 0.15π), and 8 (0.15π to 0.1π), but the increases are relatively small. Note that the registration accuracy decreases from 20.00 to 10.07 pixels using 38 and 37 checkpoints in image 6, because there is one checkpoint with a large stitching error, located in the top of the image. Above all, the registration accuracy is affected by the different distributions of checkpoints, but the difference is within 2 pixels in most cases.

Comparison of Different Registration Methods

The PROM method is further compared with the skyline-based method (Zhu *et al.* 2018) and the method using road lamps and lanes (Zhu *et al.* 2019). Table 10 shows the comparison of the three registration methods in terms of applicability, efficiency, initial-value requirements, and accuracy.

The PROM registration method uses the matching feature points in panoramic-image pairs to solve the relative attitude parameters, then combines the absolute position and attitude of the initial image to register the panoramic-image sequence. This

method does not extract features from lidar points, and thus it has the highest applicability in different road scenes, such as in data sets II and III. However, this method can be prone to error accumulation, and it requires precise manual registration of the starting image.

The three registration methods have different applications. The skyline-based method requires that the skyline

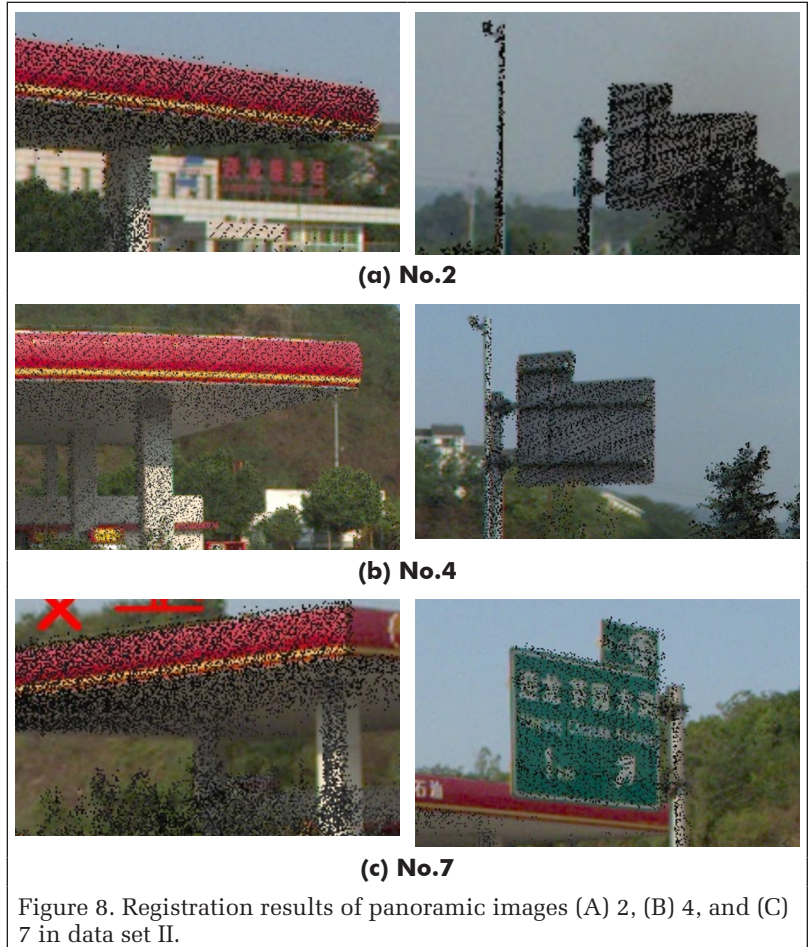


Figure 8. Registration results of panoramic images (A) 2, (B) 4, and (C) 7 in data set II.

Table 9. Registration accuracy (pixels) influenced by checkpoint distribution (number of checkpoints given in parentheses).

Image	0.5π	0.45π	0.4π	0.35π	0.3π	0.25π	0.2π	0.15π	0.1π
1	5.24 (38)	5.24 (38)	5.24 (38)	5.24 (38)	5.24 (38)	5.24 (38)	5.24 (38)	4.69 (37)	3.77 (31)
2	7.17 (38)	7.17 (38)	7.17 (38)	7.17 (38)	7.17 (38)	7.17 (38)	7.17 (38)	6.77 (37)	7.83 (32)
3	5.62 (38)	5.62 (38)	5.62 (38)	5.62 (38)	5.62 (38)	5.62 (38)	5.62 (38)	5.62 (38)	3.82 (32)
4	5.62 (38)	5.62 (38)	5.62 (38)	5.62 (38)	5.62 (38)	5.62 (38)	5.62 (38)	5.09 (37)	4.41 (30)
5	5.39 (38)	5.39 (38)	5.39 (38)	5.39 (38)	5.39 (38)	5.39 (38)	5.11 (37)	5.03 (36)	4.80 (30)
6	20.00 (38)	20.00 (38)	20.00 (38)	10.07 (37)	10.07 (37)	10.07 (37)	10.07 (37)	6.16 (34)	5.28 (29)
7	8.78 (38)	8.78 (38)	8.78 (38)	8.78 (38)	8.78 (38)	6.33 (37)	5.87 (36)	5.92 (35)	5.14 (30)
8	7.28 (38)	7.28 (38)	7.28 (38)	7.28 (38)	7.28 (38)	7.28 (38)	7.13 (37)	6.53 (36)	6.65 (29)
9	6.86 (38)	6.86 (38)	6.86 (38)	6.86 (38)	6.86 (38)	6.86 (38)	6.82 (37)	6.70 (36)	5.26 (27)
10	8.28 (38)	8.28 (38)	8.28 (38)	8.28 (38)	8.28 (38)	8.14 (36)	8.14 (36)	7.31 (35)	6.68 (28)

Table 10. Comparison of three registration methods.

Parameter	Skyline-based (Zhu <i>et al.</i> 2018)	Road lamps and lanes (Zhu <i>et al.</i> 2019)	PROM
Applicability	The skyline is required, such as in an urban street	A road scene containing road lamps and lanes is required	Suitable for most scenes
Efficiency	The brute-force method in optimal matching is less efficient	Feature points extracted and matched from lidar points and images	Efficient extraction and matching of feature points from images only
Initial values required	Position and attitude	Position	Position
Accuracy	11.08 pixels	10.45 pixels	7.72 pixels

be consistent in lidar points and panoramic images, but data sets II and III do not meet this condition. The method using road lamps and lanes requires lamps in the scene, but there is no lamp in data set II, so this method is not applicable. The PROM method is not limited by scene, and is therefore suitable for data sets I, II, and III. Therefore, in order to compare the registration accuracy of the three methods, only data set I is selected, being appropriate for all three methods. The registration accuracy of the PROM method is 7.72 pixels, better than those of the other two methods (using the same five panoramic images in data set I).

Conclusion

We propose a method for the registration of MMS lidar points and panoramic-image sequences based on PROM. Three challenging data sets are used to verify the effectiveness of our registration method. Compared with other methods, our method transforms the registration of panoramic images and lidar points into image feature-point matching, and thus it can avoid the complex task of extracting and matching feature points from images and lidar points, making it widely suitable for most road scenes.

Acknowledgments

The authors would to thank Prof. S. J. from Wuhan University, Wuhan, China, for help with providing data set I. This research was funded by the National Science Fund for Distinguished Young Scholars of China (grant 41725005), supported by LIEMARS Special Research Funding, the Guangxi Zhuang Autonomous Region Remote Sensing Institute of Natural Resources (grant GXZC2019-G3-000703-GXDC), and the National Nature Science Foundation of China (grant 42101446).

References

- Abayowa, B. O., A. Yilmaz and R. C. Hardie. 2015. Automatic registration of optical aerial imagery to a LiDAR point cloud for generation of city models. *ISPRS Journal of Photogrammetry and Remote Sensing* 106:68–81. <https://doi.org/10.1016/j.isprsjsprs.2015.05.006>.
- Barnea, S. and S. Filin. 2013. Segmentation of terrestrial laser scanning data using geometry and image information. *ISPRS Journal of Photogrammetry and Remote Sensing* 76:33–48. <https://doi.org/10.1016/j.isprsjsprs.2012.05.001>.
- Bay, H., A. Ess, T. Tuytelaars and L. Van Gool. 2008. Speeded-Up Robust Features (SURF). *Computer Vision and Image Understanding* 110(3):346–359. <https://doi.org/10.1016/j.cviu.2007.09.014>.
- Brown, M., D. Windridge and J.-Y. Guillemot. 2015. Globally optimal 2D-3D registration from points or lines without correspondences. Pages 2111–2119 in *2015 IEEE International Conference on Computer Vision (ICCV)*, held in Santiago, Chile, 7–13 December 2015. <https://doi.org/10.1109/ICCV.2015.244>.



Figure 9. Registration results of panoramic images (A) 1, (B) 3, (C) 5, (D) 7, (E) 9, and (F) 11 in data set III.

- Chen, C., B. Yang, M. Tian, J. Li, X. Zou, W. Wu and Y. Song. 2018. Automatic registration of vehicle-borne mobile mapping laser point cloud and sequent panoramas. *Acta Geodaetica et Cartographica Sinica* 47(2):215–224. <https://doi.org/10.11947/j. AGCS.2018.20170520>.
- Corsini, M., M. Dellepiane, F. Ganovelli, R. Gherardi, A. Fusiello and R. Scopigno. 2013. Fully automatic registration of image sets on approximate geometry. *International Journal of Computer Vision* 102:91–111. <https://doi.org/10.1007/s11263-012-0552-5>.
- Cui, T., S. Ji, J. Shan, J. Gong and K. Liu. 2017. Line-based registration of panoramic images and LiDAR point clouds for mobile mapping. *Sensors* 17(1):70. <https://doi.org/10.3390/s17010070>.
- Dong, Z., F. Liang, B. Yang, Y. Xu, Y. Zang, J. Li, Y. Wang, W. Dai, H. Fan, J. Hyypää and U. Stilla. 2020. Registration of large-scale terrestrial laser scanner point clouds: A review and benchmark. *ISPRS Journal of Photogrammetry and Remote Sensing* 163:327–342. <https://doi.org/10.1016/j.isprsjprs.2020.03.013>.
- Dong, Z., B. Yang, F. Liang, R. Huang and S. Scherer. 2018. Hierarchical registration of unordered TLS point clouds based on binary shape context descriptor. *ISPRS Journal of Photogrammetry and Remote Sensing* 144:61–79. <https://doi.org/10.1016/j.isprsjprs.2018.06.018>.
- Dong, Z., B. Yang, Y. Liu, F. Liang, B. Li and Y. Zang. 2017. A novel binary shape context for 3D local surface description. *ISPRS Journal of Photogrammetry and Remote Sensing* 130:431–452. <https://doi.org/10.1016/j.isprsjprs.2017.06.012>.
- Gong, M., S. Zhao, L. Jiao, D. Tian and S. Wang. 2014. A novel coarse-to-fine scheme for automatic image registration based on SIFT and mutual information. *IEEE Transactions on Geoscience and Remote Sensing* 52(7):4328–4338. <https://doi.org/10.1109/ TGRS.2013.2281391>.
- Kaminsky, R. S., N. Snavely, S. M. Seitz and R. Szeliski. 2009. Alignment of 3D point clouds to overhead images. Pages 63–70 in 2009 *IEEE Computer Society Conference on Computer Vision and Pattern Recognition Workshops*, held in Miami, FL, 20–25 June 2009. <https://doi.org/10.1109/CVPR.2009.5204180>.
- Lepetit, V., F. Moreno-Noguer and P. Fua. 2009. EPnP: An accurate O(n) solution to the PnP problem. *International Journal of Computer Vision* 81:155–166. <https://doi.org/10.1007/ s11263-008-0152-6>.
- Li, J., B. Yang, C. Chen, R. Huang, Z. Dong and W. Xiao. 2018. Automatic registration of panoramic image sequence and mobile laser scanning data using semantic features. *ISPRS Journal of Photogrammetry and Remote Sensing* 136:41–57. <https://doi.org/10.1016/j.isprsjprs.2017.12.005>.
- Liang, F., B. Yang, Z. Dong, R. Huang, Y. Zang and Y. Pan. 2020. A novel skyline context descriptor for rapid localization of terrestrial laser scans to airborne laser scanning point clouds. *ISPRS Journal of Photogrammetry and Remote Sensing* 165:120–132. <https://doi.org/10.1016/j.isprsjprs.2020.04.018>.
- Liu, L. and I. Stamos. 2012. A systematic approach for 2D-image to 3D-range registration in urban environments. *Computer Vision and Image Understanding* 116(1):25–37. <https://doi.org/10.1016/j.cviu.2011.07.009>.
- Lv, F. and K. Ren. 2015. Automatic registration of airborne LiDAR point cloud data and optical imagery depth map based on line and points features. *Infrared Physics & Technology* 71:457–463. <https://doi.org/10.1016/j.infrared.2015.06.006>.
- Ma, L., Y. Li, J. Li, C. Wang, R. Wang and M. A. Chapman. 2018. Mobile laser scanned point-clouds for road object detection and extraction: A review. *Remote Sensing* 10(10):1531. <https://doi.org/10.3390/rs10101531>.
- Miled, M., B. Soheilian, E. Habets and B. Vallet. 2016. Hybrid online mobile laser scanner calibration through image alignment by mutual information. *ISPRS Annals of the Photogrammetry, Remote Sensing and Spatial Information Sciences* III-1:25–31. <https://doi.org/10.5194/isprsannals-III-1-25-2016>.
- Parmehr, E. G., C. S. Fraser, C. Zhang and J. Leach. 2014. Automatic registration of optical imagery with 3D LiDAR data using statistical similarity. *ISPRS Journal of Photogrammetry and Remote Sensing* 88:28–40. <https://doi.org/10.1016/j.isprsjprs.2013.11.015>.
- Pascoe, G., W. Maddern and P. Newman. 2015. Robust direct visual localisation using normalised information distance. Pages 1–13 in *Proceedings of the British Machine Vision Conference*, held in Swansea, UK, 7–10 September 2015. Edited by X. Xie, M. W. Jones, and G. K. L. Tam. <https://dx.doi.org/10.5244/C.29.70>.
- Plötz, T. and S. Roth. 2017. Automatic registration of images to untextured geometry using average shading gradients. *International Journal of Computer Vision* 125:65–81. <https://doi.org/10.1007/s11263-017-1022-x>.
- Shan, J., Z. Li and W. Zhang. 2019. Recent progress in large-scale 3D city modeling. *Acta Geodaetica et Cartographica Sinica* 48(12):1523–1541. <https://doi.org/10.11947/j. AGCS.2019.20190471>.
- Shao, J., W. Zhang, Y. Zhu and A. Shen. 2017. Fast registration of terrestrial LiDAR point cloud and sequence images. *International Archives of the Photogrammetry, Remote Sensing and Spatial Information Sciences* XLII-2/W7:875–879. <https://doi.org/10.5194/isprs-archives-XLII-2-W7-875-2017>.
- Taylor, Z. and J. Nieto. 2013. Automatic calibration of lidar and camera images using normalized mutual information. *IEEE Conf. Robot. Autom.*
- Wen, C., X. Sun, J. Li, C. Wang, Y. Guo and A. Habib. 2019. A deep learning framework for road marking extraction, classification and completion from mobile laser scanning point clouds. *ISPRS Journal of Photogrammetry and Remote Sensing* 147:178–192. <https://doi.org/10.1016/j.isprsjprs.2018.10.007>.
- Yang, B. and C. Chen. 2015. Automatic registration of UAV-borne sequent images and LiDAR data. *ISPRS Journal of Photogrammetry and Remote Sensing* 101:262–274. <https://doi.org/10.1016/j.isprsjprs.2014.12.025>.
- Yang, B. and Z. Dong. 2013. A shape-based segmentation method for mobile laser scanning point clouds. *ISPRS Journal of Photogrammetry and Remote Sensing* 81:19–30. <https://doi.org/10.1016/j.isprsjprs.2013.04.002>.
- Yang, B. and Z. Dong. 2019. Progress and perspective of point cloud intelligence. *Acta Geodaetica et Cartographica Sinica* 48(12):1575–1585. <https://doi.org/10.11947/j. AGCS.2019.20190465>.
- Yang, B., F. Liang and R. Huang. 2017. Progress, challenges and perspectives of 3D LiDAR point cloud processing. *Acta Geodaetica et Cartographica Sinica* 46(10):1509–1516. <https://doi.org/10.11947/j. AGCS.2017.20170351>.
- Yang, B., W. Xu and Z. Dong. 2013. Automated extraction of building outlines from airborne laser scanning point clouds. *IEEE Geoscience and Remote Sensing Letters* 10(6):1399–1403. <https://doi.org/10.1109/LGRS.2013.2258887>.
- Yao, L., H. Wu, Y. Li, B. Meng, J. Qian, C. Liu and H. Fan. 2017. Registration of vehicle-borne point clouds and panoramic images based on sensor constellations. *Sensors* 17(4):837. <https://doi.org/10.3390/s17040837>.
- Zai, D., J. Li, Y. Guo, M. Cheng, Y. Lin, H. Luo and C. Wang. 2018. 3-D road boundary extraction from mobile laser scanning data via supervoxels and graph cuts. *IEEE Transactions on Intelligent Transportation Systems* 19(3):802–813. <https://doi.org/10.1109/ TITS.2017.2701403>.
- Zang, Y., B. Yang, J. Li and H. Guan. 2019. An accurate TLS and UAV image point clouds registration method for deformation detection of chaotic hillside areas. *Remote Sensing* 11(6):647. <https://doi.org/10.3390/rs11060647>.
- Zheng, S., R. Huang and Y. Zhou. 2013. Registration of optical images with LiDAR data and its accuracy assessment. *Photogrammetric Engineering and Remote Sensing* 79(8):731–741.
- Zhu, N. 2019. Simulation analysis of spherical panoramic mosaic. *Signal Processing* 158:190–200. <https://doi.org/10.1016/j. sigpro.2019.01.012>.
- Zhu, N., Y. Jia and X. Huang. 2019. Semiautomatically register MMS LiDAR points and panoramic image sequence using road lamp and lane. *Photogrammetric Engineering and Remote Sensing* 85(11):829–840. <https://doi.org/10.14358/PERS.85.11.829>.
- Zhu, N., Y. Jia and S. Ji. 2018. Registration of panoramic/fish-eye image sequence and LiDAR points using skyline features. *Sensors* 18(5):1651. <https://doi.org/10.3390/s18051651>.

Dense Bathymetry in Turbid Coastal Zones Using Airborne Hyperspectral Images

Steven Martinez Vargas, Claudio Delrieux, Katy L. Blanco, and Alejandro Vitale

Abstract

We used airborne hyperspectral images to generate a dense survey of bathymetric data in the Bahía Blanca estuary (Buenos Aires Province, Argentina). This estuarine area is characterized by intense sediment transport turning the water muddy, and thus optical bathymetric estimations are difficult. We used 24 spectral bands in a range of 500–900 nm acquired with a hyperspectral camera aboard an unmanned aerial vehicle, together with 100 bathymetry data points surveyed with a sonar sensor aboard an unmanned surface vehicle, covering an area of about 800 m². Random-forest and support-vector-machine regressors were trained with this data set. The resulting model yielded a determination coefficient of 0.815 with unseen data, a root-mean-square error of 0.166 m, and an absolute average error less than 2%. These results allow dense and accurate reconstructions of the underwater profile in wide, muddy, shallow regions of the Bahía Blanca estuary, showing the feasibility of hyperspectral imagery combined with sonar data in turbid shallow waters.

Introduction

Precise and dense bathymetric measurements are extremely valuable in coastal management and planning, specifically in areas with heavy vessel traffic (Su *et al.* 2008). In complex and dynamic estuarine areas, this is especially required to perform environmental, geomorphological, and biological research activities (Stumpf *et al.* 2003). In particular, the Bahía Blanca estuary, located southwest of Buenos Aires Province, Argentina (Figure 1a), comprises more than 2500 km² of intertidal flats, highly interconnected channels, islands, ponds, salt marshes, and other small shallow water bodies, making it one of the most extended and complex coastal environments

Steven Martinez Vargas is with the Consejo Nacional de Investigaciones Científicas y Tecnológicas (CONICET); the Departamento de Ingeniería Eléctrica y de Computadoras (DIEC), Universidad Nacional del Sur (UNS); and the Instituto Argentino de Oceanografía (IADO), Bahía Blanca, Argentina (stevenmv.91@gmail.com).

Claudio Delrieux is with the Consejo Nacional de Investigaciones Científicas y Tecnológicas (CONICET); and the Departamento de Ingeniería Eléctrica y de Computadoras (DIEC), Universidad Nacional del Sur (UNS), Bahía Blanca, Argentina (cad@uns.edu.ar).

Katy L. Blanco is with the Departamento de Ingeniería Eléctrica y de Computadoras (DIEC), Universidad Nacional del Sur (UNS), Bahía Blanca, Argentina (ktyblanco@gmail.com).

Alejandro Vitale is with the Instituto Argentino de Oceanografía (IADO); Consejo Nacional de Investigaciones Científicas y Tecnológicas (CONICET); and the Departamento de Ingeniería Eléctrica y de Computadoras (DIEC) and Departamento de Geografía y Turismo, Universidad Nacional del Sur (UNS), Bahía Blanca, Argentina (vitale.alejandro@gmail.com).

Contributed by Sidike Paheding, April 6, 2021 (sent for review July 13, 2021; reviewed by Mason Maimaitijiang, Abel Angulo).



(a)



(b)

Figure 1. Study area: (a) Bahía Blanca estuary (Source: Instituto Argentino de Oceanografía); (b) localization map (Source: Google Earth).

Photogrammetric Engineering & Remote Sensing
Vol. 87, No. 12, December 2021, pp. 923–927.
0099-1112/21/923–927

© 2021 American Society for Photogrammetry
and Remote Sensing
doi: 10.14358/PERS.21-00015R2

in the world (Marcovecchio and Ferrer 2005; Piccolo *et al.* 2008). The tidal cycles generate both an erosive effect and a thick sediment-transport process (Popovich and Sinclair 2008), which not only turns the water heavily opaque but also modifies the shape and size of small geographical and geomorphological features (Revollo *et al.* 2019). A major difficulty in environmental research in the Bahía Blanca estuary is the lack of wide and accurate bathymetric information. Precise water-depth estimations are key in determining factors related to floods, erosive processes, and ecological habitats, among many other aspects. Traditional bathymetry uses direct means (wires or sticks) or active ultrasound onboard devices. These means provide only point-wise information, and thus are costly and laborious if dense measurements are required in wide regions, in addition to the associated operational risks in shallow-water contexts (Papadopoulou *et al.* 2015; Wang *et al.* 2020). More recent approaches are based on advanced active devices such as multi-beam echo sounders, which provide denser measurements, or airborne lidar. The latter takes advantage of the varying optical properties of water at different wavelengths. For this reason, dual beams in the near-infrared region (1064 nm) and visible green (532 nm) are typically used in water bodies over benthic layers (Allouis *et al.* 2010; Kakuta *et al.* 2018), especially in areas in which navigation is difficult or risky. However, this approach is effectively applicable only in relatively small areas, given the associated high operational costs, and may provide poor results in regions where water carries thick sediment suspensions (Wang *et al.* 2020).

A recent alternative arose from the use of light and (relatively) low-cost passive hyperspectral sensors, which can be practical to attach to unmanned aerial vehicles (UAVs) and provide high-resolution imagery in several optical bands, making the associated operational costs significantly lower (Stumpf *et al.* 2003; Su *et al.* 2008; Wang *et al.* 2020). A simplified justification of the method is based on the fact that the sensed backscattered solar radiation from a uniformly reflective bottom surface depends on a negative exponential function of the water depth (Lyzenga 1981, 1985). This principle enables the methodological design of image-based dense bathymetric estimates. A major disadvantage of this approach is the lack of appropriate calibration methods, since the actual measurements are subject to a superimposition of physical phenomena which are difficult to model and adjust all together, including the daylight spectral radiance distribution, atmospheric correction, suspended sediment absorption, incident and reflected light-path attenuation, and backscattering, to mention only the most relevant uncertainty sources (Su *et*

al. 2008; Papadopoulou *et al.* 2015). For this reason, data fusion appears to be a significant alternative in the integration of passive hyperspectral imagery data in bathymetric estimation. For instance, Pan *et al.* (2016) used hyperspectral imagery together with lidar data for the detection and classification of underwater vegetation. Misra *et al.* (2018) combined Landsat multispectral imaging and echo-sounding measurements on-site using a support vector machine as a predictor for shallow-water bathymetry mapping. These methods have generally shown good results in clear water, but poor results in areas with complex tidal and sediment dynamics. In this work we follow a similar path, combining UAV-based hyperspectral imagery with sonar data from an unmanned surface vessel (USV) to obtain dense bathymetry over a relatively large underwater area of about 800 m². As in these previous works, we do not intend to provide estimates of the physical light-transport parameters. Instead, our purpose is to understand the feasibility and practicability of obtaining useful dense bathymetry by fusing airborne hyperspectral images and echo-sounding measurements. Sonar data taken along a few transects were taken as ground truth for training a random-forest (RF) and a support-vector-machine regression model able to predict the actual depth as a function of the digital numbers in spectral bands. The model was applied to the hyperspectral image, obtaining dense bathymetry for the complete study area.

Materials and Methods

Study Area

The study area is located northeast of the Bahía Blanca estuary, close to the urban settlement of General Cerri and the Cuatros port (Figure 1a and 1b). In this location, the site's depth, tidal cycles, and geomorphological features are representative of other shallow portions, which cover the majority of the estuary's flooded area. In addition, the harbor facilities provide adequate access and UAV and USV operation, and the dock serves as a rigid target for geo-location. Finally, the study area is within the coverage of a differential global positioning system station. This facilitates the complete data-acquisition procedure.

USV Bathymetry

A low-cost USV was used to perform sonar-based bathymetric acquisitions along five transects. The USV was specifically designed and assembled for this purpose by the fourth author at the Instituto Argentino de Oceanografía (Figure 2b), using the open architecture ArduPilot (<https://ardupilot.org/>). The USV includes a 200-kHz Garmin Echo 100 sounder, and

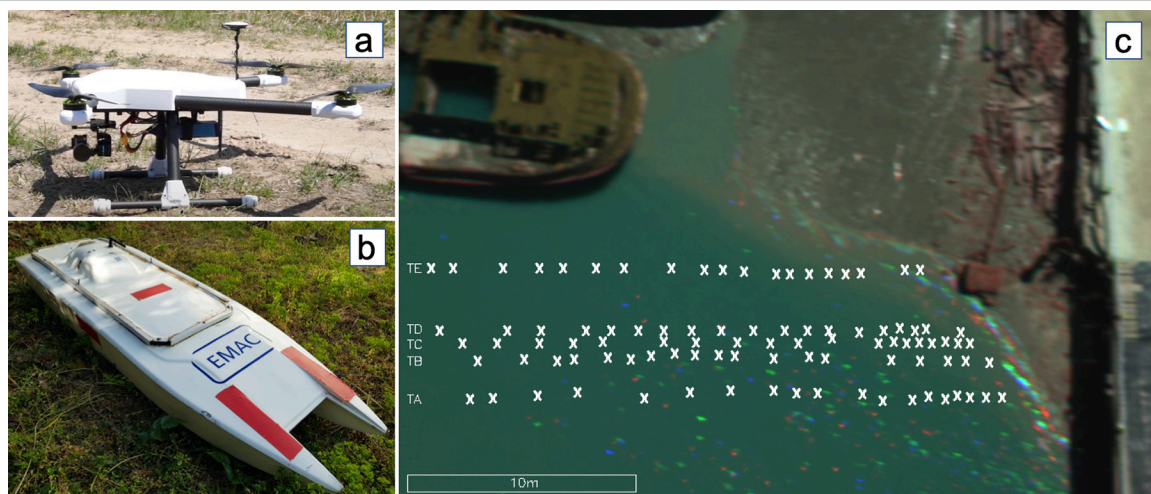


Figure 2. Equipment used for data acquisition: (a) unmanned aerial vehicle with Rikola hyperspectral camera onboard; (b) unmanned surface vessel; (c) bathymetry transects and acquisition locations.

Mission Planner software was used to manage the navigation and monitoring. The acquisition was performed at a 5-Hz rate while the vessel was displacing at an average speed of 1 m/s, to obtain an approximately equally spaced sampling. A total of 100 bathymetric samples were taken (20 per transect, about 30-m length each), covering an area of about 300 m². The acquisition was performed during high tide and with adequate wind conditions, to avoid USV swinging, on 22 February 2018. In Figure 2c, the transects (labeled TA, TB, TC, TD, and TE) and acquisition locations are shown.

Hyperspectral Data

The hyperspectral images were acquired within a few minutes after the USV bathymetry using a Rikola Hyperspectral Imager (Rikola Ltd., Oulu, Finland), which is based on a Fabry–Pérot interferometer (Rikola 2015). It was mounted on a Quanam Spider 700 Professional Multirotor UAV (Figure 2a). Only 24 spectral bands in the range 500–900 nm can be acquired off-line (i.e., onboard) in sequence. The choice of bands was made following several criteria, including spectral distributions of the water transmittance, the suspended sediment absorption, the bottom backscattering, and the goal of verifying the presence of zooplankton and traces of chemicals. In Table 1 we show the actual wavelengths (in the first row) and the digital numbers of the first point of each transect, together with their respective measured depths. Image acquisition was performed with the UAV steadily hovering over the region of interest at an average height of 30 m above ground level, yielding a frame footprint of 36×22 m. Exposure time was set between 10 and 20 ms, according to the upwelling and down-welling radiation and to avoid motion blur. Each spectral band was acquired in a 12-bit, 1024×648 format, (i.e., a pixel size of about 3.6 cm).

Data Preprocessing

Each of the 24 frames corresponding to the spectral bands was processed with Rikola Imager software to correct for lens distortion and calibrate black level. Digital numbers in the range 0–4095 were converted to spectral radiance, in mW/(m² sr nm). Even though the image acquisition was performed

in favorable wind conditions, the small uncompensated UAV swings occurring between the individual band acquisitions resulted in noticeable displacements between pairs of frames, in most cases less than 10 pixels. To register the pixel location adequately, the SIFT algorithm (Lowe 2004) was used to identify a set of 100 key points with which all the frames were registered to the same reference using four-point homography (Szeliski 2011). The frames were finally geo-localized using the differential global positioning system coordinates of known rigid points. Finally, with those coordinates of the USV acquisitions, the 100 bathymetry samples were registered and located within the frames. In this way, a 100×25 data set was built. Each row corresponds to each bathymetry sample and the values of the 24 spectral bands acquired at the same point, after a 3×3 Gaussian smoothing.

Data Analysis and Results

Random-forest and support-vector-machine regressors (Geurts *et al.* 2006) were trained with the data set already described, using the 24 spectral-band values as explanatory variables and the actual bathymetric measure as an explained variable. We used the standard Scikit-Learn Python library implementation (Pedregosa *et al.* 2011). The learning parameters were set as follows: *k*-fold cross-validation *k* = 3, estimators between 10 and 200, max depth between 10 and 110. Hyperparameter tuning was performed using RandomizedSearchCV. The training was performed with the standard 60%, 20%, 20% partition for training, validation, and testing to avoid overfitting. The best model and fold with the test set (data unseen by the model) was RF, with a root-mean-square error of 0.1661 m and coefficient of determination $R^2 = 0.815$. The average absolute error of RF was 0.1233 m, representing less than 10% of the actual depth range. Results can be seen in Tables 1 and 2. RF has better performance (in terms of R^2 , root-mean-square error, and average absolute error) than the support vector machine. In Figure 3a we show a scatterplot of the RF prediction versus the actual bathymetry for the 100 data points. The linear fit of the model has a slope of 1.069

Table 1. Hyperspectral wavelengths, digital numbers, and depths of the first point in the five transects.

Transect	Spectral Band (nm)									
	500	510	525	555	560	600	620	628	670	
TA	1934.0	4643.5	9053.8	10 007.5	10 767.5	12 309.5	13 311.0	13 749.8	11 556.2	
TB	1783.4	4630.1	9026.0	9940.4	10 740.3	12 323.9	13 344.1	13 774.4	11 587.1	
TC	1825.7	4536.7	8844.9	9873.4	10 521.1	12 194.2	13 245.5	13 665.2	11 556.2	
TD	1835.1	4656.8	9151.3	10 208.5	10 781.4	12 424.8	13 771.3	14 083.8	12 159.5	
TE	1821.0	4456.6	8733.5	9662.8	10 356.7	12 093.3	13 311.2	13 847.2	12 020.3	
	675	678	685	698	700	705	710	725	740	750
	11994.5	11 925.5	11 617.7	10 309.1	10 203.3	10 553.8	10 591.9	8791.8	6703.4	6055.9
	12073.7	12 021.6	11 779.3	10 309.1	10 449.3	11 027.8	10 849.5	9402.8	7461.9	7923.6
	12026.2	12 037.6	11 520.8	10 199.6	10 199.1	10 411.6	10 608.0	8842.7	6509.4	6225.7
	12659.2	12 709.9	12 118.7	10 778.4	10 934.3	11 343.8	11 541.7	9996.8	8308.7	7885.9
	12564.2	12 453.8	12 037.8	10 872.3	10 824.8	11 233.2	11 348.5	10 217.5	8502.7	8489.6
					Bathymetry (m)					
					Actual	Predicted (Random Forest)	Absolute Error	Predicted (Support Vector Machine)	Absolute Error	
820	840	870	876	892	8.274	8.279	0.005	8.402	0.128	
6000.6	5186.4	4336.0	4226.2	4054.9	8.452	8.227	0.225	8.303	0.149	
6289.1	5506.6	4725.1	4397.6	4197.7	8.172	8.330	0.158	8.426	0.254	
5962.1	5186.4	4391.6	4112.0	3997.8	7.986	8.014	0.028	8.123	0.109	
7885.4	6787.2	5892.5	5511.2	5311.3	7.828	8.029	0.201	8.170	0.141	
8308.5	7043.3	6170.5	5711.1	5568.3						

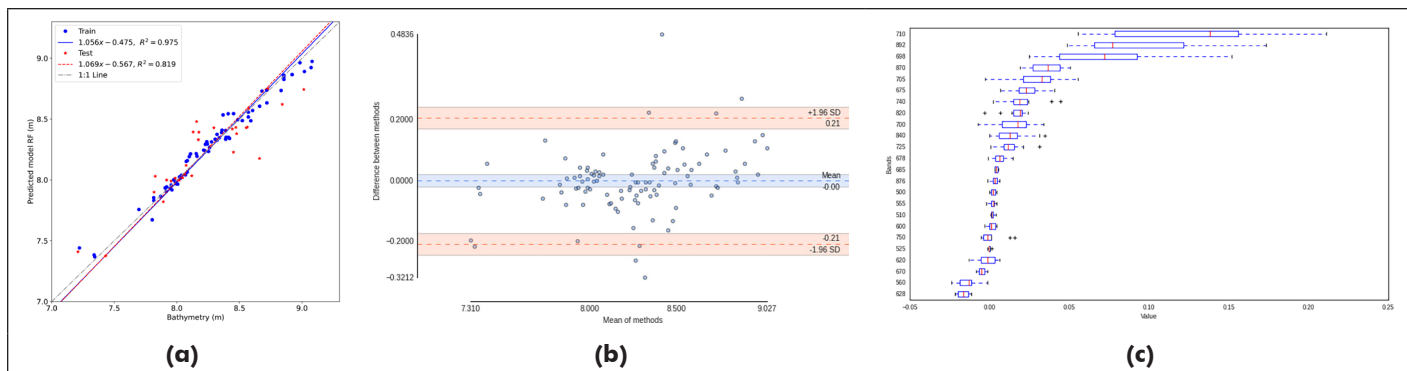


Figure 3. Results for the random-forest model: (a) predicted versus estimated depth in model training and testing; (b) Bland–Altman plot; (c) ablation study.

Table 2. Accuracy of the models for different segments.

Variable	Total Area Models		RF Models by Transect				RF Models by Zone		
	RF	SVM	T AB	Predicted T C	T DE	Predicted TC	Shallower	Intermediate	Deeper
R^2	0.815	0.720	0.727	0.767	0.737	0.763	0.953	0.744	0.717
RMSE	0.166	0.203	0.186	0.186	0.130	0.187	0.069	0.101	0.094
MAE	0.123	0.174	0.128	0.154	0.111	0.139	0.060	0.077	0.067

MAE = mean absolute error; RF = random forest; RMSE = root-mean-square error; SVM = support vector machine; T = transect

with unseen data. Only four outliers can be found with an absolute error of more than 0.2 m (Figure 3b). Finally, the model was applied to the complete hyperspectral image (i.e., a bathymetry was assigned to every pixel in the image according to the model prediction from the corresponding 24 spectral-band values).

An ablation analysis of the relative importance of the different wavelengths in the model shows that the likely confounding variables are few, and are present only in the visible part of the spectrum (far from the red edge). The results of the permutation importance test performed on the different wavelengths used in the model are shown in Figure 3c. It is worth mentioning that the omission of the three confounding wavelengths (560, 628, and 670 nm) generates only a marginal improvement in performance. Two additional ablation tests were performed. In the first, two different models were generated, with data from transects TA and TB and from transects TD and TE, respectively. Then the resulting models were used for depth prediction along transect TC. In the second, the study area was divided into three zones according to depth, each taking one third of each transect (leftmost for the deep zone, middle for the intermediate zone, and rightmost for the shallower zone). Then a model was generated and assessed independently for each zone. The results of these experiments are shown in Table 2. A dense reconstruction displayed as a contour model (generated using Surfer 8) is shown in Figure 4a. Further geomorphological validation was performed by tracing five test transects in the study area to evaluate the plausibility of the seabed profiles obtained. Each transect has an approximate length of 18 m and a separation of about 1.8 m (Figure 4b). The predicted bathymetry along the transects was computed and the resulting seabed profiles were evaluated by expert geomorphologists with experience in the area (Figure 4c), who concluded that the overall predicted texture, slope, and shape are fully coincident with underwater observations performed in other areas of the estuary.

Discussion and Conclusion

We presented a methodology with the potential to obtain dense bathymetries in turbid coastal shallow water using hyperspectral imagery. A set of 100 sample points were

measured with a 200-kHz Garmin Echo sounder, taken as a gold standard. A 24-band hyperspectral image was acquired at the same time, to which the bathymetric measurements were registered. These measurements were used together with the spectral values to train a random-forest model that predicts the expected bathymetric value given the spectral values. The predicted bathymetries presented very low root-mean-square error (less than 20 cm) compared to the actual ones. Very few outliers arose, attributed to far-from-ideal acquisition conditions. The regression line was very close to the identity line, with a significantly high coefficient of determination, which proved the accuracy and precision of the model. A dense bathymetric map for all the images can be computed from the complete image, which can be useful for studying sediment-transport phenomena in the bottom surface of the estuary.

We performed several ablation tests to assess the robustness of the model. First, an analysis of the relative importance of the wavelengths shows less importance and confounding information in the visible spectrum. The likely explanation for this is that light transmittance coefficients differ from the Jerlov type III model, due to the amount of suspended sediment and the presence of algae and zooplankton. In the second and third ablation tests, the transect data were split according to two different criteria, transverse and longitudinal. In the longitudinal analysis (i.e., taking fewer transects), it was shown that the predictive power degrades slightly concerning the complete data sets and that the predictions using noncontiguous data are consistent. This implies that in the same conditions (illumination, suspended sediments, etc.), the methodology presented will have uniform predictions. In the transverse analysis, it can be seen that model performance decreases concerning depth, which can be interpreted as a gradual loss of hyperspectral data precision given the accumulated uncertain factors in deeper light transport paths.

Among future work based on these preliminary results, the most challenging is to modify the electronic setting of the hyperspectral imager in a way such as to extract more than 24 spectral bands in off-line acquisition. For this, an embedded system is being designed to emulate the online operational context of the camera, enabling—in principle—the extraction of up to 394 spectral bands in the range 500–900 nm. With this information, it will be possible to precisely characterize

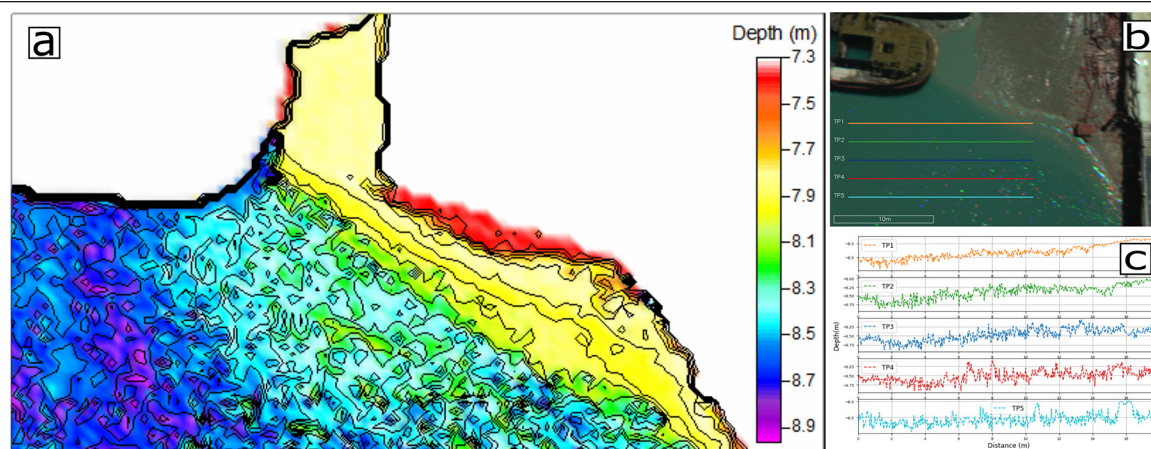


Figure 4. Dense bathymetry results: (a) predicted dense bathymetry map of the study area; (b) validation transects; (c) respective predicted seabed profiles.

the spectral end members of the suspended sediment, and therefore to compute dense bathymetries in wider regions in which there is no gold standard (under the assumption that the sediment absorption and microdispersion are known). On the other hand, for regions in which the water depth is roughly known, the imaging would be able to determine the amount of suspended sediment. Also, it would be possible to detect the presence of chemicals and contaminants with known spectral absorption properties, which is also a highly required environmental-monitoring task in several locations along the Bahía Blanca estuary.

References

- Allouis, T., J.-S. Bailly, Y. Pastol and C. Le Roux. 2010. Comparison of LiDAR waveform processing methods for very shallow water bathymetry using Raman, near-infrared and green signals. *Earth Surface Processes and Landforms* 35(6):640–650. <https://doi.org/10.1002/esp.1959>.
- Chamberlin, J., A. Novotney, E. Packard and M. Price. 2008. Enhancing worker well-being: Occupational health psychologists convene to share their research on work, stress, and health. *Monitor on Psychology* 39(5):26–29.
- Geurts, P., D. Ernst and L. Wehenkel. 2006. Extremely randomized trees. *Machine Learning* 63:3–42. <https://doi.org/10.1007/s10994-006-6226-1>.
- Kakuta, S., E. Ariyasu and T. Takeda. 2018. Shallow water bathymetry mapping using hyperspectral data. In *IGARSS 2018—2018 IEEE International Geoscience and Remote Sensing Symposium*, held in Valencia, Spain, 22–27 July 2018. <https://doi.org/10.1109/IGARSS.2018.8518386>.
- Lowe, D. G. 2004. Distinctive image features from scale-invariant keypoints. *International Journal of Computer Vision* 60:91–110. <https://doi.org/10.1023/B:VISI.0000029664.99615.94>.
- Lyzenga, D. R. 1981. Remote sensing of bottom reflectance and water attenuation parameters in shallow water using aircraft and LANDSAT data. *International Journal of Remote Sensing* 2(1):71–82. <https://doi.org/10.1080/01431168108948342>.
- Lyzenga, D. R. 1985. Shallow-water bathymetry using combined lidar and passive multispectral scanner data. *International Journal of Remote Sensing* 6(1):115–125. <https://doi.org/10.1080/01431168508948428>.
- Marcovecchio, J. and L. Ferrer. 2005. Distribution and geochemical partitioning of heavy metals in sediments of the Bahía Blanca estuary, Argentina. *Journal of Coastal Research* 21(4):826–834.
- Misra, A., Z. Vojinovic, B. Ramakrishnan, A. Luijendijk and R. Ranasinghe. 2018. Shallow water bathymetry mapping using Support Vector Machine (SVM) technique and multispectral imagery. *International Journal of Remote Sensing* 39(13):4431–4450. <https://doi.org/10.1080/01431161.2017.1421796>.
- Pan, Z., C. Glennie, J. C. Fernandez-Diaz and M. Starek. 2016. Comparison of bathymetry and seagrass mapping with hyperspectral imagery and airborne bathymetric lidar in a shallow estuarine environment. *International Journal of Remote Sensing* 37(3):516–536. <https://doi.org/10.1080/01431161.2015.1131869>.
- Papadopoulou, M., P. Lafazani, E. R. Mavridou, M. Tsakiri-Strati and G. Doxani. 2015. Creation of digital bathymetric maps using high resolution satellite imagery and multispectral bathymetric modeling for shallow waters. *Measuring and Mapping the Earth, Special issue for Professor Emeritus Christogeorgis Kaltsikis. School of Rural and Surveying Engineers, Aristotle University Thessalonica*. <https://doi.org/10.13140/RG.2.1.4012.6167>.
- Pedregosa, F., G. Varoquaux, A. Gramfort, V. Michel, B. Thirion, O. Grisel, M. Blondel, P. Prettenhofer, R. Weiss, V. Dubourg, J. Vanderplas, A. Passos, D. Cournapeau, M. Brucher, M. Perrot and É. Duchesnay. 2011. Scikit-learn: Machine learning in Python. *Journal of Machine Learning Research* 12:2825–2830.
- Piccolo, M. C., G.M.E. Perillo and W. D. Melo. 2008. The Bahía Blanca Estuary: An integrated overview of its geomorphology and dynamics. In *Perspectives on Integrated Coastal Zone Management in South America*, edited by J. Editor, 219–229. City, State: Publisher.
- Popovich, C. A. and J. E. Marcovecchio. 2008. Spatial and temporal variability of phytoplankton and environmental factors in a temperate estuary of South America (Atlantic coast, Argentina). *Continental Shelf Research* 28(2):236–244. <https://doi.org/10.1016/j.csr.2007.08.001>.
- Revollo, N. V., G. N. Revollo Sarmiento, M. A. Huamantincio Cisneros, C. A. Delrieux and M. C. Piccolo. 2019. Assessing the evolution in remotely sensed vegetation index using image processing techniques. *Anuário do Instituto de Geociências-UFRJ* 42(3):27–41.
- Rikola. 2015. Rikola Hyperspectral Imager—Quick start guide. Kaitoväylä, Finland: Rikola Ltd.
- Stumpf, R. P., K. Holderied and M. Sinclair. 2003. Determination of water depth with high-resolution satellite imagery over variable bottom types. *Limnology and Oceanography* 48(1, part 2):547–556.
- Su, H., H. Liu and W. D. Heyman. 2008. Automated derivation of bathymetric information from multi-spectral satellite imagery using a non-linear inversion model. *Marine Geodesy* 31(4):281–298. <https://doi.org/10.1080/01490410802466652>.
- Szeliski, R. 2011. *Computer Vision: Algorithms and Applications*. London: Springer.
- Wang, Y., X. Zhou, C. Li, Y. Chen and L. Yang. 2020. Bathymetry model based on spectral and spatial multifeatures of remote sensing image. *IEEE Geoscience and Remote Sensing Letters* 17(1):37–41.

SUSTAININGMEMBERS

ACI USA Inc.

Weston, Florida
<https://acicorporation.com/>
 Member Since: 2/2018

Aerial Services, Inc.

Cedar Falls, Iowa
www.AerialServicesInc.com
 Member Since: 5/2001

Ayres Associates

Madison, Wisconsin
www.AyresAssociates.com
 Member Since: 1/1953

Dewberry

Fairfax, Virginia
www.dewberry.com
 Member Since: 1/1985

Environmental Research Incorporated

Linden, Virginia
www.eri.us.com
 Member Since: 8/2008

Esri

Redlands, California
www.esri.com
 Member Since: 1/1987

GeoCue Group

Madison, Alabama
<http://www.geocue.com>
 Member Since: 10/2003

Geographic Imperatives LLC

Centennial, Colorado
<http://geographicimperativesllc.com>
 Member Since: 9/2021

GeoWing Mapping, Inc.

Richmond, California
www.geowingmapping.com
 Member Since: 12/2016

GPI Geospatial Inc.

formerly Aerial Cartographics of America, Inc. (ACA)
 Orlando, Florida
www.aca-net.com
 Member Since: 10/1994

Green Grid Inc.

San Ramon, California
www.greengridinc.com
 Member Since: 1/2020

Keystone Aerial Surveys, Inc.

Philadelphia, Pennsylvania
www.kasurveys.com
 Member Since: 1/1985

Kucera International

Willoughby, Ohio
www.kucerainternational.com
 Member Since: 1/1992

L3Harris Corporation

Broomfield, Colorado
www.harris.com
 Member Since: 6/2008

NV5 Geospatial

Sheboygan Falls, Wisconsin
www.quantumspatial.com
 Member Since: 1/1974

Pickett and Associates, Inc.

Bartow, Florida
www.pickettusa.com
 Member Since: 4/2007

Riegl USA, Inc.

Orlando, Florida
www.rieglusa.com
 Member Since: 11/2004

Robinson Aerial Surveys, Inc.(RAS)

Hackettstown, New Jersey
www.robinsonaerial.com
 Member Since: 1/1954

Sanborn Map Company

Colorado Springs, Colorado
www.sanborn.com
 Member Since: 10/1984

Scorpius Imagery Inc.

Newark, Delaware
aerial@scorpiusimagery.com
 Member Since: 6/2021

Surdex Corporation

Chesterfield, Missouri
www.surdex.com
 Member Since: 12/2011

Surveying And Mapping, LLC (SAM)

Austin, Texas
www.sam.biz
 Member Since: 12/2005

T3 Global Strategies, Inc.

Bridgeville, Pennsylvania
<https://t3gs.com/>
 Member Since: 6/2020

Towill, Inc.

San Francisco, California
www.towill.com
 Member Since: 1/1952

Woolpert LLP

Dayton, Ohio
www.woolpert.com
 Member Since: 1/1985

SUSTAININGMEMBERBENEFITS

Membership

- ✓ Provides a means for dissemination of new information
- ✓ Encourages an exchange of ideas and communication
- ✓ Offers prime exposure for companies

Benefits of an ASPRS Membership

- Complimentary and discounted Employee Membership*
- E-mail blast to full ASPRS membership*
- Professional Certification Application fee discount for any employee
- Member price for ASPRS publications
- Discount on group registration to ASPRS virtual conferences
- Sustaining Member company listing in ASPRS directory/website
- Hot link to company website from Sustaining Member company listing page on ASPRS website
- Press Release Priority Listing in PE&RS Industry News
- Priority publishing of Highlight Articles in PE&RS plus, 20% discount off cover fee
- Discount on PE&RS advertising
- Exhibit discounts at ASPRS sponsored conferences (exception ASPRS/ILMF)
- Free training webinar registrations per year*
- Discount on additional training webinar registrations for employees
- Discount for each new SMC member brought on board (Discount for first year only)

*quantity depends on membership level



WHITTLES PUBLISHING

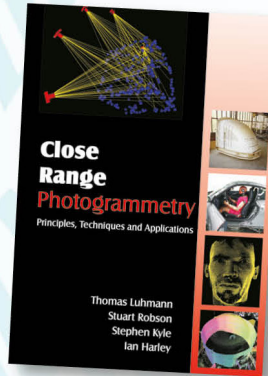
SIMPLY BRILLIANT BOOKS

ASPRS MEMBER EXCLUSIVE

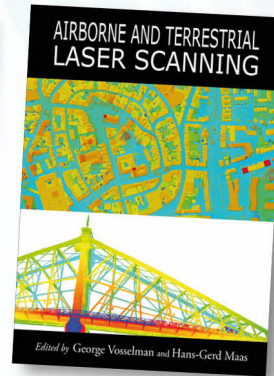
20% DISCOUNT

ON ALL WHITTLES PUBLISHING BOOKS USING CODE WPASPRS2

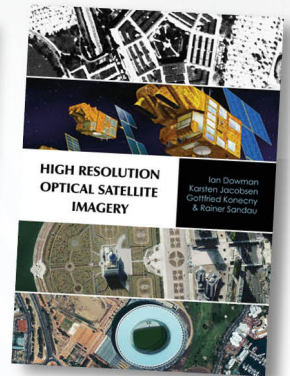
WHITTLES PUBLISHING'S STABLE OF CLASSIC GEOMATICS BOOKS INCLUDES THE THREE WINNERS OF THE PRESTIGIOUS KARL KRAUS MEDAL AWARDED BY ISPRS



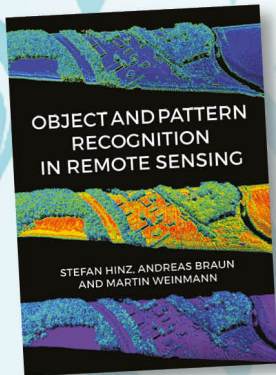
978-1870325-73-8 (Available as a CD)



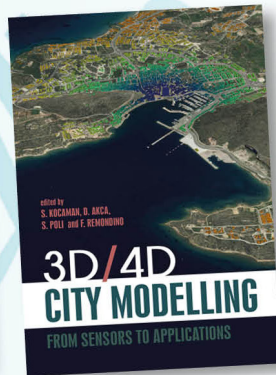
978-1904445-87-6



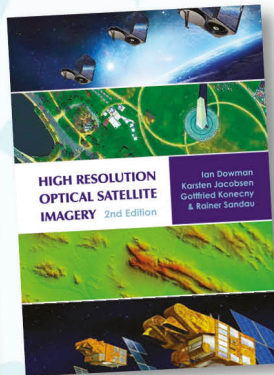
ISBN? Website only has 2nd edition



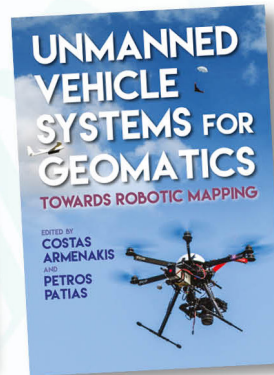
978-184995-128-9



978-184995-475-4



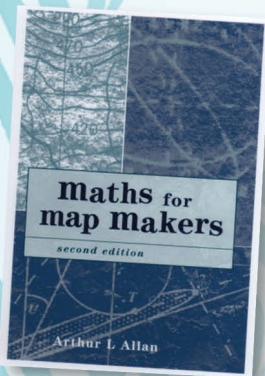
978-184995-390-0



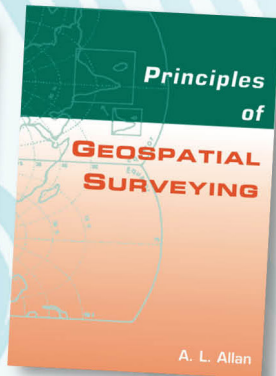
978-184995-127-2

OUR LIST CONTINUES TO EXPAND WITH THESE NEW TITLES

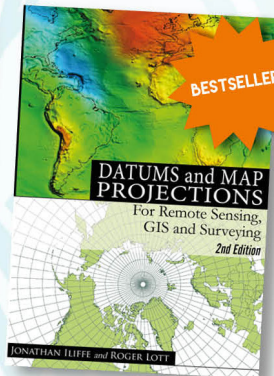
BROWSE OUR WEBSITE TO SEE OUR FULL RANGE OF ACCLAIMED GEOMATICS BOOKS



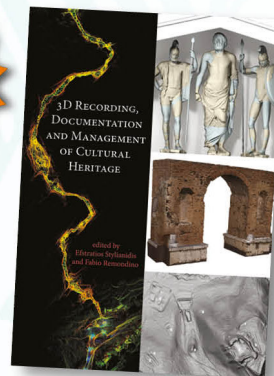
978-1870325-99-8



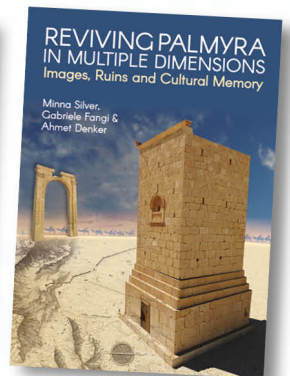
978-1904445-21-0



978-1904445-47-0



978-184995-168-5



978-184995-296-5

LEARN
DO
GIVE
BELONG

ASPRS Offers

- » Cutting-edge conference programs
- » Professional development workshops
- » Accredited professional certifications
- » Scholarships and awards
- » Career advancing mentoring programs
- » *PE&RS*, the scientific journal of ASPRS

asprs.org

ASPRS